

© Copyright by Eric Ashley Olson, 2003

NANOCALORIMETRY OF BISMUTH NANOPARTICLES

BY

ERIC ASHLEY OLSON

B.S., Rice University, 1995

DISSERTATION

Submitted in partial fulfillment of the requirements  
for the degree of Doctor of Philosophy in Materials Science and Engineering  
in the Graduate College of the  
University of Illinois at Urbana-Champaign, 2003

Urbana, Illinois

**CERTIFICATE OF COMMITTEE APPROVAL**

*University of Illinois at Urbana-Champaign  
Graduate College*

August 27, 2003

*We hereby recommend that the thesis by:*

**ERIC ASHLEY OLSON**

*Entitled:*

**NANOCALORIMETRY OF BISMUTH NANOPARTICLES**

*Be accepted in partial fulfillment of the requirements for the degree of:*

**Doctor of Philosophy**

*Signatures:*



*Director of Research*



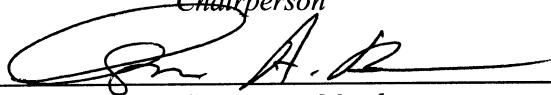
*Head of Department*

Committee on Final Examination\*



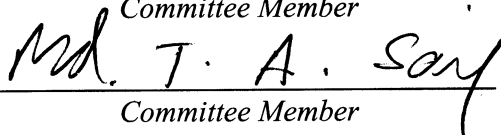
*Chairperson*

*Committee Member*

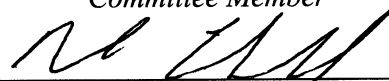


*Committee Member*

*Committee Member*



*Committee Member*



*Committee Member*

\* Required for doctoral degree but not for master's degree

## **Abstract**

The properties of nanosized bismuth particles are investigated using a nanocalorimetric technique. A brief description of the experimental method and data analysis procedures is reported. Bismuth nanoparticles are found to melt at a temperature below that of bulk material, but higher than expected using the standard model.

Also included is the results of a finite element analysis and simulated melting of bismuth films on various kinds of sensors. Temperature distributions are found to be nonuniform for calorimetric sensors with Al metallizations, but much more uniform for Pt metallized sensors. The consequences of this nonuniformity on caloric data are discussed.

## **Acknowledgments**

This work would not have been possible without the support of the rest of my research group: Les Allen, Mikhail Efremov, Alex Kwan, Francois Schiettekatte, Ming Zhang, and Zishu Zhang. Thanks to Ming, especially, for doing most of the TEM. Phil Infante at the Cornell Nanofabrication Facility was invaluable in the fabrication of the sensors.

This work was performed in part at the Cornell Nano-Scale Science & Technology Facility (a member of the National Nanofabrication Users Network) which is supported by the National Science Foundation under grant ECS-9731293, its users, Cornell University, and industrial affiliates.

SEM and TEM were carried out in the Center for Microanalysis of Materials at the University of Illinois, which is partially supported by the U.S. Department of Energy under grant DEFG02-91-ER45439. Optical microscopy was done in the author's laboratory.

This work was supported by National Science Foundation grants ECS-9807384, DMR-9803019, and DMR-0108694 as well as by American Chemical Society Petroleum Research Fund grant 37027-AC7.

## Table of Contents

List of Figures.....	viii
List of Symbols.....	xiii
Chapter 1: Introduction.....	1
1.1    References.....	3
1.2    Figures.....	5
Chapter 2: Previous Work.....	6
2.1    Bismuth.....	6
2.2    Melting Point Depression.....	7
2.3    Superheating and Surface Melting.....	8
2.4    Hamaker Constant.....	10
2.5    Other Size Anomalies.....	11
2.6    References.....	12
2.7    Figures and Tables.....	16
Chapter 3: The Nanocalorimetry Technique.....	21
3.1    MEMS Sensor.....	21
3.1.1    Sensor fabrication.....	22
3.2    Temperature Calibration.....	24
3.3    Experimental Setup.....	25
3.4    Calorimetric Pulsing.....	25
3.5    Data Analysis.....	26
3.6    LED Pulsing.....	28
3.7    Particle Counting.....	30

3.8	<i>Mapping</i> .....	31
3.9	<i>References</i> .....	32
3.10	<i>Figures</i> .....	33
Chapter 4: Bismuth.....		41
4.1	<i>Radius vs. Thickness</i> .....	41
4.2	<i>Heat Capacity and Heat of Fusion</i> .....	42
4.3	<i>Continuous Heat Capacity Measurement</i> .....	42
4.4	<i>Heat Capacity Dependence on Heating Rate</i> .....	43
4.4.1	<i>Finite element analysis</i> .....	44
4.4.2	<i>Very slow pulses</i> .....	46
4.4.3	<i>Experimental evidence of nonuniformity</i> .....	46
4.5	<i>Mapped Melting Temperatures</i> .....	47
4.6	<i>References</i> .....	48
4.7	<i>Figures and Tables</i> .....	49
Chapter 5: Discussion.....		64
5.1	<i>Sensor Uniformity</i> .....	64
5.2	<i>Temperature Calibration</i> .....	64
5.3	<i>Superheating and Kinetics</i> .....	66
5.4	<i>Conclusions</i> .....	68
5.5	<i>References</i> .....	68
5.6	<i>Figures</i> .....	70
Chapter 6: Future Work.....		71
6.1	<i>References</i> .....	73

Appendix A: Scanning Calorimeter for Nanoliter Scale Liquid Samples .....	74
Appendix B: Protein Research.....	87
Appendix C: FEA Programs .....	89
Vita.....	102



## List of Figures

Figure 1-1	Cross sectional view of a superconducting transition-edge microcalorimeter used to detect X-rays in X-ray microanalysis. An X-ray passes through the aperture and is absorbed by the 2 $\mu\text{m}$ Bi film, and detected by the Al-Ag superconductor. A 250 nm $\text{SiN}_x$ membrane is used for thermal isolation. The resolution of this device is 3–4 eV. Reprinted from [20].	5
Figure 2-1	(a) The rhombohedral lattice can be written in terms of a hexagonal lattice. (b) The similarity between a rhombohedral lattice and a cubic one. In a true cubic lattice, the angle $\alpha$ between the rhombic unit vectors is $60^\circ$ , but in Bi, the body diagonal is slightly stretched, and $\alpha = 57^\circ$ . Reprinted from [30].	16
Figure 2-2	Pressure-temperature phase diagram for bulk Bi, showing several high pressure solid phases. Reprinted from [31].	17
Figure 2-3	Construction commonly used in the calculation of the Hamaker constant. Part (a) shows two solid surfaces separated by vacuum at some distance $d$ . In this case, the force between the bodies will always be attractive. Part (b) shows a large solid surface separated from its own vapor by a liquid layer. The force between the vapor and the solid will be dependent on the properties of the liquid, relative to the vapor and solid. Usually, the force will be repulsive. For some materials (e.g. Bi and Ge), the force will be attractive, and the liquid layer will thin, or even vanish.	18
Figure 2-4	Crystal structure of Bi. (a) The standard rhombohedral unit cell of Bi, with two atoms per cell. [32] This is very similar, but slightly distorted from, a cube. (b) Some researchers have suggested that small Bi particles have a cubic structure. [29] If the Bi rhombohedron is distorted such that the angle between the rhombohedral axes is $60^\circ$ , the unit cell can also be described as a cube, where the rhombohedron's corners are at the centers of the cube faces. Only the atoms inside the rhombohedral unit cell are shown here.	19
Figure 3-1	Schematic of the MEMS sensor, not to scale. (a) A top view showing the location of the $\text{SiN}_x$ , the membrane, and the metallization. (b) The metallization showing the electrical connections. (c) A cross section, showing the location of the membrane and metal heater.	33

Figure 3-2	Sensor fabrication process. (a) The process starts with a silicon wafer with $\text{SiN}_x$ deposited on both sides. (b) Photoresist (PR) is spun on both sides, then one side is patterned and reactive-ion etched. (c) The PR is stripped off and the Si is etched using an 80 °C KOH solution. (d) Another PR layer is spun on, patterned, and developed so that a liftoff profile is created. (e) Metal is deposited uniformly on the wafer. (f) The PR and excess metal is removed in an acetone bath.....	34
Figure 3-3	Electrical schematic of a differential nanocalorimetric experiment. Shown are: supply voltages $V_{SUP}$ , adjustable resistances $R_{EXT}$ , ammeters $A$ , voltages across each calorimetric sensor $V$ , currents $I$ , and the differential voltage $\Delta V$ . The small section of each sensor that is heated, but not included in the voltage measurement is represented here as $R_H$ . The $R$ and $S$ subscripts denote the reference and sample branches of the circuit, respectively. ....	35
Figure 3-4	Typical experimental data for a 10 nm Bi film on a sensor with an Al metallization. (a) $I_S$ and $I_R$ . (b) $V_S$ and $V_R$ . (c) $R_S$ and $R_R$ . (d) $T_S$ and $T_R$ . (e) $\Delta V$ and $d(\Delta V)/dt$ . (f) The final heat capacity curve. The heating rate in this case was $\sim 40$ kK/s.....	36
Figure 3-5	Results of calorimetric scan synchronized with an LED pulse. (a) The experimental setup. A 50 nm Bi film was deposited onto the calorimeter, and a blue LED used to flash onto the sensor area 1 ms into the 7 ms calorimetric scan. (b) The LED pulse is visible in the $d(\Delta V)/dt$ data. (c) The effect of the LED pulse on the calorimetric scan itself. Since the LED supplies energy, it has an effect similar to an exothermic reaction, and $C_p$ curve decreases. (d) The amount of heat under the LED pulse trough in (c) scales linearly with the length of the pulse. ....	37
Figure 3-6	Particle counting. Shown are TEM micrographs, thresholded images, and calculated particle size histograms for 0.4 nm, 2 nm, and 5 nm Bi films. In the histogram, the number density of particles $h(r)$ has been multiplied by the volume of each bin, $4/3\pi r^3$ . The histogram has also been divided by the bin size so that the integrated area represents the average film thickness.....	38
Figure 3-7	Mapping of calorimetry data to particle size for a 2 nm Bi deposition. (a) The results of a calorimetric scan. (b) The particle size histogram. Here, the particle number density $h(r)$ has been multiplied by the volume of a particle in each bin. (c) The integrated calorimetric data. (d) The integrated particle size data. (e) The resulting mapped relationship between melting temperature and particle radius. Blue and red lines in (c) and (d) show how one temperature is connected to a particular particle size, and correspond to blue and red dots in (e).....	39

Figure 3-8	Mapping procedure as applied to indium experiments. (a) The results from a series of films ranging from 0.2 to 10 nm. (b) Averaged $T_m(r)$ data, along with expected values using various melting models. The data fits the HMM (HGM in the figure) well. Reprinted from [5].	40
Figure 4-1	TEM micrographs for Bi and In films, 5 and 10 nm thick, heated (hot) and unheated (cold). Note how the hot films are similar at 5 nm, but the Bi particles in the 10 nm thickness are much larger than those in the corresponding In micrograph.	49
Figure 4-2	Mean particle radius vs. average film thickness. Note how the 10 nm Bi trends toward high values. Data for Sn films above 5 nm were not available.	50
Figure 4-3	Dual deposition showing bimodal particle size distribution. A 10 nm Bi deposition was done to form large particles, then an addition 0.8 nm deposited to form small ones. (a) A portion of a TEM micrograph showing a few very large particles combined with many smaller ones. (b) The particle size histogram of the entire micrograph from (a). The small particles from the 0.8 nm deposition can be seen in the 0-10 nm region of the histogram, and the large particles above 10 nm. Note the difference in scale before and after the y-axis break. (c) Heat capacity data from the 10 nm and the 10+0.8 nm films. The smaller particles have a lower $T_m$ , which can be seen in the small melting peak $\sim 225$ °C.	51
Figure 4-4	Heat capacity curves for two Bi films, 1.0 and 0.4 nm thick. The (peak) melting temperature for the 0.4 nm curve is $\sim 25$ °C lower than that of the 1.0 nm film. This is due to the smaller average radius of particles. Similarly, the integrated area under the peak is smaller, because there is less material to melt, and, accordingly, less heat is required to melt it. The heating rates for these films was $\sim 40$ kK/s.	52
Figure 4-5	Heat capacity and heat of fusion for a series of twenty-three Bi films. (a) Heat capacity at 50 °C as a function of nominal film thickness measured by the quartz crystal thickness monitor. The dashed line represents the bulk heat capacity $\overline{c_p}(T)$ . (b) Latent heat of fusion as a function of nominal film thickness. (c) Heat of fusion as a function of sample mass, where mass has been calculated from the measured heat capacity. In (b) and (c), the dashed line represents the bulk heat of fusion.	53
Figure 4-6	Continuous heat capacity measurement. Here, the continuous deposition of Bi onto a sensor is measured in real-time at 1 calorimetric scan/s. The total deposition onto the quartz crystal monitor used to monitor film thickness was 2 nm, but the $C_p$ and $H_m$ values from the calorimetric curve both suggest there was only $\sim 0.1$ nm deposited onto the sensor.	54

Figure 4-7	Melting of a 10 nm Bi film at six different heating rates, using sensors with Al metallizations. Only the region of the caloric curve near the melting temperature is shown. $T_m^{bulk}$ is shown by the dashed line. ....	55
Figure 4-8	Melting of a 10 nm Bi film at six different heating rates, using sensors with Pt metallizations. Only the region of the caloric curve near the melting temperature is shown. $T_m^{bulk}$ is shown by the dashed line. The decrease in the peak temperature suggests that the particles measured here are slightly smaller than those measured in Fig. 1-5. ....	56
Figure 4-9	FEA simulated heat capacity of a uniform 5 nm Bi film on an Al sensor measured at six different heating rates. $T_m^{bulk}$ is shown by the dashed line. There is ~25 K difference between the curves at 140 kK/s and 7.2 kK/s. Also, the slower curves are broader and have a smaller integrated area. ....	57
Figure 4-10	FEA simulated heat capacity of a uniform 5 nm Bi film on a Pt sensor measured at six different heating rates. The axis limits for this figure are the same as in Fig. 1-7. The difference in the location of the peaks between the fastest and slowest pulses is ~9 K.....	58
Figure 4-11	FEA simulations of a 5 nm Bi film on (a) Pt and (b) Al sensors at ~40 kK/s. Both columns show the temperature distributions at the end of the scan; the right-hand column is an overhead view. Black lines in the right-hand column figures show the outline of the heater and voltage senses. The location of $T_m^{bulk}$ is shown by a dark contour line. All Bi inside this line is melted; everything outside it is solid. The slight distortion at ~1000 $\mu\text{m}$ and ~6500 $\mu\text{m}$ is due to heat being drawn away by the triangular voltage contacts.....	59
Figure 4-12	FEA simulation of a 5 nm Bi film on an Al sensor at ~7 kK/s. Black lines show the outline of the heater and voltage senses. The location of $T_m^{bulk}$ is shown by a dark contour line. Note the high temperature at the very center of the heater, but the melted zone does not reach out even to the voltage contacts. ....	60
Figure 4-13	Optical micrographs of a 10 nm Bi film on (a) an Al sensor and (b) a Pt sensor. These sensors had each been heated to 310 °C at ~7 kK/s. The Bi is limited to a 400 $\mu\text{m}$ wide stripe down the center of the heater. There is a contrast difference between melted and unmelted Bi. For the Pt sensor in (b), the melted zone extends to the edge of the voltage senses. For the Al sensor in (a), not all the material had melted, even though the measured average temperature was 40 K above $T_m^{bulk}$ .....	61

Figure 4-14	Mapped data for this work. Shown are melting temperatures as functions of particle sizes, using films 0.3 nm to 10 nm thick. The dotted line is $T_m^{bulk}$ for Bi, 271 °C.....	62
Figure 4-15	Mapped data for this work, as well as results from two other researchers. The dotted line is $T_m^{bulk}$ for Bi, 271 °C. The dashed line represents the expected values using the HMM model and surface energies according to G. Allen. [2].....	63
Figure 5-1	Amounts of observed Bi superheating compared with the experimental heating rates used to observe them. It should be noted that G. Allen's, Peppiatt's and Murphy's work refers to superheating above $T_m^{bulk}$ , while this work refers to superheating above the expected, size-depressed melting temperature $T_m^{HMM}(r)$ . Murphy's work was on a single crystal of Bi, not small particles. ....	70

## List of Symbols

d	thickness of liquid layer on a particle
h	particle size distribution
k	thermal conductivity
r	radius
t	time
v	heating rate; $dT/dt$
$C_P^0$	heat capacity baseline
$C_P^{cell}$	heat capacity of the calorimetric cell (sensor)
$C_P^X$	heat capacity of the sample
D	thermal diffusivity ( $D \equiv kC_P^{-1}\rho^{-1}$ )
H	Hamaker constant
$H_m^{bulk}$	bulk heat of fusion
$H_m^{TEM}$	average heat of fusion for one calorimetric experiment
$I_S$	current through the sample branch of the circuit
$I_R$	current through the reference branch of the circuit
P	electric power
S	surface area of the heater
T(R)	temperature as a function of resistance; usually a fourth-order polynomial fitted to experimental data
$T_m$	melting temperature
$T_m(r)$	size dependent melting temperature
$T_m^{bulk}$	melting temperature of bulk material
$V_S$	voltage drop across the sample sensor
$V_R$	voltage drop across the reference sensor
$\alpha$	melting-model-dependent parameter, also angle between crystallographic directions
$\rho_L$	liquid phase density
$\rho_S$	solid phase density
$\sigma_{LV}$	liquid-vapor interface energy
$\sigma_{SL}$	solid-liquid interface energy
$\sigma_{SV}$	solid-vapor interface energy
$\Delta T$	melting point depression
$\Delta V$	differential voltage

## Chapter 1: Introduction

Heat energy is a fundamental characteristic of every phase transformation and chemical reaction. Temperature, and therefore any resulting flow of heat, is one of the easiest controlled external thermodynamic variables. Calorimetry is the preferred technique for investigations of the energetics of material transformations, and has been used as such for over a hundred years. The growing interest in investigating material at nanometer-sized scales, however, requires refinements to the technique and the development of new devices that are not currently commercially available.

The physical size of material can have a tremendous effect on its thermodynamic properties. Heat capacity measurements are useful in quantifying these changes in materials characteristics. Many properties of a thin film or a small particle can be considerably different than that of the same material in bulk form: electrical resistance increases [1]; indirect bandgap semiconductors emit visible light [2]; crystal structures even change [3, 4]. This is because surface and interfacial effects, negligible in bulk material, become dominant at small scales where the total fraction of atoms at the surface is significant.

Investigating the properties of these small-scale materials, however, becomes problematic. Because any nanoscale material sample is small, any thermal signal from it is also small, and therefore difficult to measure. Also, since it is the size of the material that induces the unusual properties, the material sample can not simply be increased in size. The signal of interest can be increased by creating multilayered structures [5] or using substrates with extremely high surface areas [6, 7]. These methods, however, can introduce other effects which have little to do with the phenomenon of interest, and are not necessarily applicable to all materials systems.

Measuring small samples becomes problematic when the sample size become much smaller than the size of the calorimeter itself. At some point, it becomes necessary to shrink the calorimetric cell to measure small samples and still maintain an acceptable signal-to-noise ratio. Any number of different designs of calorimeters have been made with this in mind [8-10].

With the advent of microelectromechanical systems (MEMS), it became possible to build thermal sensors much smaller than ever before. The designs of most of these sensors build the active part of the sensor on a thin membrane, which considerably reduces the mass of the sensor itself, allowing for a much higher sensitivity. Also, the membrane materials are usually of low thermal conductivity, which thermally isolates the sensor from its surroundings.

The earliest of these MEMS thermal devices, built in the mid-1980's, was actually an X-ray detector in which an absorbed X-ray photon generated a heat pulse, which was measured by the calorimeter as a change in temperature [11]. Descendants of this design are used for astronomical observations [12] and next-generation X-ray spectroscopy systems for electron microscopy [13]. See Fig. 1-1 for an example of this type of sensor. A few years later, and apparently independently, another researcher designed a thin-film calorimeter to measure catalyzed gas-phase reactions [14, 15].

These sensors, however, all detect changes in temperature from some outside source, whether it is the absorption of an X-ray photon or a gas-phase reaction occurring that the sensor surface [16]. It is also possible to actively heat the sensor and measure its response with respect to temperature. If heated and cooled in a periodic manner (AC calorimetry) very accurate values of the heat capacity of a sample can be measured [17, 18]. It is also possible to increase the temperature at a constant rate and measure this effect [19]. This scanning calorimetric method has the advantage of being better suited to the measurement of latent heats of fusion.



## 1.1 References

- [1] D. Golmayo and J. L. Sacedon. "Measurements and interpretation of the electrical resistivity and Hall coefficient in polycrystalline gold films. I." *Thin Solid Films* **35**. 137 (1976).
- [2] O. Akcikir, J. Therrien, G. Belomoin, N. Barry, J. D. Muller, E. Gratton, and M. Nayfeh. "Detection of luminescent single ultrasmall silicon nanoparticles using fluctuation correlation spectroscopy." *Appl. Phys. Lett.* **76**. 1857 (2000).
- [3] M. G. Mitch, S. J. Chase, J. Fortner, R. Q. Yu, and J. S. Lannin. "Phase transition in ultrathin Bi films." *Phys. Rev. Lett.* **67**. 875 (1991).
- [4] J. P. K. Doye and F. Calvo. "Entropic effects on the size dependence of cluster structure." *Phys. Rev. Lett.* **86**. 3570 (2001).
- [5] E. J. Cotts. "Differential scanning calorimetry studies of thin films and multilayered composites." in *Thermal Analysis in Metallurgy*. R. D. Shull and A. Joshi. Eds. Warrendale, PA: TMS. 1992. pp. 299.
- [6] A. Bogdan, M. Kulmala, and N. Avramenko. "Reduction of enthalpy of fusion and anomalies during phase transitions in finely divided water." *Phys. Rev. Lett.* **81**. 1042 (1998).
- [7] G. K. Rennie and J. Clifford. "Melting of ice in porous solids." *J. Chem. Soc., Faraday Trans.* **73**. 680 (1977).
- [8] S. Randzio and W. Zielenkiewicz. "Microcalorimeter for heat of chemisorption measurements at higher temperatures on evaporated metallic films." *Bull. Acad. Pol. Sci. Ser. Sci. Chim.* **XXIV**. 323 (1976).
- [9] H. Yao and I. Hatta. "An AC microcalorimetric method for precise heat capacity measurement in a small amount of liquid." *Jpn. J. Appl. Phys., Part 2* **27**. L121 (1988).
- [10] C. E. Borroni-Bird and D. A. King. "An ultrahigh vacuum single crystal adsorption microcalorimeter." *Rev. Sci. Instrum.* **62**. 2177 (1991).
- [11] D. McCammon, S. H. Moseley, J. C. Mather, and R. F. Mushotzky. "Experimental tests of a single-photon calorimeter for X-ray spectroscopy." *J. Appl. Phys.* **56**. 1263 (1984).
- [12] C. K. Stahle, J. Wouters, R. L. Kelley, S. H. Moseley, and A. E. Szymkowiak. "Charge collection and thermalization in a composite calorimetric and ionization X-ray detector." *J. Appl. Phys.* **75**. 3723 (1994).
- [13] D. A. Wollman, K. D. Irwin, G. C. Hilton, L. L. Dulcie, D. E. Newbury, and J. M. Martinis. "High-resolution, energy-dispersive microcalorimeter spectrometer for X-ray microanalysis." *J. Microsc.* **188**. 196 (1997).

- [14] F. Nuscheler. "The microcalorimeter, a silicon gas sensor." *Arch. Elektronik Übertragungstechnik* **42**. 80 (1988).
- [15] F. Nuscheler. "An investigation of the dynamic behaviour of a silicon microcalorimeter." *Sensors & Actuators* **17**. 593 (1989).
- [16] J. S. Suehle, R. E. Cavicchi, M. Gaitan, and S. Semancik. "Tin oxide gas sensor fabricated using CMOS micro-hotplates and in-situ processing." *IEEE Electron Device Lett.* **14**. 118 (1993).
- [17] D. W. Denlinger, E. N. Abarra, K. Allen, P. W. Rooney, M. T. Messer, S. K. Watson, and F. Hellman. "Thin film microcalorimeter for heat capacity measurements from 1.5 to 800 K." *Rev. Sci. Instrum.* **65**. 946 (1994).
- [18] F. Fominaya, T. Fournier, P. Gandit, and J. Chaussy. "Nanocalorimeter for high resolution measurements of low temperature heat capacities of thin films and single crystals." *Rev. Sci. Instrum.* **68**. 4191 (1997).
- [19] S. L. Lai, G. Ramanath, L. H. Allen, P. Infante, and Z. Ma. "High-speed ( $10^4$  degrees C/s) scanning microcalorimetry with monolayer sensitivity ( $J/m^2$ )." *Appl. Phys. Lett.* **67**. 1229 (1995).
- [20] G. C. Hilton, D. A. Wollman, K. D. Irwin, L. L. Dulcie, N. F. Bergren, and J. M. Martinis. "Superconducting transition-edge microcalorimeters for X-ray microanalysis." *IEEE Trans. Appl. Supercond.* **9**. 3177 (1999).

## 1.2 Figures

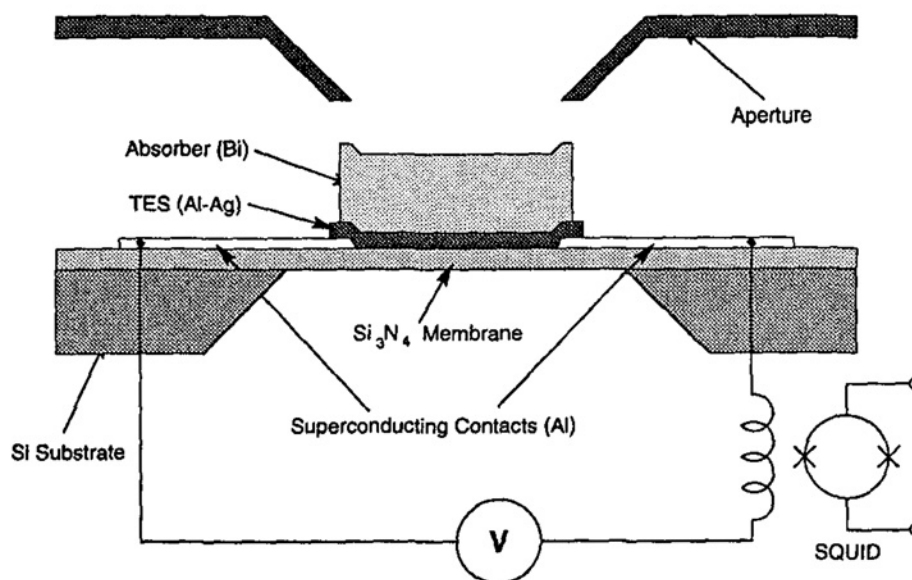


Figure 1-1: Cross sectional view of a superconducting transition-edge microcalorimeter used to detect X-rays in X-ray microanalysis. An X-ray passes through the aperture and is absorbed by the 2  $\mu\text{m}$  Bi film, and detected by the Al-Ag superconductor. A 250 nm  $\text{SiN}_x$  membrane is used for thermal isolation. The resolution of this device is 3–4 eV. Reprinted from [20].

## Chapter 2: Previous Work

### 2.1 Bismuth

Bismuth has a rhombohedral crystal structure, with a lattice parameter  $a_0 = 4.746 \text{ \AA}$  and  $\alpha = 57^\circ$ . The rhombohedral lattice can also be written in terms of a hexagonal one, as can be seen in Fig. 2-1(a). In this nomenclature,  $a'_0 = 4.546 \text{ \AA}$  and  $c'_0 = 11.86 \text{ \AA}$ . There are two bismuth atoms per lattice point. It is also interesting to note that the Bi rhombohedral lattice closely resembles a cubic one, as can be seen in Fig. 2-1(b). If the angle  $\alpha$  were  $60^\circ$ , it would be cubic. It is this slight distortion from the cubic structure that is responsible for the slight overlap in conduction and valence bands that makes Bi a semimetal. Bi is also highly anisotropic, with electron effective masses varying as much as  $200\times$ , depending on direction. [1]

Fig. 2-2 shows the phase diagram for bulk Bi. There are a number of phases available to Bi at high pressures. The surface tension of a liquid drop exerts a pressure when the drop is small. For a radius liquid drop 1 nm in radius with bulk surface tension, this pressure is expected to be  $\sim 0.8 \text{ GPa}$  (8 kbar), well within the Phase I/liquid regime. This approach assumes that the small particle behaves as a continuum and that there is no size dependency to the liquid surface tension. Some researchers have also suggested that there are even multiple *liquid* phases at high temperature and pressure [2]. Strange as this may sound, it has also been found in Te [3].

Although they will not be investigated here, bismuth has some unusual electrical properties that make it of interest. It has a large mean free path of 250 nm at 300 K [4], meaning that quantum confinement effects may be observed in relatively large samples. Nanowires, for example, undergo a semimetal-to-semiconductor transition as the wire diameter drops below  $\sim 65 \text{ nm}$  [5].

## 2.2 Melting Point Depression

The phenomenon of melting point depression in small bismuth particles was observed some time ago [6, 7]. Melting point depression, first theorized by Pawlow [8] in 1909, is due to the large influence surfaces have on small particles. When a particle is small, it has a small radius of curvature. The surface tension of the particle and small curvature have the effect of a large pressure on the particle, which reduces its melting temperature.

There are a number of different theories of how small particles melt, which may rely on factors such as a liquid layer covering the surface of the particle, or a liquid nucleus which grows as the particle melts. There is little evidence for such a liquid layer on small Bi particles, as opposed to other materials, so a homogenous melting model (HMM) can be applied. The HMM assumes that a particle melts completely when it reaches its melting temperature and there is no pre-melting. These models generally predict a melting temperature that will follow:

$$\Delta T = T_m^{bulk} - T_m(r) = \frac{2T_m^{bulk}}{H_m^{bulk} \rho_S} \frac{\alpha}{r} \quad (2-1)$$

where  $T_m^{bulk}$  is the bulk melting temperature,  $T_m(r)$  is the size dependent melting temperature,  $H_m^{bulk}$  is the bulk heat of fusion,  $\rho_S$  is the solid phase density, and  $r$  is the radius [9].  $\alpha$  is a parameter that depends on the melting model, and:

$$\alpha_{HMM} = \sigma_{SV} - \sigma_{LV} \left( \frac{\rho_S}{\rho_L} \right)^{2/3} \quad (2-2)$$

where  $\sigma_{SV}$  is the interface energy of the solid-liquid interface,  $\sigma_{LV}$  is the interface energy of the liquid-vapor interface, and  $\rho_L$  is the liquid phase density.

### 2.3 Superheating and Surface Melting

Supercooling is a fairly common effect. It is easily observed in metals, polymers, and other material systems. Superheating, however, is not generally observed in metallic systems. Crystallization requires the coordinated behavior of atoms; enough atoms must come together to form a nucleus of critical size before long-range crystallization can occur. For metals, roughly speaking [10]:

$$\sigma_{SV} > \sigma_{LV} + \sigma_{SL} . \quad (2-1)$$

Since the solid-vapor interface is of higher energy than the sum of the liquid-vapor and solid-liquid interfaces, it would be preferable for a liquid layer to exist between a solid and its vapor. In other words, the melt of a metal should entirely wet the solid, and superheating should not be possible. This approach neglects crystal anisotropy and any potential size effects.

Under some conditions, however, it is possible to heat a metal above  $T_m^{bulk}$ . Table 2-I shows a listing of a few such materials where superheating has been detected. Generally speaking, superheating is possible if and when the formation of a liquid layer at the surface can be prevented.

This superheating phenomenon has previously been observed in Bi [6, 11]. Here, Bi particles were heated to 7 K above  $T_m^{bulk}$  before they melted. A time delay in melting was also observed; particles of a given size did not melt instantaneously at a particular temperature, but after a certain period of time they would melt. The time delay was a characteristic of the melting temperature (and therefore, presumably, particle size). Lower temperatures (smaller particles) had a larger characteristic time delay than higher temperatures (larger particles). The particles in this study ranged from 8 nm to 15 nm in radius.

G. Allen also noticed this phenomenon in 1986 [7], with a superheating of 8 K for large particles ( $r > 50$  nm). This study included four materials, Bi, In, Pb, and Sn, but the superheating effect was only observed for Bi. G. Allen attributed this to an unknown surface effect which inhibited the formation of a liquid layer at the surface of a particle.

The heating rates used by these two investigators were low, 1-3 K/min, and on the order of those used in traditional differential scanning calorimetry (DSC). More recently, superheating of even bulk Bi single crystals has been observed using ultrafast heating [12]. Here, a pulsed laser was used to heat the surface of a crystal at rates  $\sim 10^{11}$  K/s and the loss of crystalline order measured using time-resolved reflection high-energy electron diffraction. This method was used to superheat a Bi (0001) crystal by 90 K. A Pb (111) surface was also superheated by 120 K [13], but a Pb (110) surface could not be superheated [14].

Based on only the results discussed above, it is clear that it is possible to heat some metals above their bulk melting temperatures, at least briefly. The question remains whether this superheated state is thermodynamically stable, or somehow kinetically trapped in the solid state.

How does a particle melt? In the homogeneous melting model, at some particular temperature  $T_m$ , crystalline order breaks down and the entire particle melts at once. The liquid shell model (LSM) assumes that there is a thin quasi-liquid [15] at the surface of a particle even below  $T_m$ . During the melting process, that liquid shell grows at the expense of the solid core. The liquid nucleation and growth (LNG) theory [16] suggests that for a particle to melt, a liquid nucleus must form, usually at the particle surface, and that nucleus grows during melting.

Small Pb platelets with only (111) faces can also be superheated to several degrees above  $T_m^{bulk}$ , and are stable for hours [17]. Similar particles with a mixture of (111) and other facets

melt normally. This, combined with the laser superheating experiments described above, suggests that superheating is a surface-dependent phenomenon.

Quasi-liquid layers have been observed on micron-sized Sn and In particles below  $T_m^{bulk}$  [18]. Melting for these particles is a smooth transition; the surface of a faceted particle roughens, and the liquid layer grows. On Bi particles, however, the facets remain until the entire particle melts all at once, suggesting that there is either no liquid layer, or a thin layer is present but can not grow below  $T_m$  [19]. Why, then, is the surface melting of Bi not present, while it is present in other material systems?

#### **2.4 Hamaker Constant**

Deviations of the ideal gas law by real materials drove van der Waals to introduce his now-famous corrections [20]. These described attractive forces between molecules, even when no permanent dipole was present. In 1937, Hamaker extended this theory to consider that the same sort of forces must exist between condensed phases of material rather than just between individual atoms and molecules [21].

It is now generally understood that these forces determine the interactions between colloidal particles in solution [22]. These forces can be described as having a geometric and material component. The geometric component will depend on the form the condensed phases take (e.g. spheres, flat planes). The material component is generally referred to as the Hamaker constant  $H$ . Fig. 2-3 shows the most commonly used geometric construction for calculations of these interactions.

Fortunately,  $H$  can be calculated from the frequency-dependent dielectric constant of the materials involved. In most cases,  $H$  is positive, meaning that there is a repulsive interaction between the solid-liquid interface and the liquid-vapor interface. If the liquid is more conducting



than the solid, however,  $H$  will be negative and the interaction between the two interfaces will be attractive [23]. Calculated Hamaker constants for some solid-liquid-vapor material systems can be seen in Table 2-II.

Bi and Ge are unusual in that they have a negative  $H$ . This is because solid Bi is a semi-metal, while liquid Bi is metallic and because solid Ge is a semiconductor, while liquid Ge is metallic. The effect of this negative  $H$  is that there is an attractive force between the liquid-solid and liquid-vapor interfaces on a surface-melted particle. This creates an energetic barrier to the formation of a liquid layer, and prevents its formation and/or growth.

### ***2.5 Other Size Anomalies***

In addition to melting temperature, other material parameters can exhibit size dependent properties. Indium, for example, undergoes a reduction in heat of fusion with size, as well as melting temperature [24].

One important question is whether solid Bi will undergo a structure change as its size increases. It is almost certain that it will do so; a cluster of just a few atoms is unlikely to form in the rhombohedral structure. Structure changes with size are not unknown. Indium, for example, is face-centered tetragonal in the bulk, but face-centered cubic below  $\sim 5$  nm in diameter [25]. The same study found no conclusive change in the structure or lattice parameter in Bi. Another study found a  $-0.1\%$  ( $\Delta a/a$ ) to  $-0.4\%$  ( $\Delta c/c$ ) lattice distortion, but suggested this could be due to excess vacancies in the solidified particles due to the electrohydrodynamic technique used to form the particles [26].

Another research group used Raman spectroscopy to probe the structural behavior of Bi solid and liquid particles [27, 28]. Their findings suggest an order-disorder transition with decreasing film thickness when measured at 110 K, with the transition occurring at an equivalent

film thickness of 0.8 nm. They reported only the film thickness, not particle sizes or distributions.

The same group later reported a similar transition in the liquid structure of Bi, namely a decrease in coordination number with decreasing film thickness [28]. They also suggest that the particles do not undergo densification upon melting. (Liquid bismuth is denser than its solid.) This transition appears to occur between 4.5 nm and 7.5 nm in diameter.

One group used gas-phase electron diffraction to study the lattice parameters and the ratio of the lattice parameters (using hexagonal structure notation) as a function of crystal size. [25] They found the lattice parameters were nearly constant for particles 6 nm in diameter and larger. There was the suggestion of a reduction in lattice parameter ratio, but the data were inconclusive.

More recently, one group used high-resolution TEM and reported that Bi crystals above 8 nm in size may have an outer surface with a rhombohedral crystal structure, but a cubic core. [29] They note that the Bi rhombohedral structure is actually very similar to a cubic structure. A distortion of less than three degrees is needed to make the Bi structure cubic. This suggests that there may be a size-dependent structure transition in Bi. The difference between the rhombohedral structure of Bi and the cubic structure suggested by these researchers can be seen in Fig. 2-4.

Nevertheless, the details of any phase transformation in Bi with decreasing size remain elusive. It is not clear whether there is a structural change or even a significant change in the lattice parameter for small particles.

## **2.6 References**

- [1] J. P. Issi. "Low temperature transport properties of the group V semimetals." *Aust. J. Phys.* **32**. 585 (1979).

- [2] A. G. Umnov, V. V. Brazhkin, S. V. Popova, and R. N. Voloshin. "Pressure-temperature diagram of liquid bismuth." *J. Phys. Condens. Matter* **4**. 1427 (1992).
- [3] K. Yaoita, K. Tsuji, Y. Katayama, N. Koyama, T. Kikegawa, and O. Shimomura. "Structural study on proposed phase-transition of liquid tellurium under high-pressure." *J. Non-Cryst. Solids* **156-158**. 157 (1993).
- [4] V. Damodara Das and N. Soundarajan. "Size and temperature effects on the Seebeck coefficient of thin bismuth films." *Phys. Rev. B* **35**. 5990 (1987).
- [5] J. Heremans, C. M. Thrush, L. Yu-Ming, S. Cronin, Z. Zhang, M. S. Dresselhaus, and J. F. Mansfield. "Bismuth nanowire arrays: Synthesis and galvanomagnetic properties." *Phys. Rev. B* **61**. 2921 (2000).
- [6] S. J. Peppiatt. "The melting of small particles. II. Bismuth." *Proc. R. Soc. London, Ser. A* **345**. 401 (1975).
- [7] G. L. Allen, R. A. Bayles, W. W. Gile, and W. A. Jesser. "Small particle melting of pure metals." *Thin Solid Films* **144**. 297 (1986).
- [8] P. Pawlow. *Z. Phys. Chem.* **65**. 545 (1909).
- [9] M. Zhang, M. Y. Efremov, F. Schiettekatte, E. A. Olson, A. T. Kwan, S. L. Lai, T. Wisleder, J. E. Greene, and L. H. Allen. "Size-dependent melting point depression of nanostructures: Nanocalorimetric measurements." *Phys. Rev. B* **62**. 10548 (2000).
- [10] J. H. Holloman and D. Turnbull. "Nucleation." *Prog. Met. Phys.* **4**. 333 (1953).
- [11] M. Blackman, S. J. Peppiatt, and J. R. Sambles. "Superheating of bismuth." *Nature (Physical Science)* **239**. 61 (1972).
- [12] E. A. Murphy, H. E. Elsayed-Ali, and J. W. Herman. "Superheating of Bi(0001)." *Phys. Rev. B* **48**. 4921 (1993).
- [13] J. W. Herman and H. E. Elsayed-Ali. "Superheating of Pb(111)." *Phys. Rev. Lett.* **69**. 1228 (1992).
- [14] J. S. Herman and H. E. Elsayed-Ali. "Time-resolved study of surface disordering of Pb(110)." *Phys. Rev. Lett.* **68**. 2952 (1992).
- [15] Atoms in a liquid layer on a particle are free to move in directions parallel to the particle surface, but are more constrained in the direction perpendicular to it. Because of this, the liquid layer is not a "liquid" in the same sense of a bulk liquid, hence the term "quasi-liquid."
- [16] P. R. Couchman and W. A. Jesser. "Thermodynamic theory of size dependence of melting temperature in metals." *Nature* **269**. 481 (1977).

- [17] J. J. Metois and J. C. Heyraud. "The overheating of lead crystals." *J. Phys. France* **50**. 3175 (1989).
- [18] A. Pavlovska, D. Dobrev, and E. Bauer. "Orientation dependence of the quasi-liquid layer on tin and indium crystals." *Surf. Sci.* **314**. 341 (1994).
- [19] A. Pavlovska, D. Dobrev, and E. Bauer. "Surface melting versus surface non-melting: an equilibrium shape study." *Surf. Sci.* **286**. 176 (1993).
- [20] J. D. van der Waals. "Over de Continuïteit van den Gas - en Vloeistoestand." Thesis. Leiden. (1873).
- [21] H. C. Hamaker. "The London/Van der Waals attraction between spherical particles." *Physica* **4**. 1058 (1937).
- [22] J. Visser. "The concept of negative Hamaker coefficients. I. History and present status." *Adv. Colloid Interface Sci.* **15**. 157 (1981).
- [23] X. J. Chen, A. C. Levi, and E. Tosatti. "Hamaker-constant calculations and surface melting of metals, semimetals and semiconductors." *Il Nuovo Cimento* **13D**. 919 (1991).
- [24] M. Y. Efremov, F. Schiettekatte, M. Zhang, E. A. Olson, A. T. Kwan, R. S. Berry, and L. H. Allen. "Discrete periodic melting point observations for nanostructure ensembles." *Phys. Rev. Lett.* **85**. 3560 (2000).
- [25] A. Yokozeki and G. D. Stein. "A metal cluster generator for gas-phase electron diffraction and its application to bismuth, lead, and indium: Variation in microcrystal structure with size." *J. Appl. Phys.* **49**. 2224 (1978).
- [26] X. F. Yu, X. Liu, K. Zhang, and Z. Q. Hu. "The lattice contraction of nanometre-sized Sn and Bi particles produced by an electrohydrodynamic technique." *J. Phys. Condens. Matter* **11**. 937 (1999).
- [27] M. G. Mitch, S. J. Chase, J. Fortner, R. Q. Yu, and J. S. Lannin. "Phase transition in ultrathin Bi films." *Phys. Rev. Lett.* **67**. 875 (1991).
- [28] V. I. Merkulov and J. S. Lannin. "Variations in atomic structure of liquid bismuth clusters." *Phys. Rev. B* **58**. 7373 (1998).
- [29] Y. Oshima, K. Takayanagi, and H. Hirayama. "Structural anomaly of fine bismuth particles observed by ultra high-vacuum TEM." *Z. Phys. D* **40**. 534 (1997).
- [30] B. D. Cullity. *Elements of X-ray Diffraction*. 2nd ed. Reading, MA: Addison-Wesley Pub. Co., Inc. (1978).
- [31] W. Klement Jr., A. Jayaraman, and G. C. Kennedy. "Phase diagrams of arsenic, antimony and bismuth at pressures up to 70 kbars." *Phys. Rev.* **131**. 632 (1963).

- [32] R. W. G. Wyckoff. *Crystal Structures*. vol. 1. 2nd ed. New York: Interscience Publishers, Inc. (1963).
- [33] X. Zeng and H. E. Elsayed-Ali. "Time-resolved structural study of low-index surfaces of germanium near its bulk melting temperature." *Phys. Rev. B* **64**. 085410 (2001).
- [34] B. Lin and H. E. Elsayed-Ali. "Temperature dependent reflection electron diffraction study of In(111) and observation of laser-induced transient surface superheating." *Surf. Sci.* **498**. 275 (2002).
- [35] J. W. Herman and H. E. Elsayed-Ali. "Time-resolved structural studies of the low-index faces of lead." *Phys. Rev. B* **49**. 4886 (1994).
- [36] G. D. T. Spiller. "Time-dependent melting and superheating of lead crystallites." *Philos. Mag. A* **46**. 535 (1982).

2.7 Figures and Tables

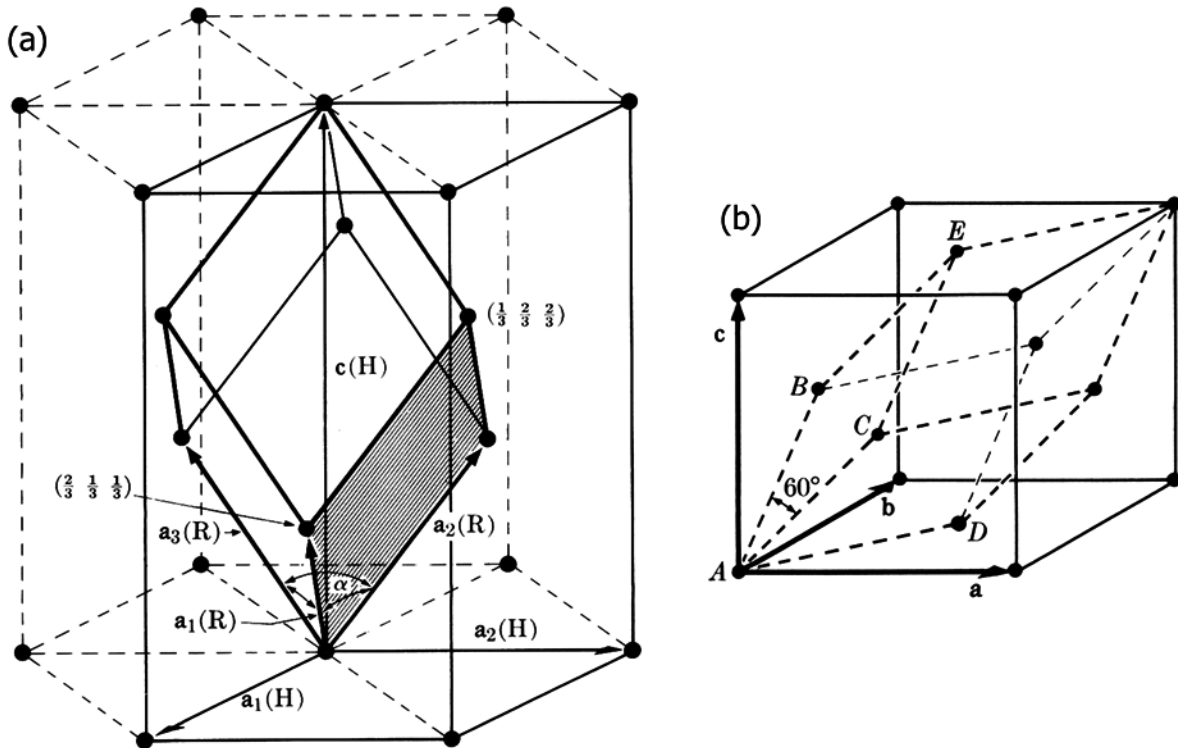


Figure 2-1: (a) The rhombohedral lattice can be written in terms of a hexagonal lattice. (b) The similarity between a rhombohedral lattice and a cubic one. In a true cubic lattice, the angle  $\alpha$  between the rhombic unit vectors is  $60^\circ$ , but in Bi, the body diagonal is slightly stretched, and  $\alpha = 57^\circ$ . Reprinted from [30].

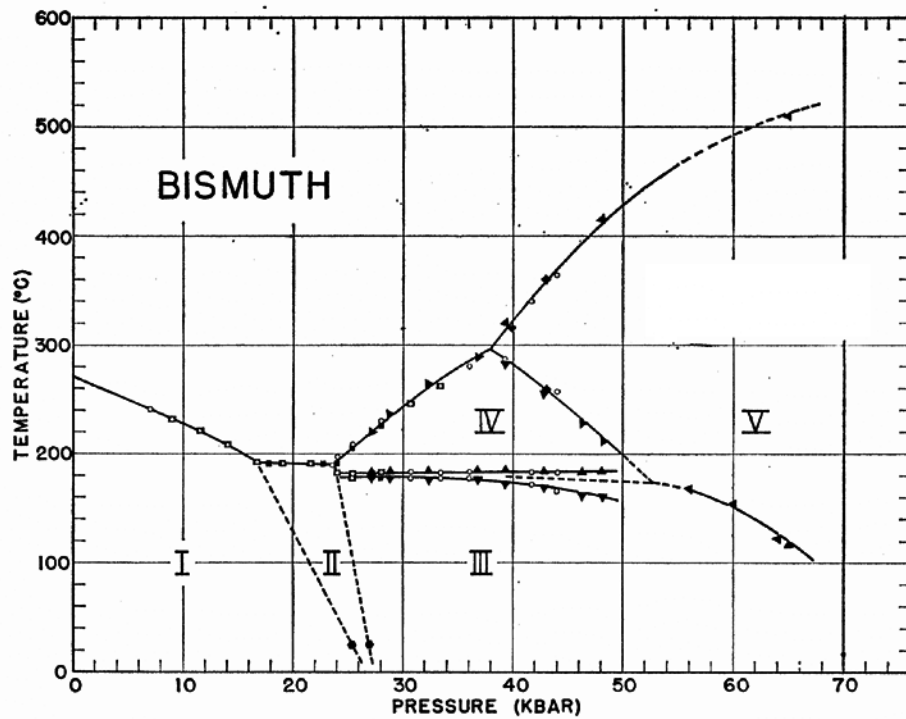


Figure 2-2: Pressure-temperature phase diagram for bulk Bi, showing several high pressure solid phases. Reprinted from [31].

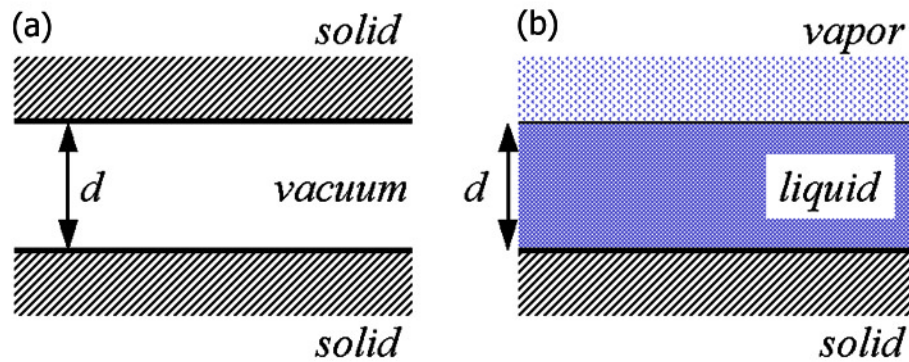


Figure 2-3: Construction commonly used in the calculation of the Hamaker constant. Part (a) shows two solid surfaces separated by vacuum at some distance  $d$ . In this case, the force between the bodies will always be attractive. Part (b) shows a large solid surface separated from its own vapor by a liquid layer. The force between the vapor and the solid will be dependent on the properties of the liquid, relative to the vapor and solid. Usually, the force will be repulsive. For some materials (e.g. Bi and Ge), the force will be attractive, and the liquid layer will thin, or even vanish.



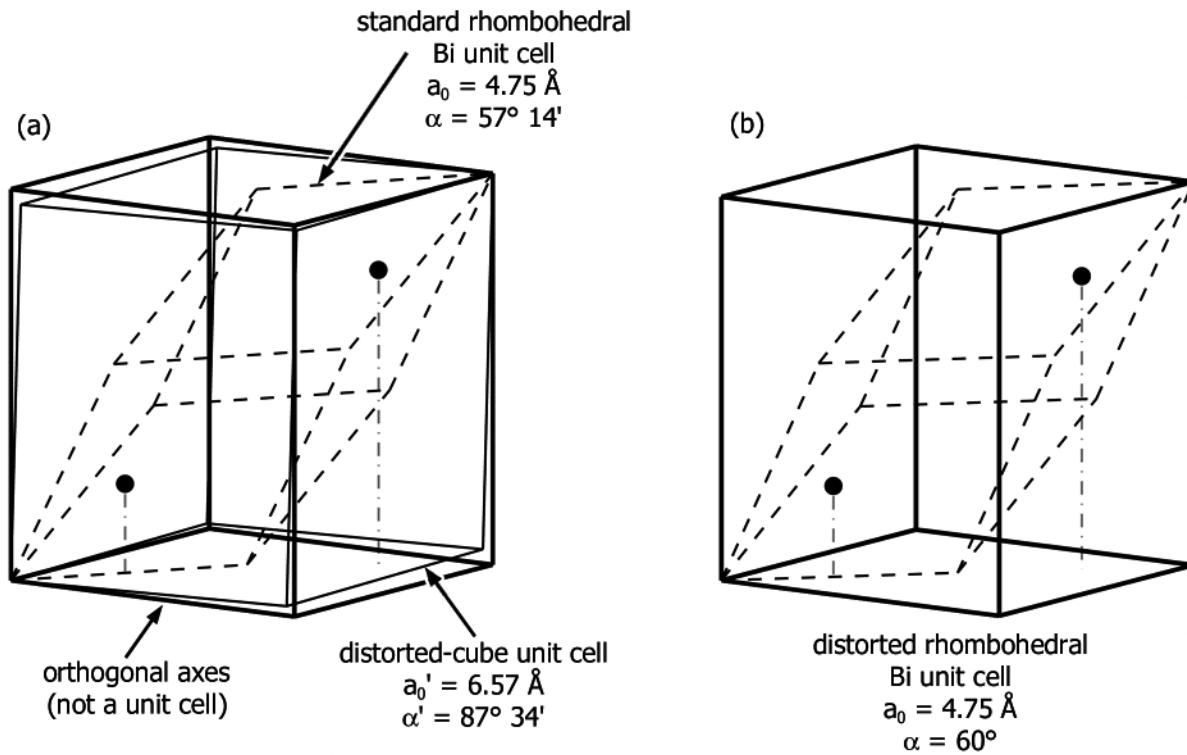


Figure 2-4: Crystal structure of Bi. (a) The standard rhombohedral unit cell of Bi, with two atoms per cell. [32] This is very similar, but slightly distorted from, a cube. (b) Some researchers have suggested that small Bi particles have a cubic structure. [29] If the Bi rhombohedron is distorted such that the angle between the rhombohedral axes is  $60^\circ$ , the unit cell can also be described as a cube, where the rhombohedron's corners are at the centers of the cube faces. Only the atoms inside the rhombohedral unit cell are shown here.

Table 2-I: Experimentally observed superheating of various elements and compounds. From [6] and references therein unless otherwise noted.

Material	$T_m$ (K)	degree of superheating (K)	Ref.
SiO <sub>2</sub> (quartz)	1700	300	
P <sub>2</sub> O <sub>5</sub>	836	50	
<i>p</i> -toluidine	318	0.6	
As <sub>2</sub> O <sub>3</sub>	551	60	
H <sub>2</sub> O	273	0.28	
Bi	544	>5	[11]
Bi(0001)	544	90	[12]
Ga	303	0.2	
Ge	1210	134	[33]
In(111)	430	73	[34]
Pb(111)	601	120 <sup>a</sup>	[35]
		2	[36]
		3	[17]
Sn	544	2	

<sup>a</sup> at  $\sim 10^{11}$  K/s

Table 2-II: Calculated Hamaker constants for several materials. The calculation was performed using frequency-dependent, complex dielectric functions. From [23].

Material	$H$ ( $\times 10^{-21}$ J)
Pb	0.3
Al	0.56
Au	0.85
Bi	< -1.3
Ge	-4.6

## Chapter 3: The Nanocalorimetry Technique

### 3.1 MEMS Sensor

The heart of the nanocalorimetry technique is the MEMS sensor, a schematic of which can be seen in Fig. 3-1 [1]. It consists of a 50 nm thick, amorphous silicon nitride ( $\text{SiN}_x$ ) membrane, supported by a Si frame. The membrane window is 3 mm  $\times$  7 mm. A patterned metal strip is deposited on one side of membrane. The strip is 50 nm thick and 0.5 mm wide. The strip is used as both a resistive heater and a resistive thermometer during the DSC measurement. The patterned metallization layer also includes two contacts for measuring the voltage drop along the metal strip. The size of these contacts is small ( $\sim 25 \mu\text{m}$  each) compared to the total length of the heater ( $\sim 7000 \mu\text{m}$ ). On the Si frame, the metallization pattern includes four contact pads, electrically connected to the strip and the voltage contacts, which serve as terminals for electrical measurements made on the membrane part of the sensor.

The total area of a typical sensor, including the supporting silicon frame, is 15 mm  $\times$  4 mm. These dimensions were chosen because such a sensor could fit intact into a transmission electron microscope (TEM) without the need to remove the membrane from the silicon support.

The region of the heater situated between the voltage contacts and the part of membrane beneath it form a calorimetric cell. Samples can be loaded onto either side of the cell ( $\text{SiN}_x$  or metallization side), except for conductive materials. Conductive materials can not be loaded on the metal side because they are able to change the electrical properties of the heater, and therefore should be placed only on the  $\text{SiN}_x$  side of the cell.

### 3.1.1 *Sensor fabrication*

Sensor fabrication is performed at the Cornell Nanofabrication Facility. The calorimetric sensor was designed to be a small device easily produced in large quantities using standard MEMS microfabrication techniques, and to have no features smaller than 10  $\mu\text{m}$ . If desired, it can be treated as a one-use, disposable item. Up to 39 sensors per 3-inch wafer are made at a time. A schematic cross section of the wafer at several steps of the fabrication process can be seen in Fig. 3-2. The fabrication sequence is as follows:

- (1) Double-side polished, (100) oriented, silicon wafers are coated on both sides with amorphous, low residual stress silicon nitride ( $\text{SiN}_x$ ) using an LPCVD process. Double-side polished wafers are required for photolithography on both sides of the wafer. The thickness of the  $\text{SiN}_x$  varies from about 30 to 1000 nm, depending on the application. Thicker  $\text{SiN}_x$  gives greater mechanical durability, but leads to larger heat losses. Optionally, a thermally grown  $\text{SiO}_2$  layer between the wafer and  $\text{SiN}_x$  can be made. The utility of such a layer will be discussed below.
- (2) On the back side of the wafer, a rectangular area of the  $\text{SiN}_x$  is patterned using optical lithography. Shipley 1813 general purpose broad band (365 nm – 436 nm) positive photoresist with MicroPrime P-20 primer are used for coating. A 5x g-line (436 nm) stepper (GCA-6300) is used for photolithography. After developing, the exposed part of the  $\text{SiN}_x$  layer is etched away by reactive ion etching (RIE) using  $\text{CF}_4$ . Since any damage to the unpatterned face of the wafer will create defects in the finished sensors, that face is protected during handling with a front-side coating of unexposed photoresist. Both front and rear side coatings are removed with acetone and 2-propanol after the RIE step.

- (3) The wafer is etched in a 35 wt% KOH solution at 80 °C to remove Si exposed in the previous step. The etch rate for these conditions is  $\sim 1 \mu\text{m}/\text{min}$ . KOH has a high selectivity for silicon over silicon nitride. It also etches Si anisotropically, with a (100):(111) etch ratio of  $\sim 400:1$  [2]. The resulting structure is a very thin  $\text{SiN}_x$  membrane on the front side of wafer, supported by a Si frame. Wafers must be oriented vertically in the etchant, as vigorous bubbling can rupture the membranes. The end of the etching process is marked by the cessation of any bubbling action.
- (4) After washing in hot (65 °C) and then cold (25 °C) water, the wafer is then isotropically etched in a solution of 450 mL  $\text{HNO}_3$  : 225 mL  $\text{H}_2\text{O}$  : 3 mL HF for 5 min. This removes any microscopic residual Si pyramids with (111)-oriented faces. This etchant is not selective to Si, and etches  $\text{SiN}_x$  at  $\sim 0.5$  to 1 nm/min. This etch step can be prolonged to thin the nitride membrane. Typically, this step reduces the  $\text{SiN}_x$  thickness by  $\sim 5$  nm. This factor should be taken into account when selecting the initial  $\text{SiN}_x$  thickness. Since wafers have extremely fragile nitride windows in this and subsequent steps, great care is required in the handling of wafers, especially during washing and drying. (Only gentle flows of solvents and dry air/nitrogen at small angles to the wafer surface should be used.)
- (5) A patterned metal layer is deposited on the front side of the wafer using the lift-off technique. Photoresist is applied on the front side of wafer using the same reagents as in step (2) and exposed by the same stepper. Membranes usually survive the regular spin-coating process with special chucks, but no vacuum should be used. A non-contact method of photolithography is mandatory at this step because direct contact would break the  $\text{SiN}_x$  membranes. An ammonia diffusion process in a YES LP-III vacuum oven is

used to reverse the tone of the patterned image and to generate an undercut profile for successful lift-off. After developing, the metal layer is deposited onto the wafer using thermal or electron beam evaporation. The thickness of this layer is typically ~50 nm. The material used for the metallization is usually Al, Au, or Pt. Deposition of a thin (~3 nm) layer of Ti before the main metallization is usually necessary to promote adhesion of the following layer. Lift-off is performed using acetone as a solvent. To ensure high quality sensors, care should be taken to completely remove all photoresist residue.

- (6) Individual sensors are cleaved from the wafer manually. Narrow lines etched into the wafer in step (3) help the accuracy of the cleaving. To clean the surface and remove any residue, they are washed before use in sequential baths of acetone, 2-propanol, and deionized water.

### ***3.2 Temperature Calibration***

Since the metal layer on a sensor will be used as both a heater and a temperature sensor, it must be annealed so that its resistance is stable with respect to temperature and calibrated to determine the response of its electrical resistance to temperature. This is done in a three-zone vacuum tube furnace. First, sensors are typically annealed in vacuum of  $\sim 10^{-8}$  torr at 450 °C for 8 h. Second, sensors are “burned in” under the same vacuum conditions using a DC electrical pulse to heat the sensor to a temperature higher than that needed for the experiment. Three to ten thousand pulses are used to burn in and stabilize each sensor. Calibrated sensors with Au, Ni or Pt metallizations can be kept in air at least for several months without noticeable degradation of their electrical characteristics. Immediately before a calorimetric experiment, the burning-in process is repeated inside the deposition chamber.

The temperature calibration is performed by increasing the furnace temperature from room temperature to  $\sim 350$  °C, and the slowly cooling back to room temperature. The 4-point resistance of the sensor is measured throughout this process by an Hewlett-Packard 34420A microohmmeter. The resistance of the sensor as a function of temperature is then determined, and a fourth-order polynomial  $T(R)$  is fitted.

### ***3.3 Experimental Setup***

After two sensors are prepared and calibrated, they are placed in a vacuum chamber. The samples described here are metal films deposited by thermal evaporation. The calorimetry is done *in situ* with the evaporation, either simultaneous with or after the deposition. The vacuum chamber is diffusion pumped to  $\sim 5 \times 10^{-8}$  torr before evaporation and calorimetry.

Bi vapor consists of Bi atoms and Bi<sub>2</sub> dimers [3]. The evaporated Bi does not necessarily deposit on those and only those surfaces with a direct line-of-sight to the evaporation source. Some fraction of the evaporated Bi behaves like a diffuse gas, and it can deposit on surfaces that have no visibility to the source. In the case of an Au sensor, a small Bi deposition can cause the resistance, and therefore the apparent temperature, of a sensor to increase. To prevent this, the sensors are enclosed in a box in the vacuum chamber. So that gas in the box can be pumped out, small holes with a total surface area of  $\sim 2$  cm<sup>2</sup> are cut into the walls of the box. No increase in the starting temperature of sensors was detected after they were placed in the box, even after a 150 nm Bi deposition.

### ***3.4 Calorimetric Pulsing***

The calorimetric scan is initiated by applying a short (milliseconds) DC electrical current (tens of milliamperes) through the metal strip. The calorimetric cell heats by resistive heating,

while the part of the strip placed on the Si frame remains cold due to the high heat capacity of the Si frame (in comparison with the  $\text{SiN}_x$  membrane). The current  $I$  through the sensor and the voltage  $V$  across it (typically a few volts) are measured as functions of time  $t$ . The resistance of the sensing area of the heater is calculated as  $R(t) = V(t)/I(t)$  and the electrical power generated in the calorimetric cell as  $P(t) = I(t)V(t)$ . The  $R(t)$  function is used then to calculate the temperature  $T(t)$  of the sensing part of the metal strip, using the previously determined  $T(R)$  relationship.

To take advantage of a differential measurement, two identical sensors are used: a sample sensor, containing the material being measured, and a reference sensor, with no added material. DC current pulses through the sensors are precisely synchronized. Five voltage measurements are made simultaneously in this differential scheme: currents through sample and reference sensors  $I_S$  and  $I_R$ , respectively (measured as voltages across known resistors); voltages across sample and reference sensors  $V_S$  and  $V_R$ , respectively; and the differential signal, the voltage  $\Delta V$ . The  $\Delta V$  value reflects the difference between sensors made by the presence of the sample on one of them. Generally,  $\Delta V = V_S - V_R$ . The principal circuitry in the differential measurement is shown in Fig. 3-3. The sampling rate for electrical measurements is typically 100 kHz, which corresponds to a temperature resolution of 0.3 K/sample for a heating rate of 30 kK/s.

### 3.5 Data Analysis

With a large sample and a large signal, only  $V_S$  and  $I_S$  are needed to calculate heat capacity  $C_P$ . Since the electrical power dissipated in the calorimeter is  $P(t) = I(t)V(t)$ ,  $C_P$  can be found by:

$$C_P(T(t)) = \frac{dQ}{dT} = \left( \frac{dQ}{dt} \right) \left( \frac{dT}{dt} \right)^{-1} = P(t) \left( \frac{dT}{dt} \right)^{-1} \quad (3-1)$$



where  $T$  can easily be found from the previously-determined  $T(R)$  relationship. Just using Eq. (3-1) on a calorimeter with a sample will result in calculating the sum of the heat capacities from the sample and the calorimetric cell ( $C_P^X + C_P^{cell}$ ). To determine the heat capacity of only the sample  $C_P^X$ , a value for  $C_P^{cell}$  is determined using a series of calorimetric pulses made before any sample has been deposited on the sensor, and this baseline value subtracted from ( $C_P^X + C_P^{cell}$ ).

When the sample is very small, however, the  $dT/dt$  term in Eq. (3-1) is noisy, and any peak can be hidden in the noise. In this case, a differential method is used, where one sensor contains the sample of interest, one sensor has no sample, and the difference between them is measured in the form of a differential voltage  $\Delta V$ .

Eq. (3-1) can be applied to both the reference and sample sensors:

$$C_P^{cell,R} = I_R V_R v_R^{-1} \quad (3-2)$$

$$C_P^{cell,S} + C_P^X = I_S V_S v_S^{-1} \quad (3-3)$$

where the definition  $v_i = dT/dt$  has been introduced.

Two assumptions are now made. Firstly, that the sensors are sufficiently similar that:

$$C_P^{cell,R}(T) = C_P^{cell,S}(T) = C_P^{cell}(T). \quad (3-4)$$

Secondly, that any difference in temperature between the two sensors is small at any given  $t$ , or:

$$C_P^{cell}(T_S(t)) = C_P^{cell}(T_R(t)). \quad (3-5)$$

Fabricating many sensors on a single Si wafer, and using sensors close to each other from that wafer, makes the assumption in Eq. (3-4) reasonable. If the sample deposited onto the sample sensor is small, any perturbation to the heating characteristics will also be small, and Eq. (3-5) will be reasonable.

Using these assumptions, Eqs. (3-2) and (3-3) can be combined to give:

$$C_P^X = \frac{I_R V_R}{v_R} \left[ \left( \frac{v_R}{v_S} \right) \left( \frac{\Delta V}{V_R} + 1 \right) \left( \frac{I_S}{I_R} \right) - 1 \right]. \quad (3-6)$$

Unfortunately, the  $v_R/v_S$  term is very noisy, since it is the ratio of two numerical derivatives.

Using the definition  $\Delta V = V_S - V_R$  and differentiating:

$$\frac{v_S}{v_R} = \frac{\left( \frac{d\Delta V}{dt} \right)}{\left( v_R \frac{dV_S}{dT} \right)} + \frac{\left( \frac{dV_R}{dT} \right)}{\left( \frac{dV_S}{dT} \right)} \quad (3-7)$$

Since  $V = IR$ ,

$$\frac{dV}{dT} = I \frac{dR}{dT} + R \frac{dI}{dT} \quad (3-8)$$

which holds true for both the sample and reference branches of the circuit. Using the previously-determined polynomial  $R(T)$ ,  $dR/dT$  has no noise. The  $I(T(t))$  term is hardware-dependent, but can be modeled by an empirical function [4].

Raw data from the calorimetric pulse, as well as the final heat capacity curve can be seen in Fig. 3-4 for a 10 nm Bi film. The heating rate for this case is  $\sim 40$  kK/s, and the sensor had an Al metallization. Results from both the sample and reference sensors are shown.

### 3.6 LED Pulsing

There was some initial concern whether heat conduction through the thickness of the film could cause problems with the calorimetry or if there was some sort of thermal resistance at the interface between the sample film and the nitride. To determine if these factors were present, a 50 nm Bi film was deposited on a sensor, and a blue LED shined on the location of the Bi film. A blue LED was chosen because of its high brightness, the low current needed to operate it, and

its fast rise time. The LED was pulsed for either 0.1 ms, 0.5 ms, or 2 ms, and synchronized to start 1 ms after the start of the calorimetric pulse.

Fig. 3-5 shows the results of the LED pulsing. Fig. 3-5(a) shows the experimental setup and the location of the LED. Fig. 3-5(b) shows the effect the LED pulse has in the  $d(\Delta V)/dt$  signal, and Fig. 3-5(c) shows the effect in the final heat capacity curve. Melting is endothermic, and appears in the caloric curve as a peak. The LED acts as a source of energy (exothermic) and appears in the caloric curve as a trough. Fig. 3-5(d) shows that the heat (i.e. integrated area) in the LED trough scales with the length of the pulse, as expected.

There do not appear to be any thermal resistance or heat conduction effects. The response of the calorimeter to the LED pulse is within one or two data points, and the LED pulse probably is not synchronized any more accurately than that. If these effects are present, they should not effect the caloric curve for any Bi film under 50 nm, at least with the current 100 kHz data collection rate.

The 50 nm thickness of the film was chosen because it was expected that this would be a continuous film, not one made of metal particles. Optical microscopy and SEM done later, however, show that even a film 150 nm thick is not continuous, if it has been melted. Films in this thickness range can be made up of particles with radii up to  $\sim 1 \mu\text{m}$ .

This method could be used to calibrate the accuracy of the nanocalorimeter, if the output of the LED were known. It might also be necessary to take into account any reflected or transmitted light, which might require some additional knowledge of the optical properties of the sample film and/or sensor.

### 3.7 Particle Counting

The ultimate goal in these experiments is to correlate the calorimetry data with the size of the particles in the sample. Therefore, it is necessary to measure the size of the particles. Since they are self-assembled, the nanoparticles are not monodisperse in size, but, rather, have a definite size distribution. Using a cluster beam system, where size selection of in-flight particles can take place, this may be avoided in the future.

To determine the range of particle sizes in a particular sample that reflects a particular set of calorimetric data, *ex situ* TEM is done on each sensor after the calorimetry. Because of the thin film nature of the sensors, the membrane is thin enough that images of the particles on the membrane can be obtained. A shadow mask is usually used to limit the area of deposition on the sensor to only the heater (i.e. the active area of the sensor), but a small  $\sim 400\ \mu\text{m}$  notch is cut into the mask. This ensures that a small amount of the film is deposited extending off the heater onto just the  $\text{SiN}_x$  membrane. (TEM imaging through the metal heater can be problematic.) Close to the edge of the heater, less than a few microns, the sample is hot enough to have been melted, and resembles the sample on the heater itself.

Several TEM micrographs are taken for each calorimetric sample. If taken using film rather than a CCD camera, the film is scanned to get digital images. To remove background noise, each image is thresholded (i.e. converted to a black/white-only image). These images are analyzed (ScionImage, Scion Corp.) to determine the projected area for each of a large number of particles. From that area, a radius for each particle is determined ( $r = \sqrt{A/\pi}$ ) and a particle surface density as a function of radius  $h(r)$  is determined. Since particles will contribute to any melting signal proportionally to their volume, not their radius, the  $h(r)$  distribution is usually multiplied by the volume of a particle for each histogram bin. It is usually more insightful to

refer to this “volume histogram.” This process also has a tendency to emphasize the contribution from larger particles. Examples of the TEM micrographs, the thresholded version of those images, and the resulting volume histograms can be seen in Fig. 3-6.

### 3.8 Mapping

The next step is to correlate a particular particle size with a particular melting temperature. It is assumed that all particles of a particular size melt completely once they reach a certain temperature. First, an average heat of fusion  $H_m^{TEM}$  is determined by:

$$H_m^{TEM} = \frac{\int_{T'}^{T_{max}} [C_P(T) - C_P^0] dT}{S \int_{r'}^{\infty} \frac{4}{3} \pi r^3 \rho_S h(r) dr} \quad (3-9)$$

where  $T_{max}$  is the end of the caloric curve,  $C_P^0$  is the heat capacity baseline,  $S$  is the surface area of the active part of the sensor, and  $\rho_S$  is the solid phase density. Since the heat capacities of solids are approximately constant, the average heat capacity between 40 °C and 60 °C is usually used for  $C_P^0$ .

To determine a  $T_m(r)$  relationship, the caloric curve and particle size histograms are examined separately, and the following two relationships calculated for each  $T$  and  $r$ :

$$A \equiv H_m^{TEM} S \int_{r'}^{\infty} \frac{4}{3} \pi r^3 h(r) dr, \text{ and} \quad (3-10)$$

$$B \equiv \int_{T'}^{T_{max}} [C_P(T) - C_P^0] dT. \quad (3-11)$$

For each radius  $r$ , there is one corresponding temperature  $T$  where  $A = B$ , which is taken as  $T_m(r)$ . This process is shown graphically in Fig. 3-7.

This method has previously been used to determine  $T_m(r)$  for In [5]. The results of the mapping procedure can be seen in Fig. 3-8(a) for a series of films of varying thickness. An

average  $T_m(r)$  is seen in Fig. 3-8(b), along with the behavior predicted by different melting models. The HMM matches the experimental data quite well.

### 3.9 References

- [1] E. A. Olson, M. Y. Efremov, M. Zhang, Z. S. Zhang, and L. H. Allen. "The design and operation of a MEMS differential scanning nanocalorimeter for high-speed heat capacity measurements of ultrathin films." *J. Microelectromech. Syst.* **12**. 355 (2003).
- [2] G. T. A. Kovacs. *Micromachined Transducers Sourcebook*. Burr Ridge, IL: WCB/McGraw-Hill. (1998).
- [3] A. Kawazu, T. Otsuki, and G. Tominaga. "Growth of bismuth layers on Si(100) surfaces." *Jpn. J. Appl. Phys.* **20**. 553 (1981).
- [4] M. Y. Efremov, E. A. Olson, M. Zhang, S. Lai, F. Schiettekatte, Z. S. Zhang, and L. H. Allen. "Thin-film MEMS differential scanning nanocalorimetry: Heat capacity analysis." *Thermochimica Acta*. submitted (2003).
- [5] M. Zhang, M. Y. Efremov, F. Schiettekatte, E. A. Olson, A. T. Kwan, S. L. Lai, T. Wisleder, J. E. Greene, and L. H. Allen. "Size-dependent melting point depression of nanostructures: Nanocalorimetric measurements." *Phys. Rev. B* **62**. 10548 (2000).

3.10 Figures

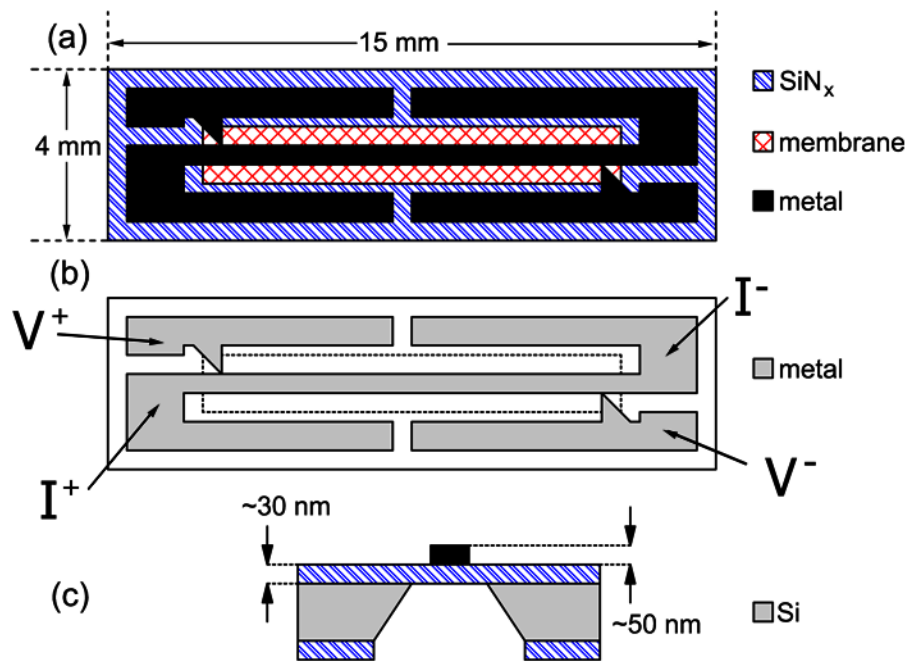


Figure 3-1: Schematic of the MEMS sensor, not to scale. (a) A top view showing the location of the SiN<sub>x</sub>, the membrane, and the metallization. (b) The metallization showing the electrical connections. (c) A cross section, showing the location of the membrane and metal heater.

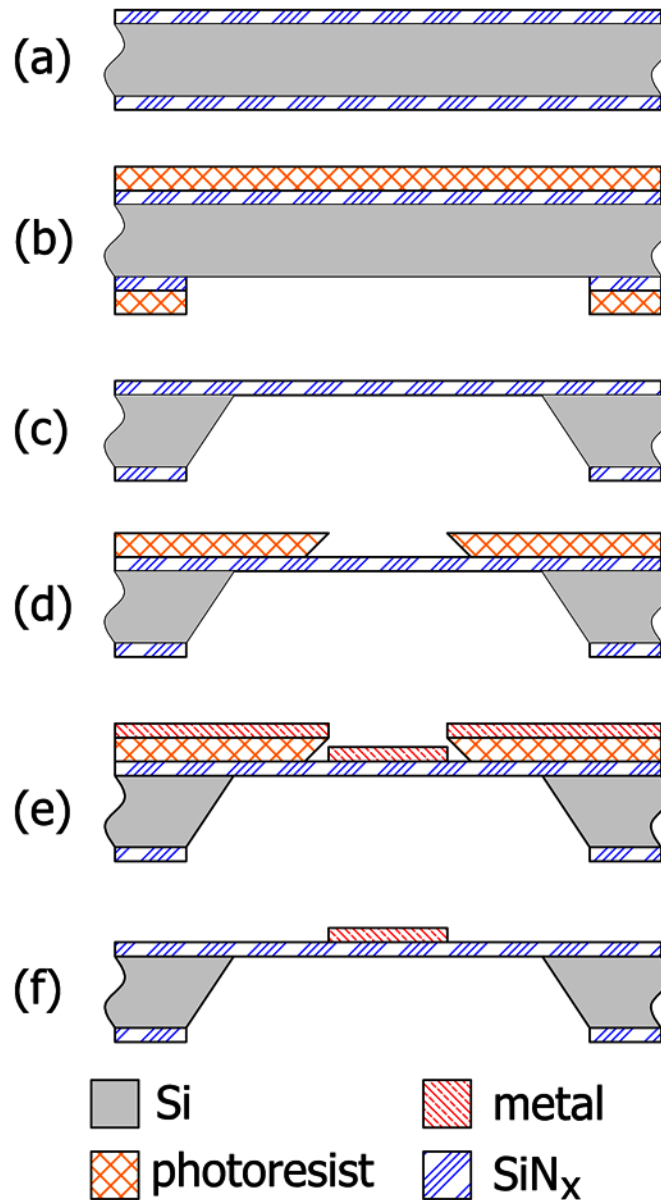


Figure 3-2: Sensor fabrication process. (a) The process starts with a silicon wafer with  $\text{SiN}_x$  deposited on both sides. (b) Photoresist (PR) is spun on both sides, then one side is patterned and reactive-ion etched. (c) The PR is stripped off and the Si is etched using an 80 °C KOH solution. (d) Another PR layer is spun on, patterned, and developed so that a liftoff profile is created. (e) Metal is deposited uniformly on the wafer. (f) The PR and excess metal is removed in an acetone bath.



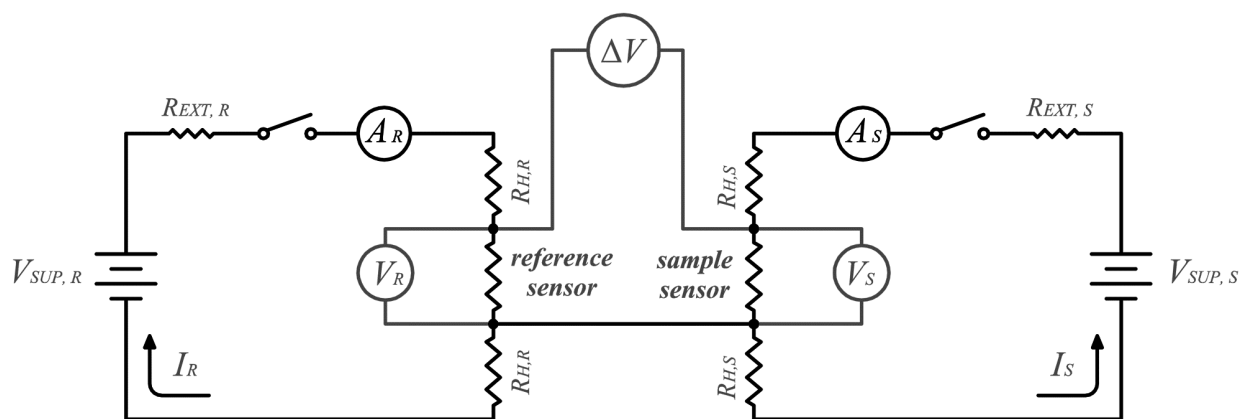


Figure 3-3: Electrical schematic of a differential nanocalorimetric experiment. Shown are: supply voltages  $V_{SUP}$ , adjustable resistances  $R_{EXT}$ , ammeters  $A$ , voltages across each calorimetric sensor  $V$ , currents  $I$ , and the differential voltage  $\Delta V$ . The small section of each sensor that is heated, but not included in the voltage measurement is represented here as  $R_H$ . The  $R$  and  $S$  subscripts denote the reference and sample branches of the circuit, respectively.

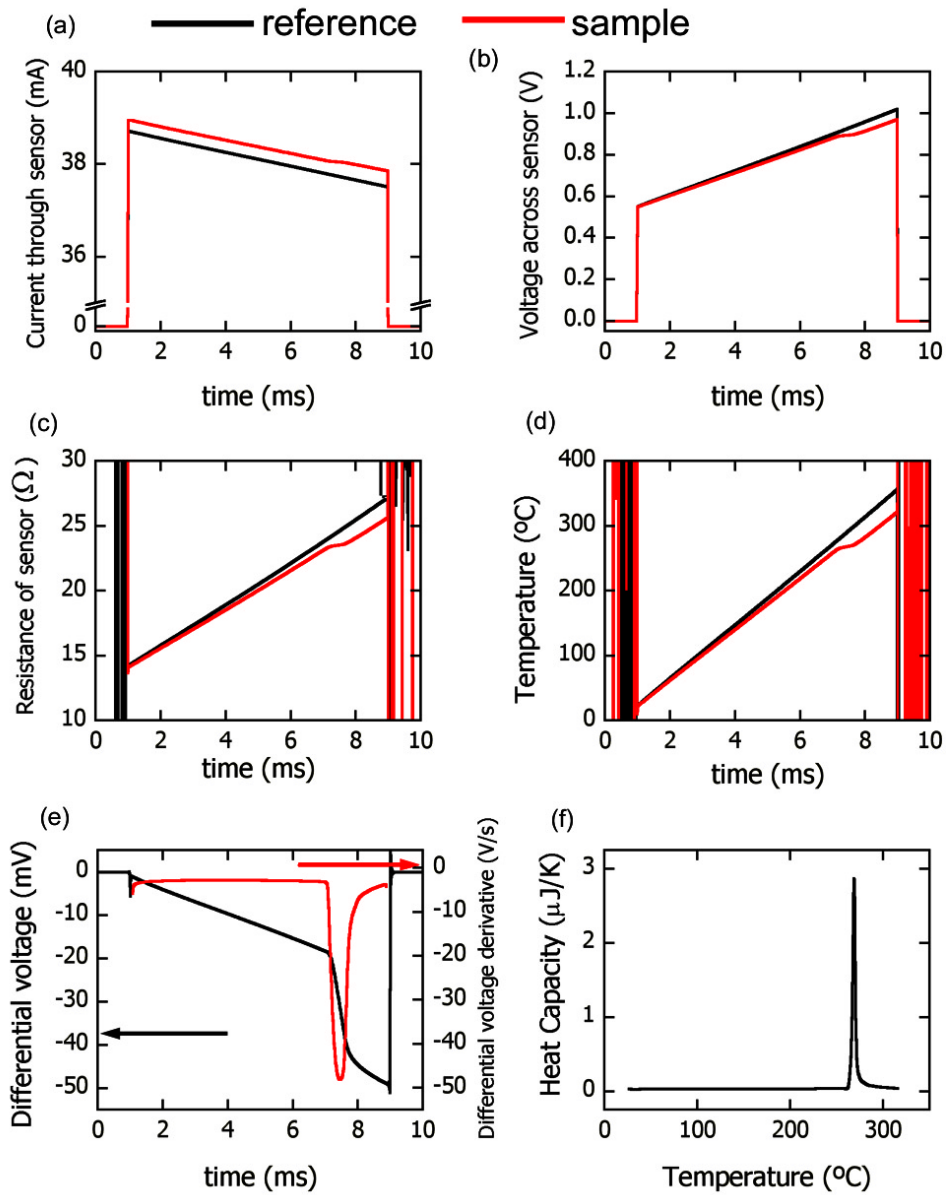


Figure 3-4: Typical experimental data for a 10 nm Bi film on a sensor with an Al metallization. (a)  $I_S$  and  $I_R$ . (b)  $V_S$  and  $V_R$ . (c)  $R_S$  and  $R_R$ . (d)  $T_S$  and  $T_R$ . (e)  $\Delta V$  and  $d(\Delta V)/dt$ . (f) The final heat capacity curve. The heating rate in this case was  $\sim 40$  kK/s.

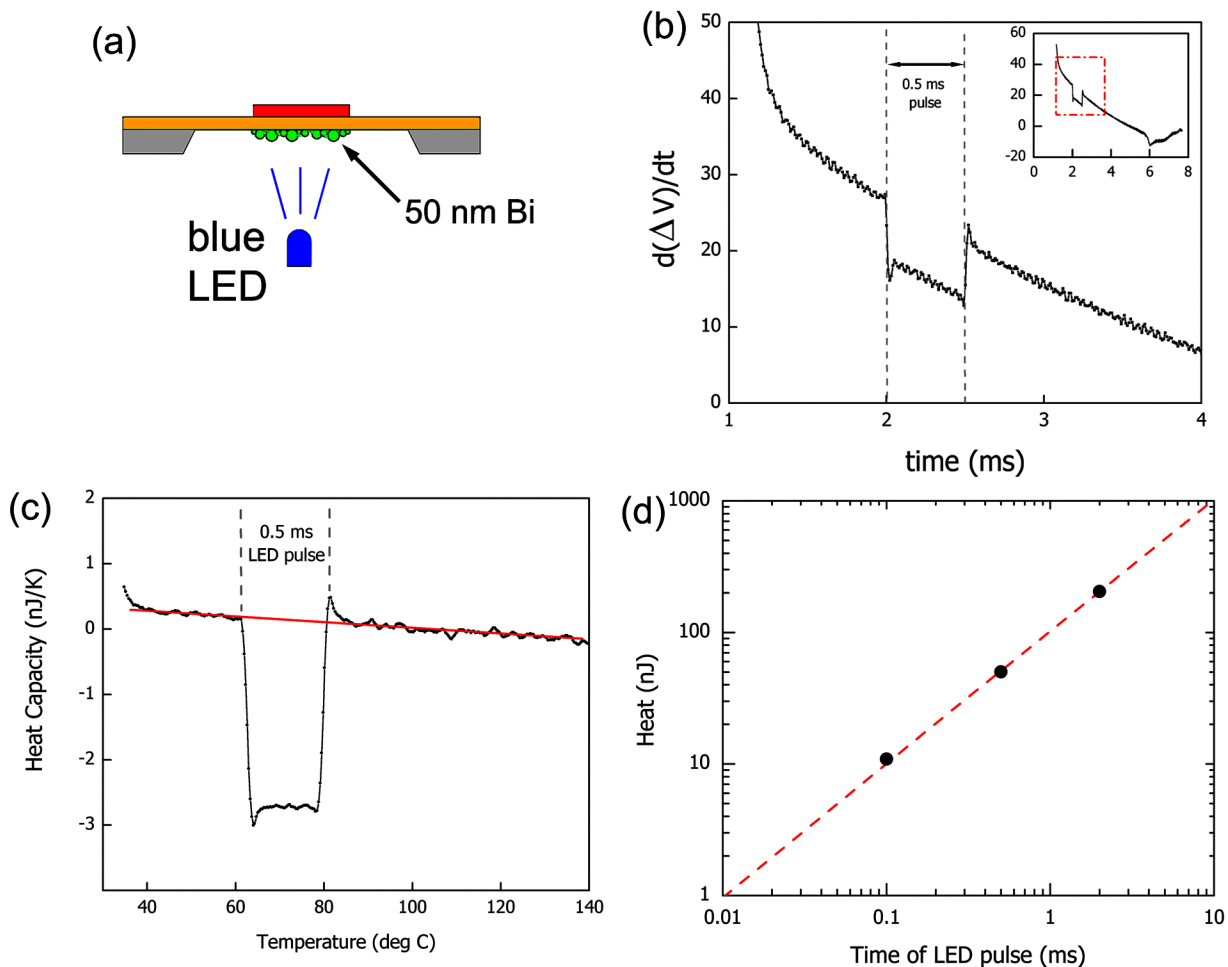


Figure 3-5: Results of calorimetric scan synchronized with an LED pulse. (a) The experimental setup. A 50 nm Bi film was deposited onto the calorimeter, and a blue LED used to flash onto the sensor area 1 ms into the 7 ms calorimetric scan. (b) The LED pulse is visible in the  $d(\Delta V)/dt$  data. (c) The effect of the LED pulse on the calorimetric scan itself. Since the LED supplies energy, it has an effect similar to an exothermic reaction, and  $C_p$  curve decreases. (d) The amount of heat under the LED pulse trough in (c) scales linearly with the length of the pulse.

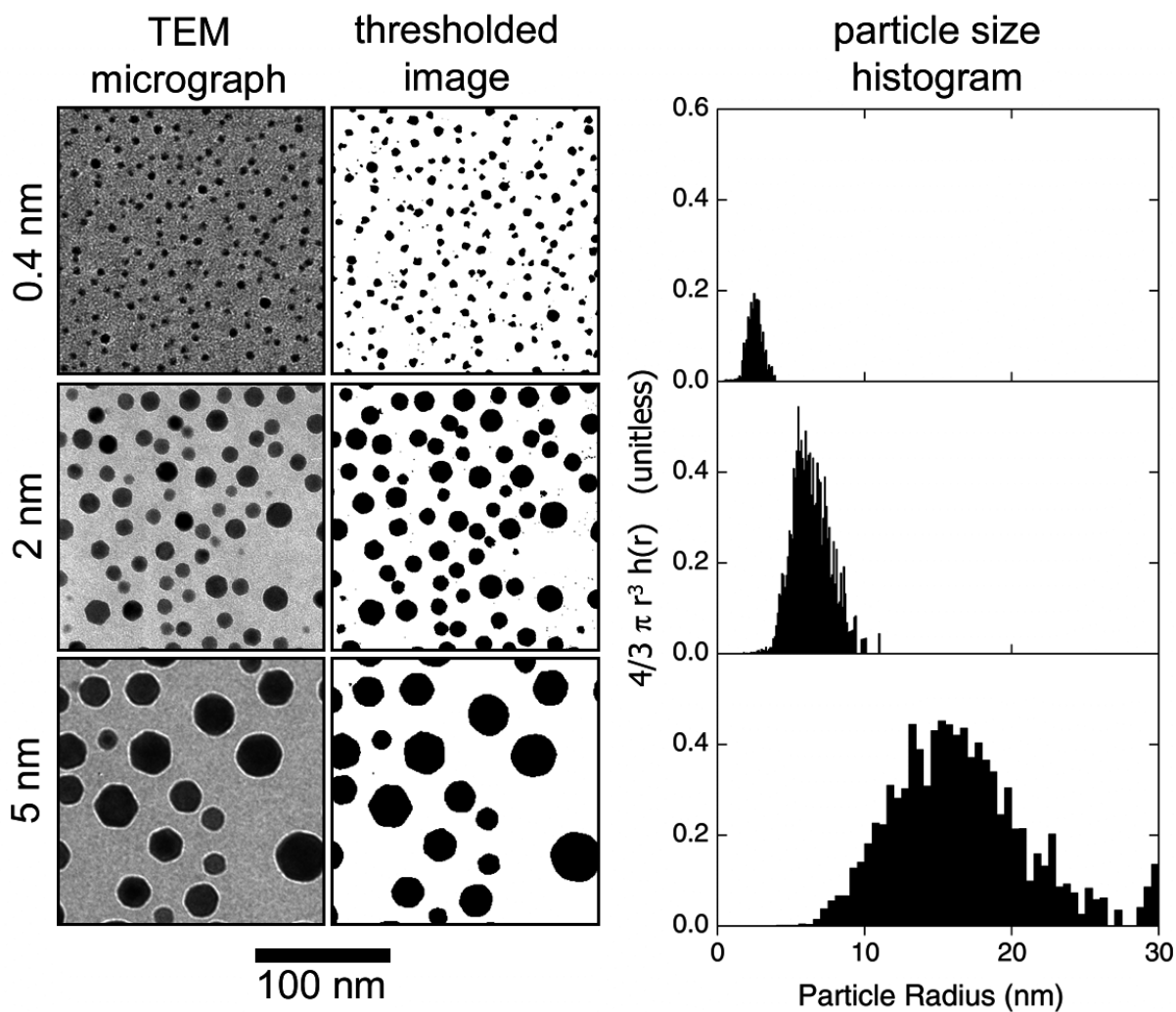


Figure 3-6: Particle counting. Shown are TEM micrographs, thresholded images, and calculated particle size histograms for 0.4 nm, 2 nm, and 5 nm Bi films. In the histogram, the number density of particles  $h(r)$  has been multiplied by the volume of each bin,  $4/3\pi r^3$ . The histogram has also been divided by the bin size so that the integrated area represents the average film thickness.

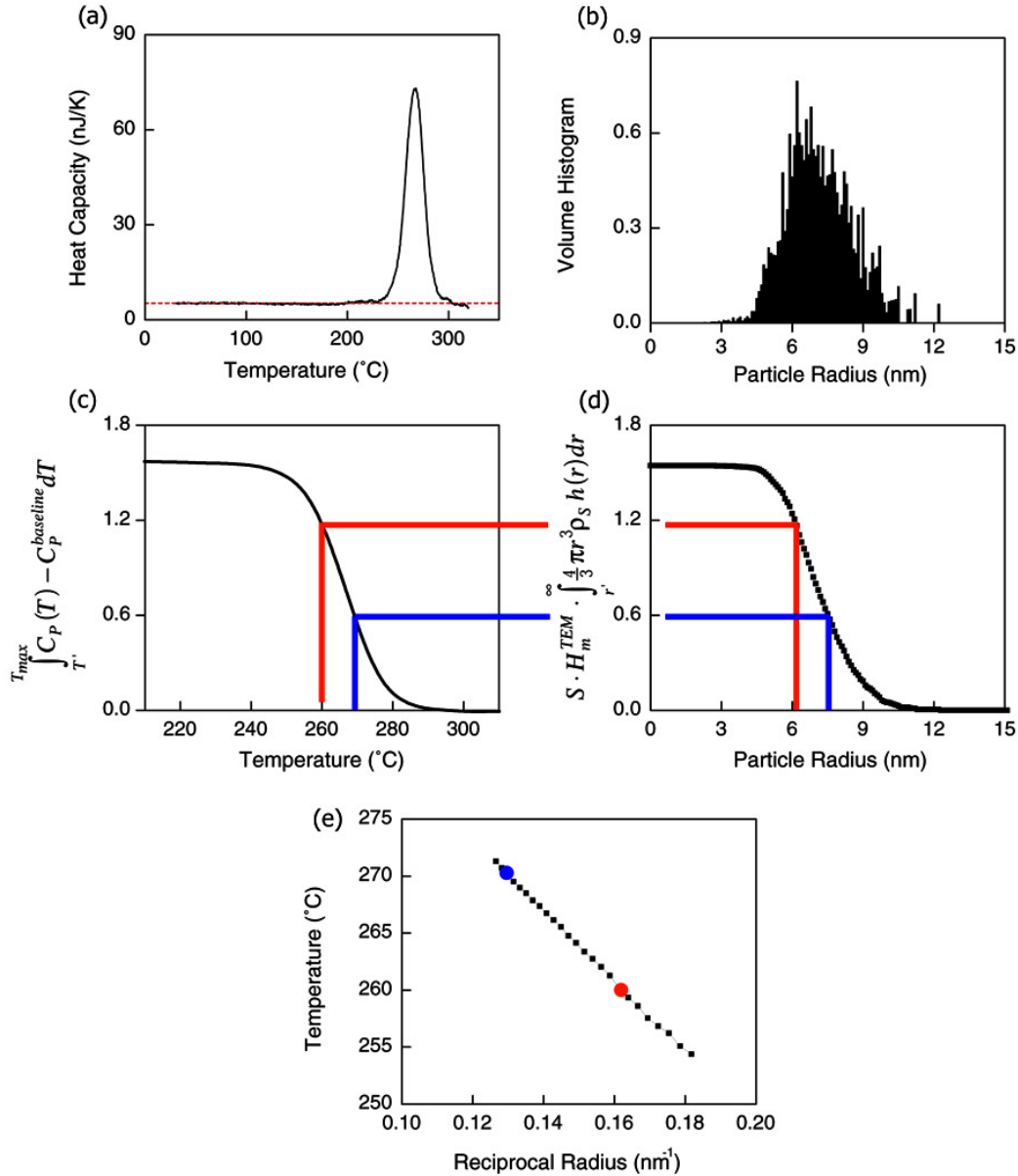


Figure 3-7: Mapping of calorimetry data to particle size for a 2 nm Bi deposition. (a) The results of a calorimetric scan. (b) The particle size histogram. Here, the particle number density  $h(r)$  has been multiplied by the volume of a particle in each bin. (c) The integrated calorimetric data. (d) The integrated particle size data. (e) The resulting mapped relationship between melting temperature and particle radius. Blue and red lines in (c) and (d) show how one temperature is connected to a particular particle size, and correspond to blue and red dots in (e).

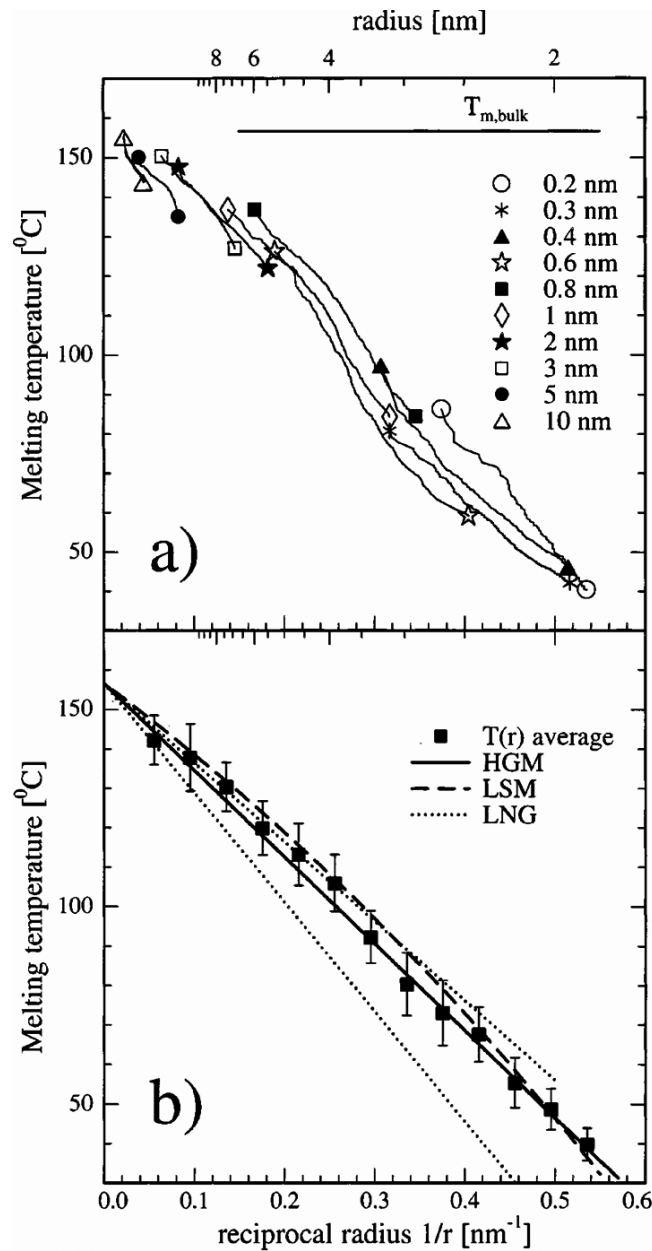


Figure 3-8: Mapping procedure as applied to indium experiments. (a) The results from a series of films ranging from 0.2 to 10 nm. (b) Averaged  $T_m(r)$  data, along with expected values using various melting models. The data fits the HMM (HGM in the figure) well. Reprinted from [5].

## Chapter 4: Bismuth

### 4.1 Radius vs. Thickness

As the average film thickness increases, the size of melted particles also gradually increases. In the as-deposited state, thin films consist of small, irregularly shaped platelets. Upon melting, the material forms rough spheres. Cooling and subsequent pulsing does not significantly change the shape of the particles. This can be seen in Fig. 4-1. A Bi film nominally 5 nm thick, in its as-deposited (cold) state, consists of platelets that are polygonal in cross section. After pulsing, the particles are circular in cross section. The In films are similar, although the cold particles are not as highly faceted.

For In, this trend continues at higher thicknesses, the particles just increase in size. An unheated, 10 nm Bi film no longer consists of discrete, irregular particles, but of a loosely interconnected network. Upon melting, this film forms spheres much larger than would have been predicted from the thinner films. This trend is shown in Fig. 4-2 for Bi, In, and Sn. Films 5 nm and below form particles of approximately the same size. At 10 nm thick, the Bi particles touch and the average particle size upon melting increases dramatically.

This change in behavior can be exploited to form bimodal distributions of particle size. Fig. 4-3 shows such a bimodal distribution. First, 10 nm of Bi is deposited and heated to form large particles with radii between 15 and 60 nm. Then, an additional 0.8 nm Bi is deposited to form small particles with radii under 10 nm. A TEM micrograph and particle size histogram can be seen in Fig. 4-3(a) and Fig. 4-3(b), respectively. The heat capacity data for these films before and after the 0.8 nm Bi deposition is shown in Fig. 4-3(c). The 0.8 nm deposition does not significantly modify the large melting peak at 260 °C. Instead, the smaller radii of the second set of particles and the size-dependence of  $T_m$  create a second melting peak at ~225 °C.

## 4.2 Heat Capacity and Heat of Fusion

Heat capacity curves for two Bi films can be seen in Fig. 4-4. The thicker film, at 1.0 nm average thickness has larger particles and, therefore, a higher average melting temperature. The 0.4 nm film has smaller particles and the average melting temperature is lower. Since there is less material in the 0.4 nm film, its latent heat is also smaller, and the integrated area under the peak is smaller. A quartz crystal monitor (QCM) is used to measure the nominal film thickness during deposition.

Heat capacity is not expected to be size-dependent. As such, it should be proportional to the mass of material deposited on the sensor surface, and can be calculated by:

$$m = \frac{C_p(T)}{c_p(T)} \quad (4-1)$$

where  $m$  is the mass of the deposited sample and  $\overline{c_p}(T)$  is the specific heat (i.e. heat capacity per gram) of the sample substance. For Bi,  $\overline{c_p}(T) = 54.1$  J/g. The latent heat of fusion can be calculated from heat capacity information by integrating the area under the melting peak. [1] Measured heat capacity and latent heat of fusion values, along with the expected bulk values for each, are shown in Fig. 4-5(a) and Fig. 4-5(b) as functions of the nominal film thickness for twenty-three films. There may be a difference in the amount of Bi that sticks to the SiN<sub>x</sub> surface of the calorimeter and the amount that sticks to the Bi-coated surface of the QCM. Therefore, heat of fusion as a function of the mass calculated using Eq. (4-1) is shown in Fig. 4-5(c).

## 4.3 Continuous Heat Capacity Measurement

Since the calorimetry is done *in situ* to the film deposition, it is possible to measure the thermal properties of a film simultaneously with its deposition. An example of this can be seen in Fig. 4-6. Here, 10 scans are taken at a rate of 1 scan/s and the results averaged. The deposition



rate was very slow, about 0.001 nm/s. The slow development of a melting peak can be seen as the film grows.

The total deposition in this experiment was 2 nm. The  $C_P$  and  $H_m$  values from the calorimetric data, however, are consistent with a deposition of only  $\sim 0.1$  nm. The discrepancy may be due to a difference in sticking coefficient between the sensor with its  $\text{SiN}_x$  surface and the QCM surface that had been coated with Bi during previous experiments. Also, small liquid droplets have a higher vapor pressure than the bulk. During a very slow deposition, it would be expected that the initial particles formed would be quite small, and may therefore be evaporated from the sensor surface rather than coalesced into larger particles. The fact that there is little melting point depression at the end of the deposition suggests that the film was made up of a small number of large particles, but this was not verified microscopically.

#### ***4.4 Heat Capacity Dependence on Heating Rate***

Ideally, the response of the calorimetric sensor would be independent of the heating rate used in an experiment. In these experiments high heating rates are used to achieve as adiabatic conditions as possible. In the limit of infinitely fast heating, there will be zero heat lost to the environment. In reality, some heat is lost, and that heat loss becomes worse with decreasing heating rate. This will induce inaccuracies in both the measured heat required to melt the sample, and the temperature measured by the sensor.

Fig. 4-7 shows the results of measuring the melting of a 10 nm Bi film at five heating rates from 8 kK/s to 165 kK/s, using sensors with Al metallizations. For a typical scan of room temperature to 350 °C, these heating rates translate to pulse lengths of 2 ms to 64 ms. As can be seen in the figure, the melting peaks for the slow pulses are shifted to lower temperatures, and are also broader and have a smaller integrated area. It is not immediately clear, however, whether

this effect is real and due to some physical property of the sample, or if it introduced by the sensor.

Fig. 4-8 shows the results of a similar experiment using sensors with Pt metallization. The range of heating rates is similar. The same temperature shifts visible in Fig. 4-7 are not visible here. The method of deposition is slightly different for the material in this figure. The film in Fig. 4-7 was deposited all at once, while this film was deposited in several stages, pulsing between each stage. The result is that the particles are smaller, and the average  $T_m$  is at a lower temperature. This is not the cause of the temperature shifts in Fig. 4-7, since similar behavior was noticed in several different samples with different deposition conditions.

#### 4.4.1 Finite element analysis

Why, then, is there a difference in the two results? It is interesting to note that the thermal properties of the Al and Pt used for the metallization are rather different. Al is a much better thermal conductor than Pt. The thermal diffusivity  $D$  of Al is roughly four times that of Pt, as can be seen in Table 4-I.

To determine whether some sort of temperature nonuniformity was the cause of the shifts in the temperature peaks shown in Fig. 4-7 and Fig. 4-8, the response of a sensor to a sample was simulated using a two-dimensional finite element analysis (FEA). An implicit solution method was used, and the simulation was done using MATLAB (The Mathworks, Inc.) Several simplifications were used in this analysis:

- (1) Temperature in the direction perpendicular to the surface (thickness) was assumed to be constant. The thickness of the sensor is  $\sim 100$  nm, and the thermal diffusion length ( $\sqrt{Dt}$ ) for  $\text{SiN}_x$  is  $\sim 1$   $\mu\text{m}$  in 10  $\mu\text{s}$ , so this should be a reasonable simplification.

- (2) The sample film was assumed to be of uniform thickness, evenly spread over the 400  $\mu\text{m}$ -wide sample area. In other words, the particle nature of the film was neglected.
- (3) All properties except electrical resistance were assumed to be constant with respect to temperature.
- (4) Size effects in melting were neglected, so  $T_m = T_m^{bulk}$ . Unless otherwise noted, size effects in the electrical properties of the heater metal were ignored, and bulk properties used.
- (5) The finite element mesh used in all results shown here was  $10 \mu\text{m} \times 10 \mu\text{m}$ , giving 150,000 nodes.
- (6) The boundary conditions chosen were: a uniform initial temperature of 300 K and the edges of the membrane were assumed to be constant at 300 K. This should be a reasonable assumption, since the 250  $\mu\text{m}$ -thick Si frame has a much larger heat capacity than the membrane, and should not heat significantly.
- (7) Thermal radiation and convection were neglected.
- (8) The simulation was limited to only a single sensor, so there is no  $\Delta V$  information. Heat capacity was determined by:  $C_p = P\nu^{-1}$ .

For a 5 nm Bi film, the resulting simulated heat capacity curves can be seen in Fig. 4-9 for an Al sensor and Fig. 4-10 for a Pt sensor. For the Al sensor, there is a large difference in the apparent melting peaks,  $\sim 25$  K. For the Pt sensor, the difference is only  $\sim 9$  K. Fig. 4-11 shows simulated temperature distributions for Pt and Al metallized sensors. The right-hand view in this figure shows a contour line at  $T_m^{bulk}$ .

The difference between peaks in the experimental data is 17 K for the Al sensors, and 0.7 K for the Pt sensors. There is some discrepancy between the simulated and experimental data, but the fact that the simulated curves show the same behavior as the experimental ones strongly

suggests that the shifts in peak locations in the experimental data are due to temperature nonuniformities in the sensors, and not some intrinsic material property of Bi. The simulations neglect thermal radiation, which may become significant for longer pulses, since heat loss at a given temperature will be proportional to time. Heat loss through radiation would have the effect of reducing the nonuniformities in temperature because it will be much stronger in regions of high temperature (since heat loss  $\propto T^4$ ) like at the center of the heater.

#### 4.4.2 *Very slow pulses*

As discussed above, there are significant thermal nonuniformities introduced into sensors by pulsing for long times with slow heating rates. Just how significant these are can be seen in Fig. 4-12. That figure shows the results of a simulation of an Al sensor pulsed at  $\sim 7$  kK/s. The dark line is a contour line of where the temperature has reached  $T_m^{bulk}$ . This will mark the border between Bi that was melted and Bi that never got hot enough to melt. Note that, not only is the center of the heater significantly hotter than the rest, but the melted zone is still entirely within the voltage senses. This means that  $\sim 20\%$  of the Bi never melted in this pulse. This helps explain why the slow pulses in Fig. 4-7 have a smaller integrated area than the fast pulses: the effective sample size is smaller.

#### 4.4.3 *Experimental evidence of nonuniformity*

To verify the extent of the nonuniformities found in these simulations, 10 nm Bi films were deposited on sensors with different metallizations, and the sensors pulsed using slow rates. In the as-deposited state, the Bi film is fairly uniform and continuous; it is only upon melting that it forms spheres. If the film is thick enough, the change in film morphology is visible to the eye.

The boundary between melted and unmelted material will show where the temperature reached at least  $T_m$ .

Fig. 4-13 shows optical micrographs of two sensors so treated. The silicon frame is visible at the outer edge of the image. The  $\text{SiN}_x$  membrane is transparent, and the metallization is visible through it. The heater is a horizontal strip 500  $\mu\text{m}$  wide, and the roughly-triangular voltage senses can be seen on the lower left and upper right of each sensor. The Bi is deposited in a 400  $\mu\text{m}$  wide strip aligned with the heater. Material deposited through the  $\sim 400$   $\mu\text{m}$  wide notch cut into the shadow mask (usually used for TEM observations) is also visible at the center of the heater. The sensors were pulsed at  $\sim 7$  kK/s for 64 ms to melt the 10 nm thick film. The maximum measured temperature was 310  $^\circ\text{C}$ .

The melted/unmelted boundary is visible as a dark line where the Bi film changes color. For the Al sensor in Fig. 4-13(a), the melted region is  $\sim 5$  mm long, while it is  $\sim 6$  mm long on the Pt sensor in Fig. 4-13(b). Any measurement of the melting signal from Fig. 4-13(b) is therefore expected to be 20% greater than that from Fig. 4-13(a).

#### ***4.5 Mapped Melting Temperatures***

Eight Bi films with nominal thicknesses between 0.3 nm and 10 nm were measured calorimetrically and with TEM as described in Chap. 3. For each film, the  $T_m(r)$  relationship was determined. The results for these films can be seen in Fig. 4-14. As can be seen from this figure, as the film thickness increases, the melting temperature trends toward  $T_m^{bulk}$ .

The results for these films can also be seen in Fig. 4-15, along with data reported by G. Allen [2] and Peppiatt [3]. Also shown in that figure is the  $T_m(r)$  relationship fitted by G. Allen using the HMM.

#### 4.6 References

- [1] M. Zhang, M. Y. Efremov, F. Schiettekatte, E. A. Olson, A. T. Kwan, S. L. Lai, T. Wisleder, J. E. Greene, and L. H. Allen. "Size-dependent melting point depression of nanostructures: Nanocalorimetric measurements." *Phys. Rev. B* **62**. 10548 (2000).
- [2] G. L. Allen, R. A. Bayles, W. W. Gile, and W. A. Jesser. "Small particle melting of pure metals." *Thin Solid Films* **144**. 297 (1986).
- [3] S. J. Peppiatt. "The melting of small particles. II. Bismuth." *Proc. R. Soc. London, Ser. A* **345**. 401 (1975).
- [4] D. R. Lide. *CRC Handbook of Chemistry and Physics*. vol. 82. New York: CRC Press. (2002).

4.7 Figures and Tables

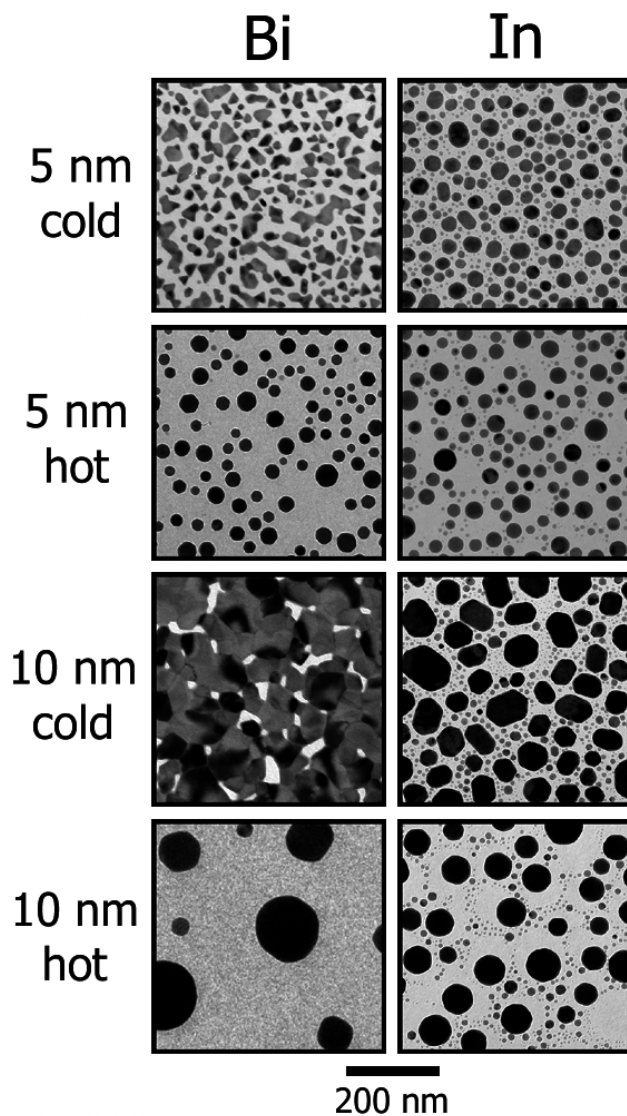


Figure 4-1: TEM micrographs for Bi and In films, 5 and 10 nm thick, heated (hot) and unheated (cold). Note how the hot films are similar at 5 nm, but the Bi particles in the 10 nm thickness are much larger than those in the corresponding In micrograph.

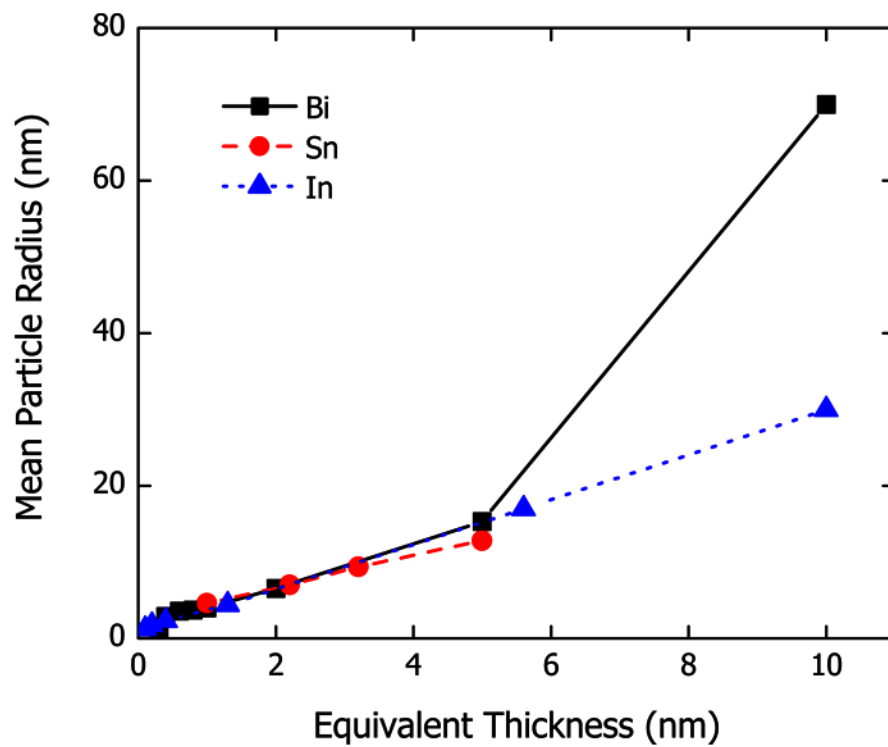


Figure 4-2: Mean particle radius vs. average film thickness. Note how the 10 nm Bi trends toward high values. Data for Sn films above 5 nm were not available.



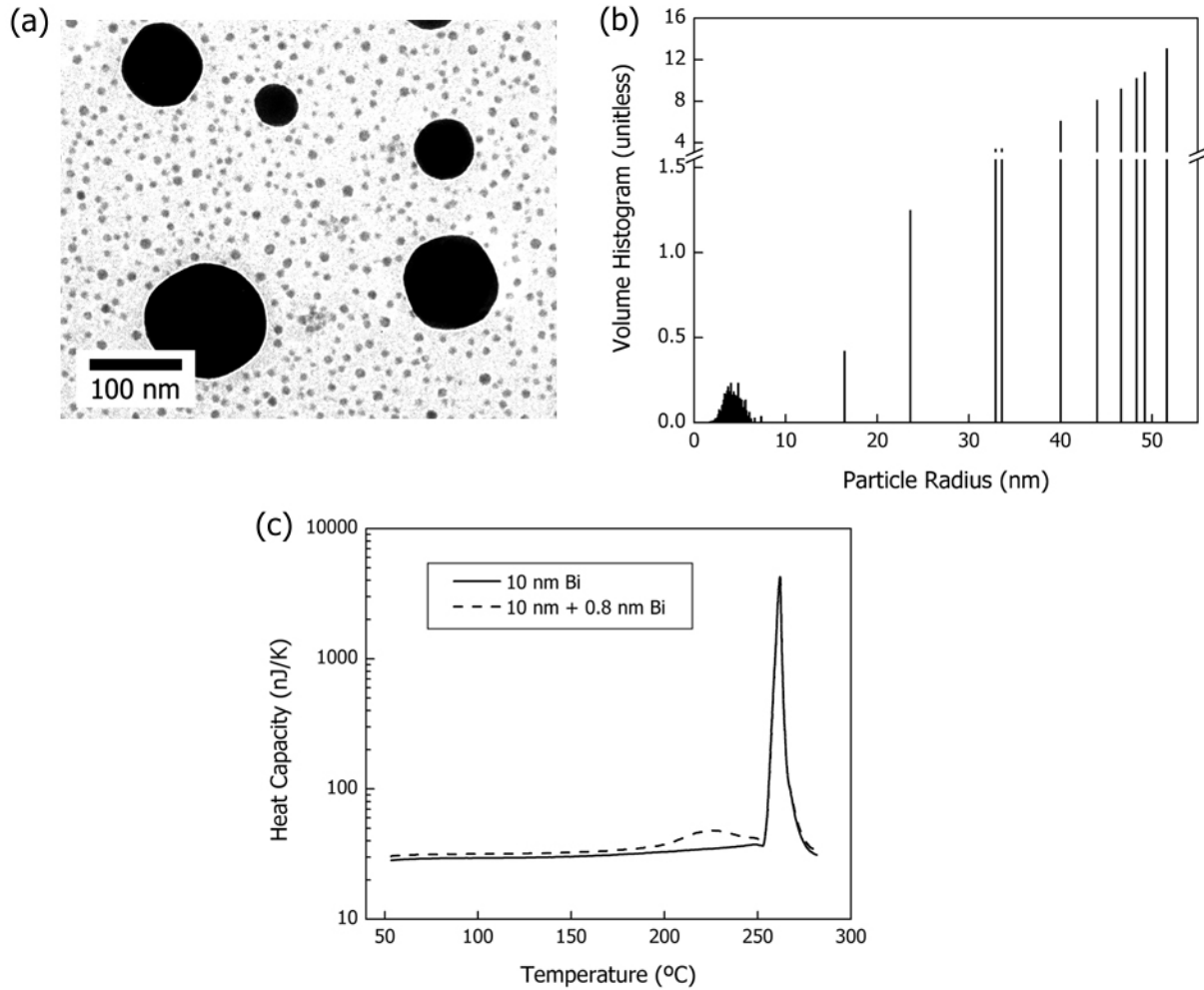


Figure 4-3: Dual deposition showing bimodal particle size distribution. A 10 nm Bi deposition was done to form large particles, then an addition 0.8 nm deposited to form small ones. (a) A portion of a TEM micrograph showing a few very large particles combined with many smaller ones. (b) The particle size histogram of the entire micrograph from (a). The small particles from the 0.8 nm deposition can be seen in the 0-10 nm region of the histogram, and the large particles above 10 nm. Note the difference in scale before and after the y-axis break. (c) Heat capacity data from the 10 nm and the 10+0.8 nm films. The smaller particles have a lower  $T_m$ , which can be seen in the small melting peak  $\sim 225$  °C.

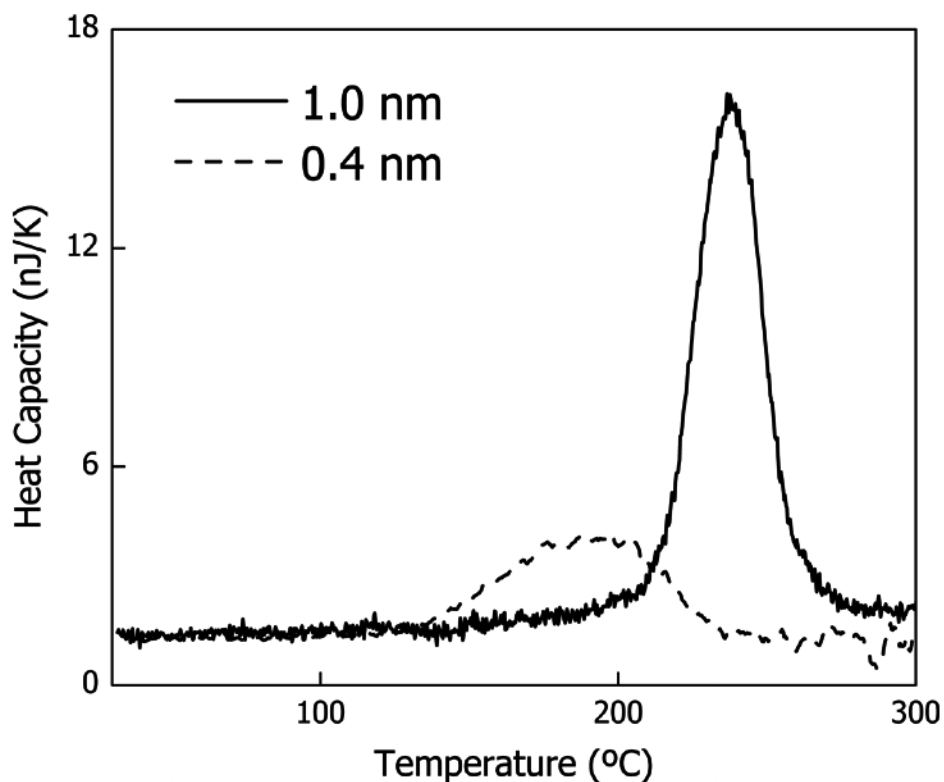


Figure 4-4: Heat capacity curves for two Bi films, 1.0 and 0.4 nm thick. The (peak) melting temperature for the 0.4 nm curve is  $\sim 25$  °C lower than that of the 1.0 nm film. This is due to the smaller average radius of particles. Similarly, the integrated area under the peak is smaller, because there is less material to melt, and, accordingly, less heat is required to melt it. The heating rates for these films was  $\sim 40$  kK/s.

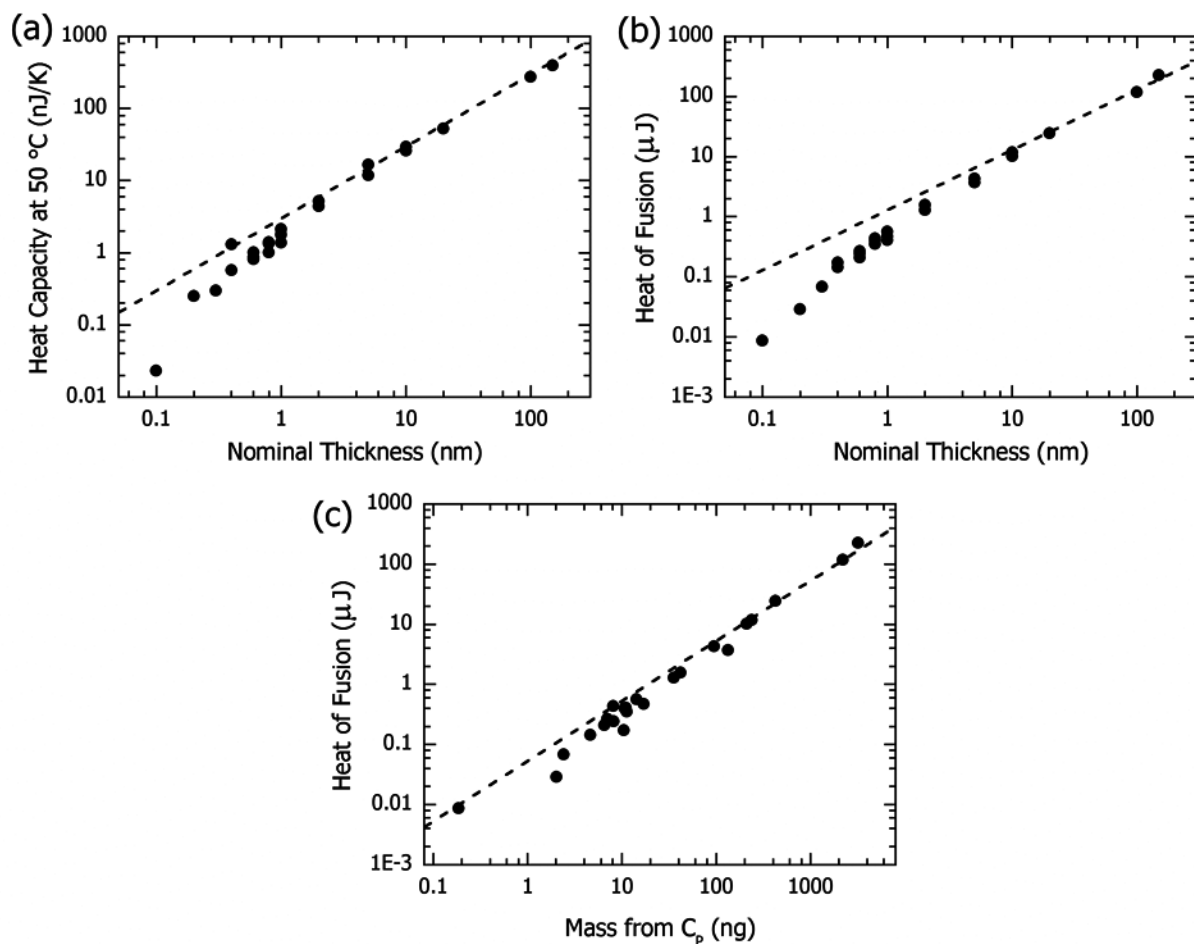


Figure 4-5: Heat capacity and heat of fusion for a series of twenty-three Bi films. (a) Heat capacity at 50 °C as a function of nominal film thickness measured by the quartz crystal thickness monitor. The dashed line represents the bulk heat capacity  $\overline{c_p}(T)$ . (b) Latent heat of fusion as a function of nominal film thickness. (c) Heat of fusion as a function of sample mass, where mass has been calculated from the measured heat capacity. In (b) and (c), the dashed line represents the bulk heat of fusion.

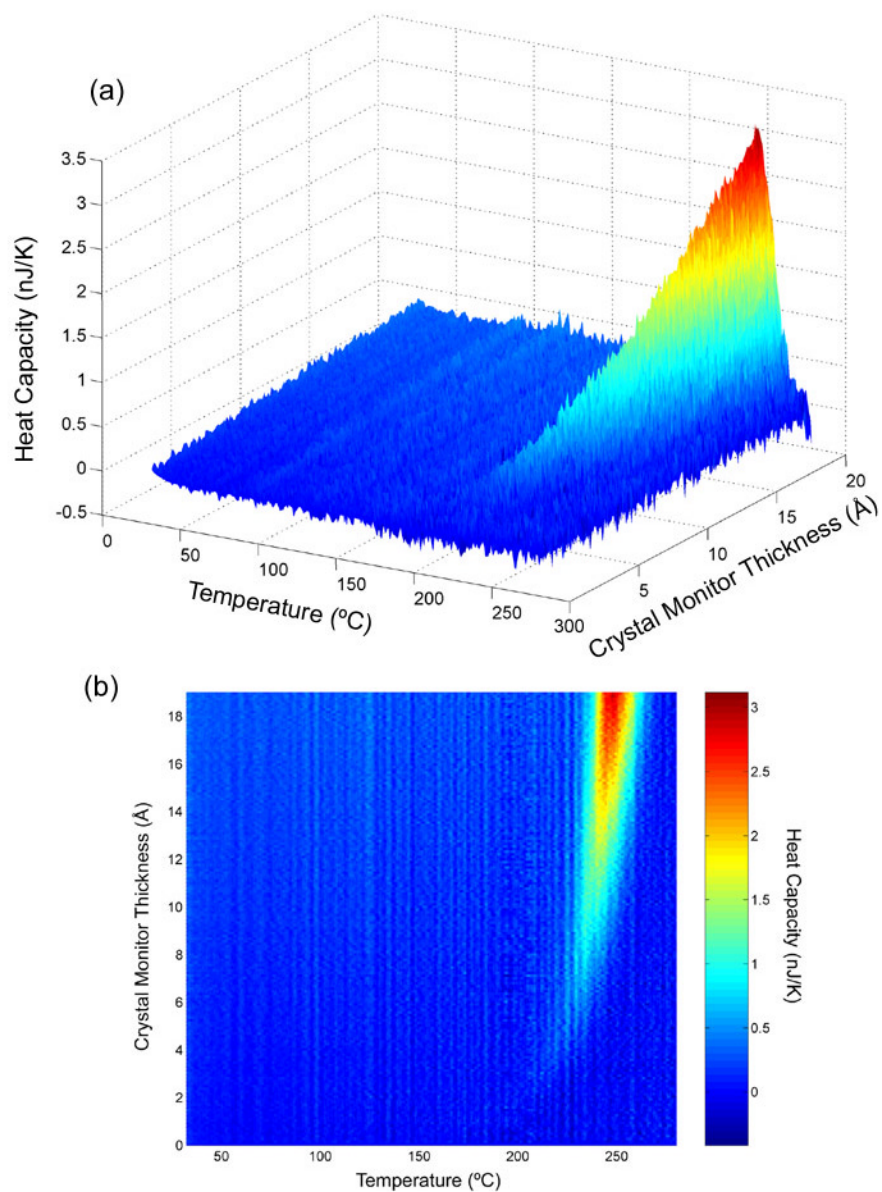


Figure 4-6: Continuous heat capacity measurement. Here, the continuous deposition of Bi onto a sensor is measured in real-time at 1 calorimetric scan/s. The total deposition onto the quartz crystal monitor used to monitor film thickness was 2 nm, but the  $C_P$  and  $H_m$  values from the calorimetric curve both suggest there was only  $\sim 0.1$  nm deposited onto the sensor.

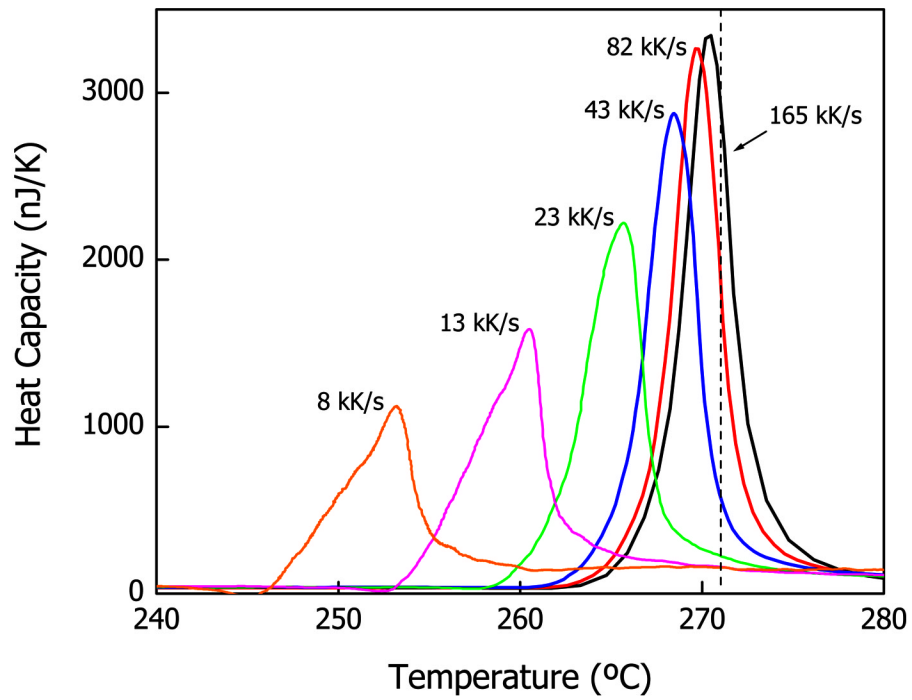


Figure 4-7: Melting of a 10 nm Bi film at six different heating rates, using sensors with Al metallizations. Only the region of the caloric curve near the melting temperature is shown.  $T_m^{bulk}$  is shown by the dashed line.

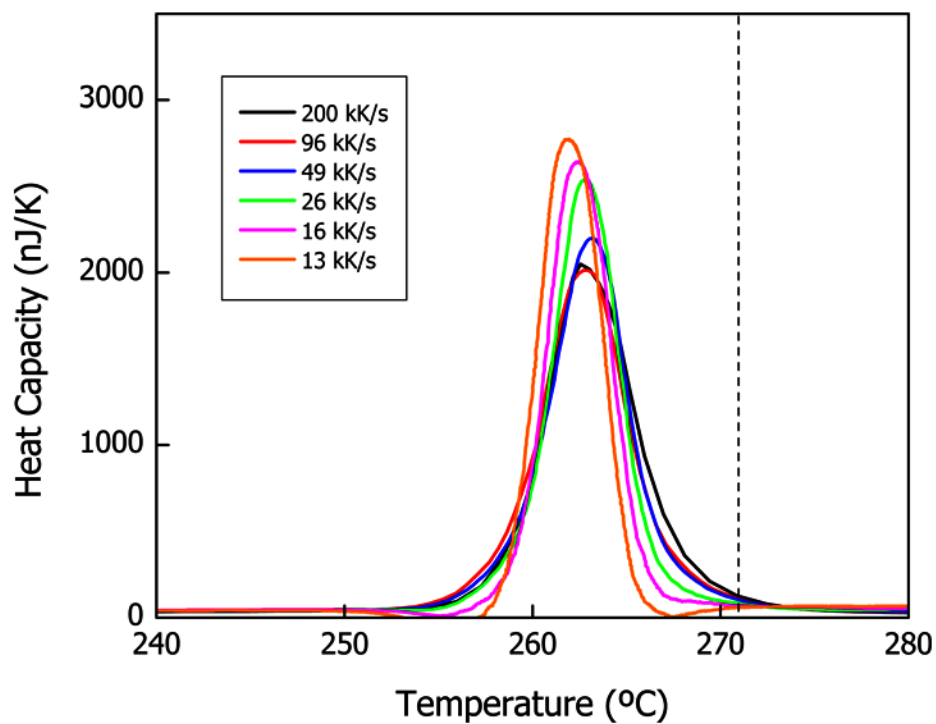


Figure 4-8: Melting of a 10 nm Bi film at six different heating rates, using sensors with Pt metallizations. Only the region of the caloric curve near the melting temperature is shown.  $T_m^{bulk}$  is shown by the dashed line. The decrease in the peak temperature suggests that the particles measured here are slightly smaller than those measured in Fig. 4-5.

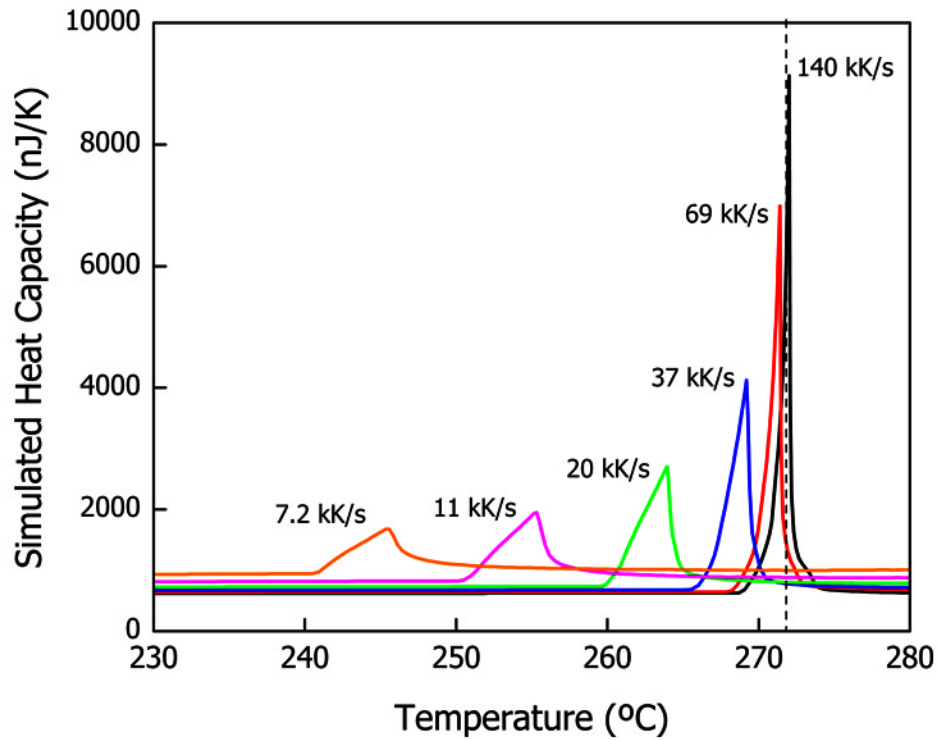


Figure 4-9: FEA simulated heat capacity of a uniform 5 nm Bi film on an Al sensor measured at six different heating rates.  $T_m^{bulk}$  is shown by the dashed line. There is ~25 K difference between the curves at 140 kK/s and 7.2 kK/s. Also, the slower curves are broader and have a smaller integrated area.

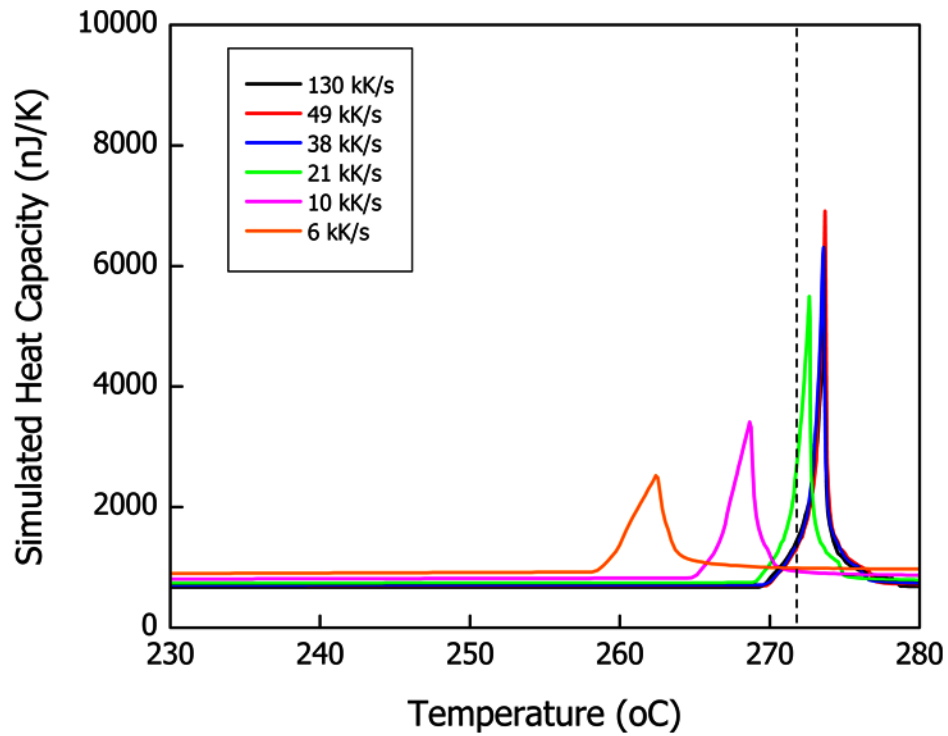


Figure 4-10: FEA simulated heat capacity of a uniform 5 nm Bi film on a Pt sensor measured at six different heating rates. The axis limits for this figure are the same as in Fig. 4-7. The difference in the location of the peaks between the fastest and slowest pulses is ~9 K.



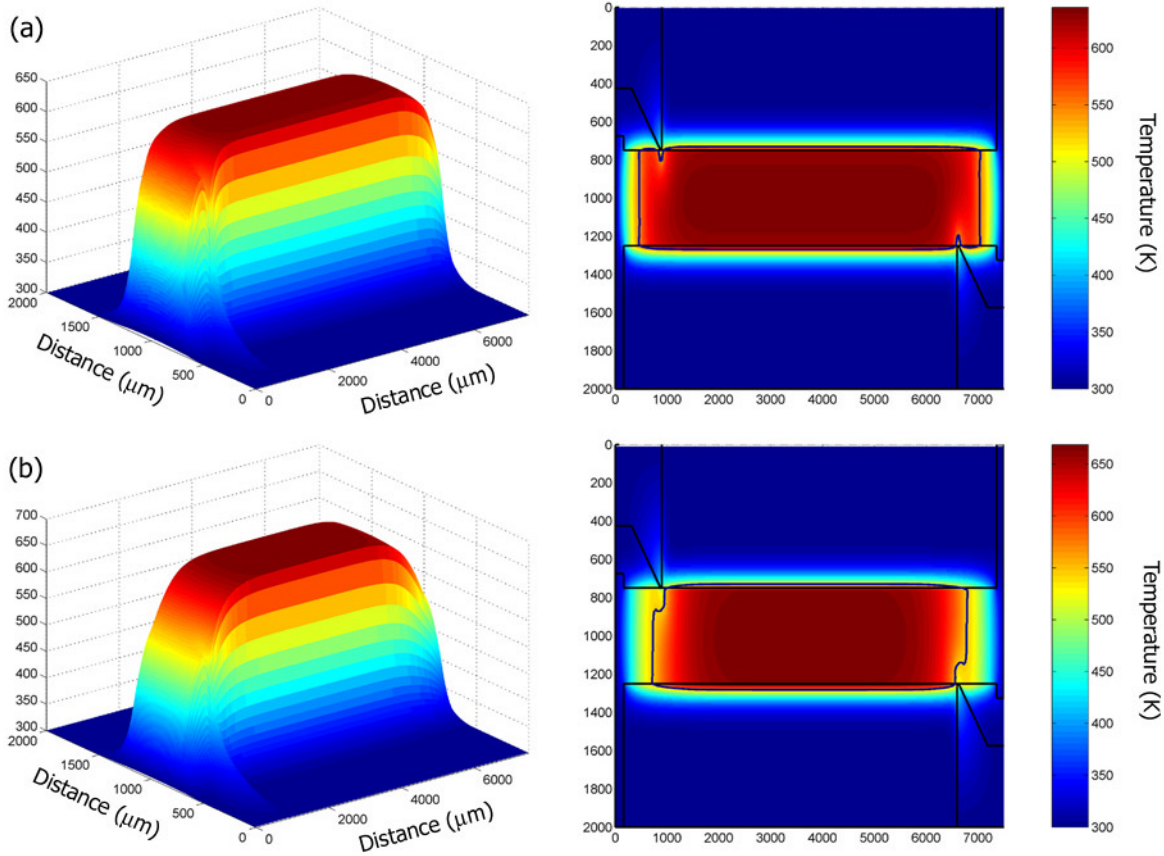


Figure 4-11: FEA simulations of a 5 nm Bi film on (a) Pt and (b) Al sensors at  $\sim 40$  kK/s. Both columns show the temperature distributions at the end of the scan; the right-hand column is an overhead view. Black lines in the right-hand column figures show the outline of the heater and voltage senses. The location of  $T_m^{bulk}$  is shown by a dark contour line. All Bi inside this line is melted; everything outside it is solid. The slight distortion at  $\sim 1000$   $\mu\text{m}$  and  $\sim 6500$   $\mu\text{m}$  is due to heat being drawn away by the triangular voltage contacts.

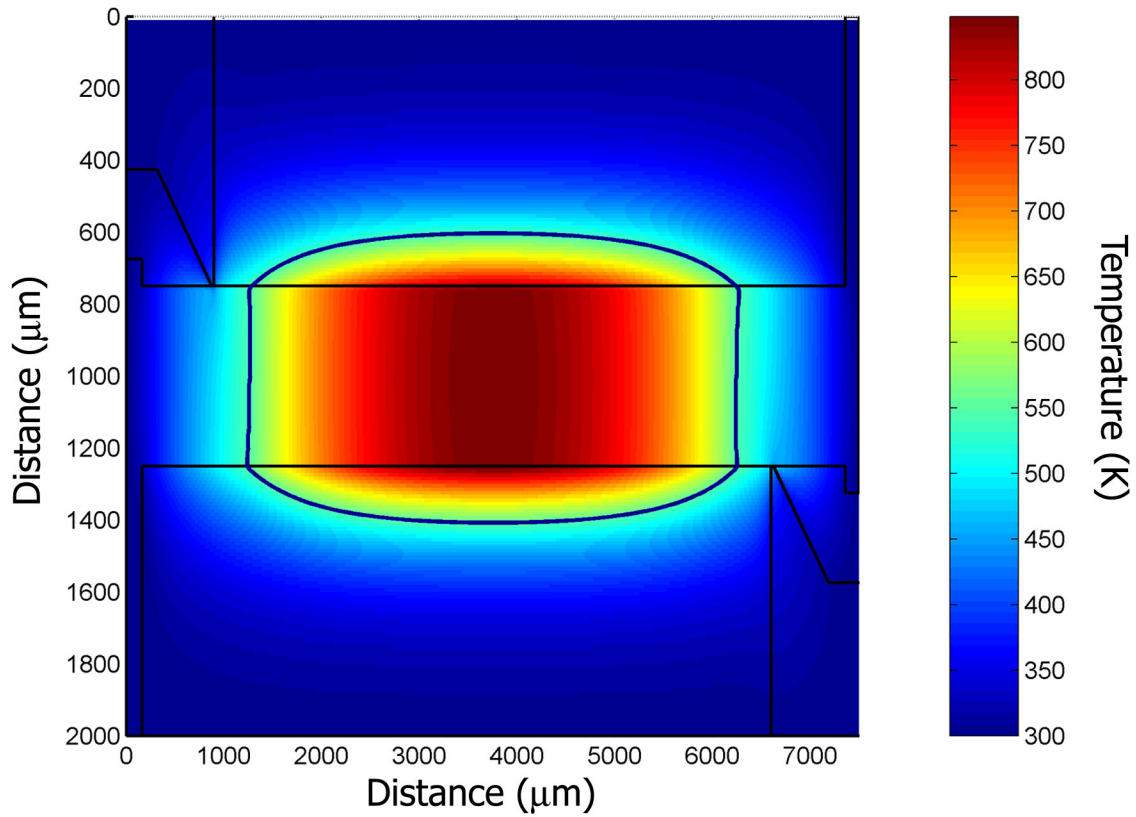


Figure 4-12: FEA simulation of a 5 nm Bi film on an Al sensor at  $\sim 7$  kK/s. Black lines show the outline of the heater and voltage senses. The location of  $T_m^{bulk}$  is shown by a dark contour line. Note the high temperature at the very center of the heater, but the melted zone does not reach out even to the voltage contacts.

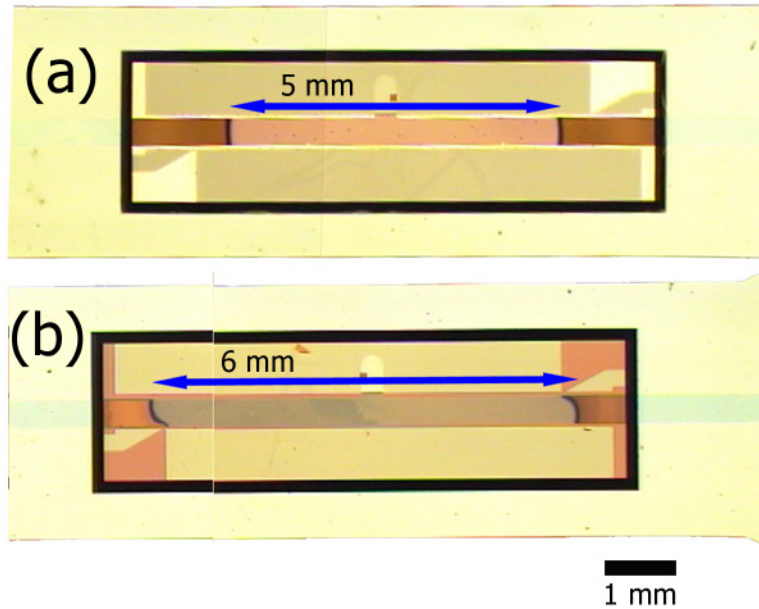


Figure 4-13: Optical micrographs of a 10 nm Bi film on (a) an Al sensor and (b) a Pt sensor. These sensors had each been heated to 310 °C at  $\sim 7$  kK/s. The Bi is limited to a 400  $\mu\text{m}$  wide stripe down the center of the heater. There is a contrast difference between melted and unmelted Bi. For the Pt sensor in (b), the melted zone extends to the edge of the voltage senses. For the Al sensor in (a), not all the material had melted, even though the measured average temperature was 40 K above  $T_m^{bulk}$ .

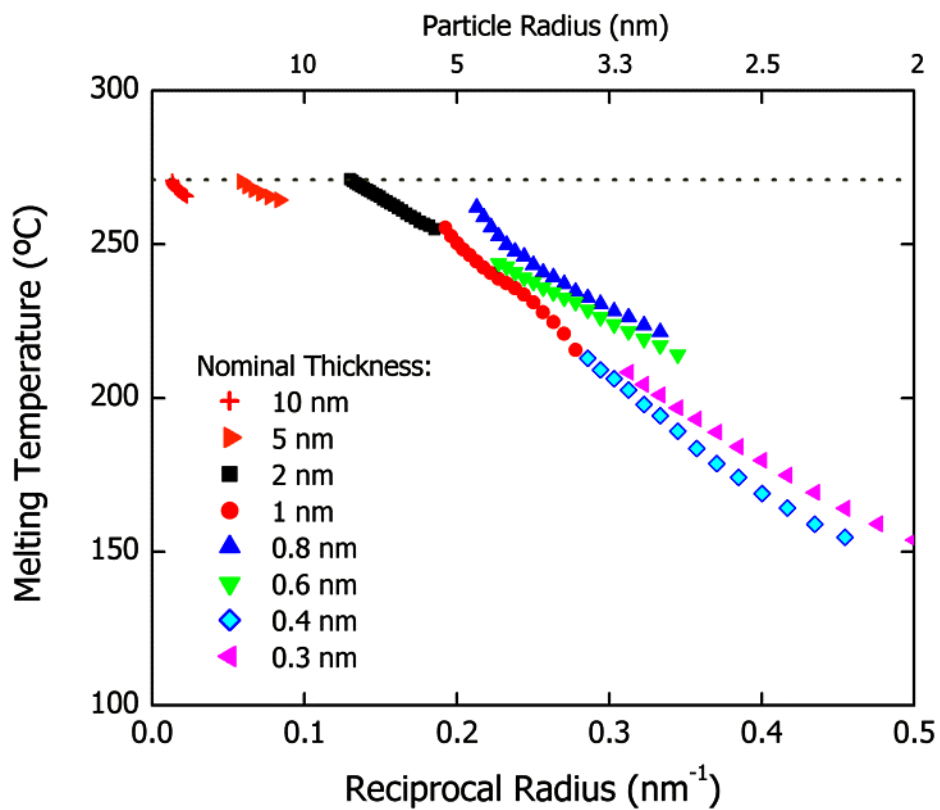


Figure 4-14: Mapped data for this work. Shown are melting temperatures as functions of particle sizes, using films 0.3 nm to 10 nm thick. The dotted line is  $T_m^{bulk}$  for Bi, 271 °C.

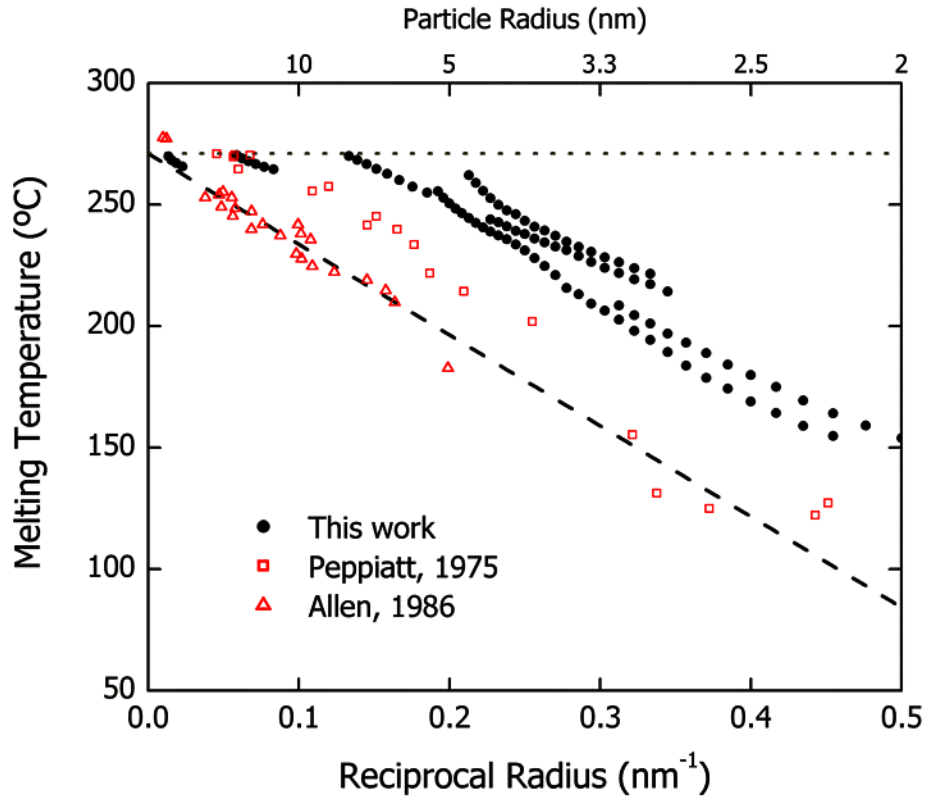


Figure 4-15: Mapped data for this work, as well as results from two other researchers. The dotted line is  $T_m^{bulk}$  for Bi, 271 °C. The dashed line represents the expected values using the HMM model and surface energies according to G. Allen. [2]

TABLE 4-I: Properties of typical heater metals at ~25 °C. [4]

	$k$ (W cm <sup>-1</sup> K <sup>-1</sup> )	$C_P$ (J g <sup>-1</sup> K <sup>-1</sup> )	$\rho$ (g cm <sup>-3</sup> )	$D$ (cm <sup>2</sup> s <sup>-1</sup> )
Al	2.37	0.904	2.7	0.971
Au	3.17	0.129	19.3	1.27
Ni	0.907	0.445	8.9	0.229
Pt	0.716	0.133	21.5	0.250

## Chapter 5: Discussion

The most unusual aspect of the work presented here is that the melting temperatures determined appear to be about 25 °C higher than those previously reported [1, 2]. As expected, the melting temperature trends toward  $T_m^{bulk}$  for thick films and large particles. Above a film thickness of  $\sim 2$  nm, there is little melting point depression. Also of interest, the melting temperature is higher than predicted by the HMM. Discussed below are some possible interpretations of this result.

### 5.1 Sensor Uniformity

It has been shown in Chapter 4 that the temperature of a calorimetric sensor is significantly nonuniform if the heating rate is low, or if the sensor metallization conducts heat well. Since measuring the resistance (and therefore the temperature) of the sensor yields only one number, this method only measures an average resistance of the entire sensor. Therefore, the measured temperature will reflect the average temperature of a non-uniform sensor, and will always have a *lower* value than the maximum temperature. Since the results shown here have a  $T_m(r)$  *higher* than expected, this is probably not the cause.

### 5.2 Temperature Calibration

What is really measured in the calorimetric experiment is the electrical resistance of the sensor, and that resistance is then transformed into temperature using a predetermined  $T(R)$  polynomial. Therefore, the temperature measurement will only be as accurate as the temperature calibration. If, for example, the metal film has had some defects introduced into it since

calibration, the measured resistance will be increase, and the observed temperature will be higher than the actual temperature.

The calibration is done in a vacuum furnace where the entire sensor is uniformly heated, including the Si frame. During a calorimetric experiment, however, just the section of the metallization on the frame heats up. There may be, for example, some stress at some area of the film due to temperature gradients or difference in thermal expansion of the materials that make up the sensor. Also, the current used during calibration to measure the resistance of the sensor is small (100  $\mu$ A), while the currents used during calorimetric pulses can be as high as 100 mA. If high current densities cause deviations from Ohm's Law in the metal, the resulting temperature will be incorrect.

The highest current used in these experiments is  $\sim$ 100 mA. For a metal film with a cross section of 500  $\mu$ m  $\times$  50 nm, this would result in a current density of  $4 \times 10^5$  A/cm<sup>2</sup>. Ohm's Law is obeyed up to at least  $5 \times 10^8$  A/cm<sup>2</sup> in Au and  $2 \times 10^8$  A/cm<sup>2</sup> in Pt [3]. Therefore, the calorimetric sensors are expected to exhibit ohmic behavior.

There are three points of internal temperature calibration. First is the starting, or room, temperature. Any significant change in the resistance of the film would be detectable as an increase in the initial resistance of the sensor, and the pulse would appear to start above room temperature. Also, thick Bi and In films can be used to determine the melting points of bulk material ( $T_m^{In} = 157$  °C and  $T_m^{Bi} = 272$  °C). If there is a problem with the calibration or current used in the pulse, these values will be incorrect.

Sensors with Au metallizations do suffer from an increase in initial resistance after extended periods of time. This may be due to grain growth of the Au film, as happens at room temperature on glass [4]. This can be compensated for by adjusting the  $T(R)$  relation so that the

temperature response is constant, but the room temperature resistance is increased to match the measured value.

### 5.3 Superheating and Kinetics

Both the above explanations consider only equipment and experimental effects for the behavior seen in Figs. 4-14 and 4-15. There remains the possibility that these effects are not due to the measurement technique, but due to an inherent material property of the sample. This could be the case if, for example, small particles were in a crystal structure different from that of a bulk crystal.

If the increased melting temperatures in Fig. 4-15 are a property of the material sample, the question remains whether the increased temperature is a *thermodynamic* property or a *kinetic* one. In other words, if the property is thermodynamic, then  $T_m(r) > T_m^{HMM}(r)$ , and a particle of a given size has a melting temperature greater than that expected by the HMM model. If the property is kinetic, then the particles are somehow forced into a metastable state by the heating rates involved, and melting is a time-dependent process. They would simply have an *apparent* melting temperature greater than  $T_m^{HMM}$ .

In Fig. 5-1, the experimental superheating above  $T_m^{bulk}$  found by G. Allen [2], Murphy [5], and Peppiatt [1] is compared to the heating rates used by each one. As can be seen in the figure, it appears the faster the heating rate, the larger the degree of superheating. The range of heating rates used in this work are also shown in the figure. In this case, the superheating shown is the approximate degree of superheating above  $T_m^{HMM}(r)$ .

If the melting temperatures discussed here are indeed the thermodynamic melting temperatures, they will be size-dependent, but not heating-rate-dependent. This is consistent with



what is seen in Fig. 4-8, where the melting peak does not shift to different temperatures at rates ranging between 13 kK/s and 200 kK/s. Based on the FEA simulations previously discussed, it seems reasonable to conclude that the shifts in melting temperature shown in Fig. 4-7 are due to temperature nonuniformities of the Al sensor, and not any material property.

Probably the best explanation for why  $T_m(r) > T_m^{HMM}$  is the possibility of alternate crystal structures. Indium, for example, undergoes a structure change from fc-tetragonal to fcc as the crystal radius decreased below  $\sim 3$  nm [6]. No abrupt change in  $T_m(r)$ , however, has been found in that size regime [7].

It is not clear whether such a structure change exists for Bi. Different researchers have produced inconclusive and possibly contradictory results [6, 8-10]. Similarly inconclusive is whether there is a contraction in the lattice parameter for small particles [11, 12]. High resolution TEM, however, on Bi particles  $\sim 4$  nm in size did not show any significant deviation from the bulk rhombohedral structure [13].

If the melting temperatures shown here are due to kinetic reasons, then it is curious that the melting peaks in Fig. 4-8 *do not* shift with heating rate. As  $v \rightarrow 0$ , melting should approach the thermodynamic limit and  $T_m(r) \rightarrow T_m^{HMM}(r)$ , and as  $v \rightarrow \infty$ ,  $T_m(r) \rightarrow \infty$ . (This neglects any upper limit to superheating.) One possible explanation for why this is not observed is that, although the heating rates are large, the range of heating rates is not large enough to demonstrate this effect. As can be seen in Fig. 5-1, the rates used here are  $\sim 10^4 \times$  higher than those used in TEM heating and traditional DSC, and  $\sim 10^5 \times$  lower than those induced by laser pulsing. It may be that rate-induced shifts could be observed if the heating rate could be arbitrarily high or low.

Blocked or forbidden surface melting could lead to such kinetic effects. Since it would be energetically unfavorable for a liquid layer to form on the surface of the particle, there would be

an activation energy required for melting. This could cause particles above  $T_m(r)$  to remain in their solid state for some time before melting. Since the average temperature of the calorimeter is monotonically rising, any time delay in melting would also be interpreted as a temperature increase. This sort of behavior is expected in Bi (see Sec. 2.4). Further supporting this idea is that a quasi-liquid layer on micron-sized Bi particles near  $T_m$  was not observed [14].

#### 5.4 Conclusions

Based on the work presented herein, it is reasonable to conclude the following:

- (1) As previously reported, and as expected, the melting temperatures of Bi nanoparticles are size dependent and a function of inverse particle radius.
- (2) Heating-rate-dependent melting peak shifts seen in calorimetric experiments made with Al sensors are due to thermal nonuniformities in the sensor itself.
- (3) At least with the heating rates available to this technique, the melting temperature of Bi nanoparticles is not rate-dependent, and is higher than predicted using the homogeneous melting model.

#### 5.5 References

- [1] S. J. Peppiatt. "The melting of small particles. II. Bismuth." *Proc. R. Soc. London, Ser. A* **345**. 401 (1975).
- [2] G. L. Allen, R. A. Bayles, W. W. Gile, and W. A. Jesser. "Small particle melting of pure metals." *Thin Solid Films* **144**. 297 (1986).
- [3] H. Heinrich and W. Jantsch. "Verification of Ohm's law up to current densities of  $10^9$  A/cm<sup>2</sup> by sub-nanosecond pulse measurements." *Solid State Commun.* **7**. 377 (1969).
- [4] C. C. Wong, H. I. Smith, and C. V. Thompson. "Surface-energy-driven secondary grain growth in thin Au films." *Appl. Phys. Lett.* **48**. 335 (1986).
- [5] E. A. Murphy, H. E. Elsayed-Ali, and J. W. Herman. "Superheating of Bi(0001)." *Phys. Rev. B* **48**. 4921 (1993).

- [6] A. Yokozeki and G. D. Stein. "A metal cluster generator for gas-phase electron diffraction and its application to bismuth, lead, and indium: Variation in microcrystal structure with size." *J. Appl. Phys.* **49**. 2224 (1978).
- [7] M. Zhang, M. Y. Efremov, F. Schiettekatte, E. A. Olson, A. T. Kwan, S. L. Lai, T. Wisleder, J. E. Greene, and L. H. Allen. "Size-dependent melting point depression of nanostructures: Nanocalorimetric measurements." *Phys. Rev. B* **62**. 10548 (2000).
- [8] V. I. Merkulov and J. S. Lannin. "Variations in atomic structure of liquid bismuth clusters." *Phys. Rev. B* **58**. 7373 (1998).
- [9] M. G. Mitch, S. J. Chase, J. Fortner, R. Q. Yu, and J. S. Lannin. "Phase transition in ultrathin Bi films." *Phys. Rev. Lett.* **67**. 875 (1991).
- [10] Y. Oshima, K. Takayanagi, and H. Hirayama. "Structural anomaly of fine bismuth particles observed by ultra high-vacuum TEM." *Z. Phys. D* **40**. 534 (1997).
- [11] X. F. Yu, X. Liu, K. Zhang, and Z. Q. Hu. "The lattice contraction of nanometre-sized Sn and Bi particles produced by an electrohydrodynamic technique." *J. Phys. Condens. Matter* **11**. 937 (1999).
- [12] F. Komnik Yu, V. V. Pilipenko, and L. A. Yatsuk. "Changes in lattice spacings in bismuth and zinc island films." *Thin Solid Films* **52**. 313 (1978).
- [13] J. G. Wen, unpublished data. (2003).
- [14] A. Pavlovska, D. Dobrev, and E. Bauer. "Surface melting versus surface non-melting: an equilibrium shape study." *Surf. Sci.* **286**. 176 (1993).

## 5.6 Figures

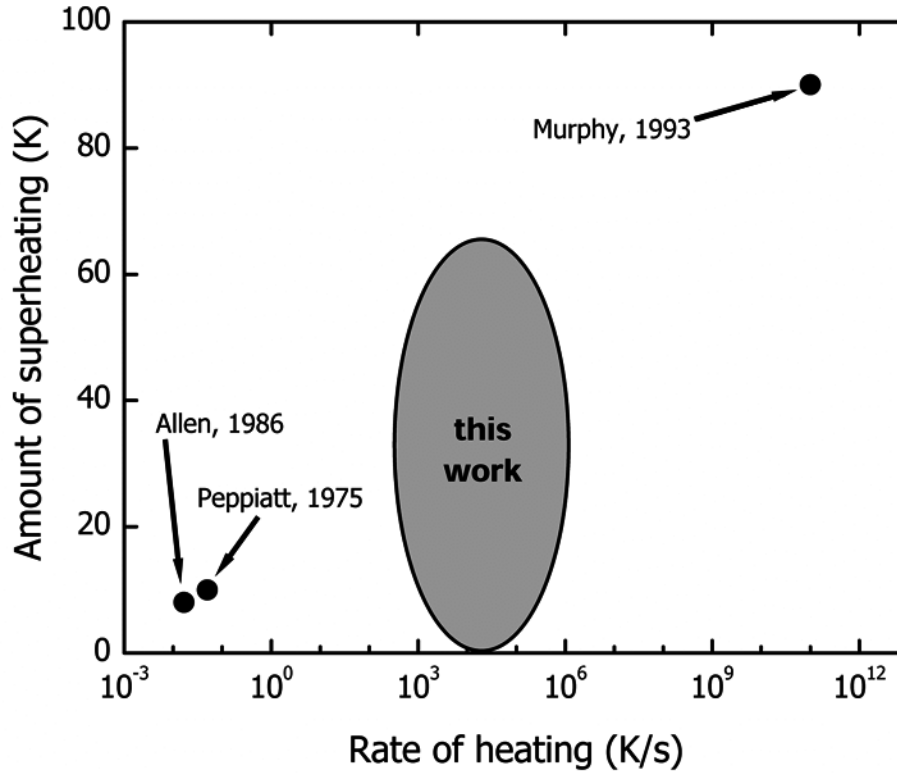


Figure 5-1: Amounts of observed Bi superheating compared with the experimental heating rates used to observe them. It should be noted that G. Allen's, Peppiatt's and Murphy's work refers to superheating above  $T_m^{bulk}$ , while this work refers to superheating above the expected, size-depressed melting temperature  $T_m^{HMM}(r)$ . Murphy's work was on a single crystal of Bi, not small particles.

## Chapter 6: Future Work

It would be advantageous if the finite element simulations described in Chap. 4 could be accurately applied to low heating rate, long time, calorimetric pulses. This would allow for more accurate simulations of the long pulses, as well as help design a calorimetric cell specifically for the purpose of doing them experimentally. Probably the greatest limitation to the FEA simulation as it stands now, is that it does not take radiation into effect. Heat loss through radiation at a given temperature will be proportional to time, and will be much more important at slow heating rates. This could be incorporated into the FEA simulations by giving each node an additional heat loss term. It would be necessary to assume some net emissivity for a given sensor metallization. Changes in emissivity with respect to temperature or due to thick samples may also need to be taken into account.

Whether Bi undergoes a phase change or if even the lattice spacing of each plane remains the same as in bulk material is still in question. The nanocalorimetric technique, obviously, can shed no light on this topic, as it does not measure the physical arrangements of the atoms. Another method, such as TEM or some sort of diffraction, must be used to determine the atomic structure of small clusters. Fortunately, any such rearrangement of atoms may not affect the calorimetry, as appears to be the case with In.

One of the limitations of the current technique is that slow heating rates can introduce significant temperature nonuniformity to a sensor. This prevents very slow pulses from being feasible, and limits the sensor to heating rates significantly faster than those used in traditional DSC. The nonuniformity is introduced because the temperature of the active area of the sensor must be  $\sim 250$  °C higher than that of the Si frame (in the case of Bi melting). If the ambient temperature could be increased, each calorimetric scan would be over a smaller range of

temperature, and temperature nonuniformities would be smaller. This could make long, slow pulses much more feasible.

This would also give some insight into the thermodynamic/kinetic nature of the particle melting. Consider a sensor with its ambient temperature raised to above  $T_m^{HMM}$ , but below the previously measured  $T_m(r)$ , and permitted to “soak” at that temperature for a long time. When the sensor is then pulsed, if the melting peak remains, this would suggest that there is no kinetic element to the melting. If the melting peak is no longer visible, this would suggest that there is some  $T_m$  above which thermodynamic stability is not retained, but kinetic limitations prevent melting.

The current experimental apparatus, however, does not permit this ambient heating. If a heating element could be introduced into the box that surrounds the sensors, the ambient temperature could be increased. It may be necessary to include some sort of heated shutter as well, to reduce radiative heat loss if the sensor has a line-of-sight to the 300 K vacuum chamber walls.

One of the most exciting potential frontiers for the nanocalorimetric technique is in protein research. Since the calorimeter design can be slightly modified to work with macroscopic liquid samples [1], it may be possible to measure the heat involved in the folding of a protein or the binding energy of a protein and substrate. If so, this could lead to the development of arrays of calorimeters for combinatorial analyses. This would allow the screening of vast expression libraries for proteins with altered functions. See Appendices A and B for more details on using the calorimetric sensor with liquids and protein studies.

## 6.1 References

- [1] E. A. Olson, M. Y. Efremov, A. T. Kwan, S. Lai, V. Petrova, F. Schiettekatte, J. T. Warren, M. Zhang, and L. H. Allen. “Scanning calorimeter for nanoliter-scale liquid samples.” *Appl. Phys. Lett.* **77**. 2671 (2000).

## Appendix A: Scanning Calorimeter for Nanoliter Scale Liquid Samples

(reprinted from *Applied Physics Letters* 77, 2671 (2000).)

E. A. Olson, M. Yu. Efremov, A. T. Kwan, S. Lai,<sup>a)</sup> V. Petrova, F. Schiettekatte, J. T. Warren,  
M. Zhang, and L. H. Allen<sup>b)</sup>

Materials Science and Engineering, University of Illinois at Urbana-Champaign, Urbana, Illinois,  
61801

Coordinated Science Laboratory, University of Illinois at Urbana-Champaign, Urbana, Illinois  
61801

We introduce a scanning calorimeter for use with a single solid or liquid sample with a volume down to a few nanoliters. We have demonstrated its use with the melting of 52 nL of indium, over a wide range of heating rates (100-1000 K/s) and found the heat of fusion to be within 5% of the bulk value. We also measured the heat of vaporization of water to be within  $\pm 23\%$  over a range of volumes from 2 to 100 nL by actively vaporizing water droplets in the scanning calorimetric mode. Excellent results (within 25%) were also obtained for the heat of vaporization by using the calorimeter in a heat-conductive mode and measuring the passive evaporation of water. The calorimeter can reach a sensitivity of  $\pm 3 \mu\text{W}$ .

**keywords MEMS, flip-chip, calorimetry, nanocalorimetry**

---

<sup>a)</sup> P29045@fpd.mot.com

<sup>b)</sup> To whom correspondence should be addressed. L-ALLEN9@uiuc.edu



Calorimetry is a universal technique for studying the thermodynamic properties and kinetic processes of materials and biological systems [1]. It is especially useful for energetic studies of exothermic and endothermic reactions and phase transformations. The conventional differential scanning calorimeter (DSC) is a well-established analytic tool, but is limited to a macroscopic sample no smaller than a fraction of a milliliter [2, 3]. Macroscale DSC can be used on small scale systems by increasing the sample size or by studying a population [4-6], but conventional methods do not work well for sample sizes on the order of nanoliters. AC microcalorimeters have been designed for samples as small as 1  $\mu\text{L}$  [7, 8], but this technique is not generally used for energetics studies [9].

Calorimetry has great potential in both pure and applied science for the investigation of material on the nanoliter scale. For example, it might be possible to nonintrusively study basic biological processes on the scale of individual cells. In the microelectronics industry, it would also be possible to study individual flip-chip solder bumps. In addition, with the use of MEMS technology, an array of calorimeters could be designed on a single wafer for rapid analysis of materials for combinatorial studies of nanoliter sized samples.

Advances have been made in the development of calorimeters in the analysis of ultra-thin films. These new nanojoule calorimeters have been used to study the melting phenomenon of nanometer sized metal particles [10], thin-films [11], and individual superconductor crystals [12, 13]. Recent developments in membrane materials [14] may lead to improvements in nanocalorimeter design and construction, and even better sensitivity. For nanoliter bulk samples, however, and especially for liquid samples, little progress has been made in the development of calorimeters for energetic studies.

In this Letter we report a new calorimetric technique for the study of a single solid or liquid sample with a volume in the nanoliter range. We demonstrate the new technique by examining simple liquid-solid and liquid-vapor transformations at very small scales and near room temperature. Ultimately, we intend to use this calorimeter in the study of polymer single crystals, biological macromolecules and the energy uptake of individual or small clusters of cells.

The calorimeters described in this work were fabricated similarly to those we have previously reported [10]. A silicon nitride membrane, 0.3  $\mu\text{m}$  thick, held by a silicon frame is constructed by etching a silicon nitride coated silicon wafer in aqueous potassium hydroxide. As a container for liquid samples, a small “box” remains unetched and has a volume of  $\sim 35$  nL. On the opposite face of the membrane, a 50 nm nickel strip is patterned and deposited, using 3 nm of titanium as an adhesion layer. A cross section of the device as well as an electron micrograph of the box is shown in Fig. 1.

Calorimetric measurements are taken by resistively heating the calorimeter by applying a dc voltage across the nickel strip. The current through the heater, as well as its resistance, is measured in real time. The temperature of the calorimeter is determined from the electrical resistance of the nickel strip.

The heat capacity of the calorimeter is then determined using:

$$C_P = \frac{dQ}{dT} = \frac{P(t)}{dT/dt} \quad (1)$$

where  $Q$  is the amount of heat absorbed;  $T$  the temperature; and  $P$  the power dissipated in the heater strip as a function of time. Latent heats are calculated by integrating the power dissipated by the heater from the beginning to end of a transformation. Corrections for heat lost to the environment are made where necessary. Additionally, the calorimeter is used as a microbalance

by measuring the difference between the heat capacity of the calorimeter with and without a sample at 30 °C.

We evaluate the performance of the calorimeter in the scanning mode by measuring the melting and vaporization of standard materials. We measure the heat of fusion and melting point of indium at heating rates from 100 to 1100 K/s, and the heat of vaporization of individual droplets of water of various volumes. To evaluate the calorimeter in a heat-conductive mode, we measure the vaporization energy of single droplets of water without active heating.

The first sample used in this work was a small section of indium wire (Alfa Aesar, 99.9985%), and was transferred into the box of the calorimeter with a glass pipette drawn to a fine, flexible end. Indium exhibits bulk characteristics at this size, unlike the size-dependent properties of the In nanostructures we recently observed [15]. Figure 2 shows heat capacity measurements of a 52 nL indium sample, scanned at a heating rate of 150 K/s. The curve shown in Fig. 2 is an average of 6 calorimetric scans. As determined by the midpoint of the peak, the melting point  $T_m$  was 155 °C and compares well with the bulk value [16]  $T_m=156.6$  °C. The precision of the technique is high; the standard deviation of  $T_m$  was less than 0.1 K for these six measurements and the FWHM of the melting peak is less than 1.3 K. The power sensitivity of this measurement was  $\pm 7$   $\mu$ W.

The size of the indium sample is comparable to solder bumps (dia.=200  $\mu$ m) used in flip-chip microelectronic interconnects. Two independent methods were used to obtain the mass of the sample: a change in the heat capacity baseline; and a conventional analytical microbalance. Since the mass of the sample is comparable to the mass of the calorimeter, there is a large (~30%) increase in the total heat capacity of the system after transferring the indium sample to the calorimeter, as can be seen in the inset of Fig. 2. Assuming the bulk value of specific heat for

indium, 0.23 J/g-K at 30 °C [17], we obtain a value of 390  $\mu\text{g}$  for the mass of the In sample using the  $C_p$  baseline method, which compares well with the 373  $\mu\text{g}$  value obtained from the microbalance (Mettler Toledo UMT2).

The latent heat of melting was calculated by integrating the area under the heat capacity peak. In this case, the total heat involved was 11 mJ. Using the previously determined mass, we obtain a value of 27.2 J/g for the latent heat of fusion  $H_m$ , which compares well with the bulk value [16] of 28.6 J/g. We obtained consistent values for  $H_m$  ( $\pm 6\%$ ) over a wide range of heating rates, from 100 to 1100 K/s. Corrections were made to account for the heat lost to the ambient at the slower heating rates.

Since most biological studies involve aqueous solutions, we are especially interested in studies of liquids between 20 and 100 °C. To evaluate the use of this new calorimetric device for liquid samples we measure the vaporization of single, nanoliter-sized water droplets using the calorimeter in both scanning and heat-conductive modes. In order to obtain a quantitative value for the volume of water for each droplet used for this paper, we place the droplet on the heater side of the device. We do this so that we obtain an unobstructed view of the droplet for size measurements using an optical microscope without the interference of the Si box.

In Fig 3 we show the results of a vaporization study of water droplets heated at  $\sim 100$  K/s. Each water droplet was placed on the calorimeter using a syringe coupled to a capillary tube drawn to a  $\sim 100$   $\mu\text{m}$  point. In future designs, microfluidic channels [18, 19] may be incorporated into the device as a sample delivery system. The size of the droplet is determined immediately prior to heating by measuring the diameter of the droplet using a conventional 40x optical microscope. The height-to-diameter ratio for water on silicon nitride was previously determined by simultaneously measuring the height and diameter of a series of drops using the microscope

and a 3 mm × 3 mm, 45°, Al<sub>2</sub>O<sub>3</sub> mirror. Using the measured diameter of the droplet and the height-to-diameter ratio, the volume of the (truncated sphere) droplet is then calculated.

The inset for Fig. 3 shows the  $C_p$  vs. T curves for 2, 3 and 7 nL water droplets. Note the increased heat required for vaporization as the size of the droplet increases. Shown in the main figure is the heat of vaporization  $H_v$  (area under the peak) for variously sized droplets ranging from 2 to 100 nL. Excellent agreement is obtained for the average value of  $H_v$ ,  $2250 \pm 500$  J/g (solid line), as compared with the bulk value for water [16]  $H_v = 2260$  J/g at 100 °C.

The final investigation presented in this paper demonstrates the new device operated in the heat-conductive mode, which is especially useful in the study of biological processes occurring near room temperature. For this experiment, we transfer a small (~60 nL) droplet of water to the calorimeter, then monitor the temperature of the system as the droplet evaporates. In this mode, the current used to measure the resistance/temperature of the calorimeter is extremely small, so that the resultant Joule heating is negligible. A typical result is shown in Fig. 4. As the droplet evaporates, heat is consumed, which cools ( $\Delta T \approx 5$ K) the calorimeter in proportion to the rate of evaporation. As the size of the droplet decreases, the evaporation rate and cooling rate also decrease, until finally ( $t=240$  s) the temperature of the calorimeter reaches the original ambient conditions.

The value of  $H_v$  for the droplet is determined by heating the bare sensor the same amount that the evaporation of the droplet had cooled it. The heat consumed during evaporation is found to be within 25% of the expected amount. Using the heat-conductive mode of the calorimeter, we find the sensitivity of the system can be as high as  $\pm 13$  mK or  $\pm 3$   $\mu$ W. Further improvement of the technique can be gained by using an additional reference calorimeter and measuring the difference in temperature. In this case, the temperature sensitivity is increased to

$\pm 3$  mK when measured over 36 000 s (10 hr). This would correspond to a power sensitivity of  $\pm 0.7$   $\mu$ W. Additional substantial gains in sensitivity can also be realized by developing a true differential calorimetric system [20].

The calorimeter described in this paper can also be used in an enclosed configuration where the entire sensor or just the sample cavity is sealed to prevent undesired evaporation of material during the calorimetric measurements. In preliminary enclosure designs, a single water droplet was stable in size for approximately an hour.

In summary, we have developed a calorimeter that allows us to study systems at sample sizes much smaller than normally accessible to a calorimeter. Intended for use with either liquid or solid samples, this calorimeter is able to measure the latent heat of transformations or simply act as a temperature sensor. We have demonstrated its use with the melting of indium, by actively vaporizing water droplets, and by passively monitoring temperature during the evaporation of water. The calorimeter can reach sensitivity up to  $\pm 13$  mK and  $\pm 3$   $\mu$ W in a heat-conductive mode and  $\pm 0.1$  K and  $\pm 7$   $\mu$ W in scanning mode. By measuring two calorimeters, the temperature sensitivity in the heat-conductive mode can be increased to  $\pm 3$  mK.

We gratefully acknowledge all the staff, especially Phil Infante, at the Cornell Nanofabrication Facility for their help in fabricating the calorimeters. This work was funded under NSF grant SGER DMR 9807384 and microanalysis was performed at the MRL at UIUC. A. Kwan was partially funded under ACS-PRF #33580-AC7. L. Allen is supported by NSF DMR 9726458.

## A.1 References

- [1] P. Duboc, L. G. Cascão-Pereira, and U. von Stockar. *Biotech. and Bioeng.* **57**. 610 (1998).
- [2] M. J. M. Van Oort and M. A. White. “Automated, small sample-size adiabatic calorimeter.” *Rev. Sci. Instrum.* **58**. 1239 (1987).
- [3] V. K. Pecharsky, J. O. Moorman, and K. A. Gschneidner, Jr. “A 3-350 K fast automatic small sample calorimeter.” *Rev. Sci. Instrum.* **68**. 4196 (1997).
- [4] A. Bogdan, M. Kulmala, and N. Avramenko. “Reduction of enthalpy of fusion and anomalies during phase transitions in finely divided water.” *Phys. Rev. Lett.* **81**. 1042 (1998).
- [5] K. M. Unruh, T. E. Huber, and C. A. Huber. “Melting and freezing behavior of indium metal in porous glasses.” *Phys. Rev. B* **48**. 9021 (1993).
- [6] C. Faivre, D. Bellet, and G. Dolino. “Phase transitions of fluids confined in porous silicon: a differential calorimetry investigation.” *European Physical Journal B* **7**. 19 (1999).
- [7] H. Yao, K. Ema, and I. Hatta. “High-resolution AC calorimeter for measuring the heat capacity of small amounts of liquid samples.” *Jpn. J. Appl. Phys., Part 1* **38**. 945 (1999).
- [8] J. E. Smaardyk and J. M. Mochel. *Rev. Sci. Instrum.* **49**. 988 (1978).
- [9] J. Caerels, C. Glorieux, and J. Thoen. “Absolute values of specific heat capacity and thermal conductivity of liquids from different modes of operation of a simple photopyroelectric setup.” *Rev. Sci. Instrum.* **69**. 2452 (1998).
- [10] S. L. Lai, J. Y. Guo, V. Petrova, G. Ramanath, and L. H. Allen. “Size-dependent melting properties of small tin particles: nanocalorimetric measurements.” *Phys. Rev. Lett.* **77**. 99 (1996).
- [11] D. W. Denlinger, E. N. Abarra, K. Allen, P. W. Rooney, M. T. Messer, S. K. Watson, and F. Hellman. “Thin film microcalorimeter for heat capacity measurements from 1.5 to 800 K.” *Rev. Sci. Instrum.* **65**. 946 (1994).
- [12] F. Fominaya, T. Fournier, P. Gandit, and J. Chaussy. “Nanocalorimeter for high resolution measurements of low temperature heat capacities of thin films and single crystals.” *Rev. Sci. Instrum.* **68**. 4191 (1997).
- [13] O. Riou, P. Gandit, M. Charalambous, and J. Chaussy. “A very sensitive microcalorimetry technique for measuring specific heat of  $\mu\text{g}$  single crystals and application to YBCO.” *Rev. Sci. Instrum.* **68**. 1501 (1997).

- [14] T. A. Friedmann, J. P. Sullivan, J. A. Knapp, D. R. Tallant, and D. M. Follstaedt. *Appl. Phys. Lett.* **71**. 3920 (1997).
- [15] M. Y. Efremov, F. Schiettekatte, M. Zhang, E. A. Olson, A. T. Kwan, R. S. Berry, and L. H. Allen. “Discrete periodic melting point observations for nanostructure ensembles.” *Phys. Rev. Lett.* **85**. 3560 (2000).
- [16] D. R. Lide. *CRC Handbook of Chemistry and Physics*. 80 ed. New York: CRC Press. (1999).
- [17] R. Hultgren, P. D. Desai, D. T. Hawkins, M. Gleiser, K. K. Kelley, and D. D. Wagman. *Selected Values of the Thermodynamic Properties of the Elements*. Metals Park, Ohio: American Society for Metals. (1973).
- [18] B.-H. V. L. Jo, L.M.; Motsegood, K.M.; Beebe, D.J. “Three-dimensional micro-channel fabrication in polydimethylsiloxane (PDMS) elastomer.” *J. Microelectromech. Syst.* **9**. 76 (2000).
- [19] B. Xie, B. Danielsson, P. Norberg, F. Winqvist, and I. Lundstrom. “Development of a thermal micro-biosensor fabricated on a silicon chip.” *Sensors and Actuators B: Chemical* **6**. 127 (1992).
- [20] S. L. Lai, A. G. Ramanath, L. H. Allen, and P. Infante. “Heat capacity measurements of Sn nanostructures using a thin-film differential scanning calorimeter with 0.2 nJ sensitivity.” *Appl. Phys. Lett.* **70**. 43 (1997).



A.2 *Figures*

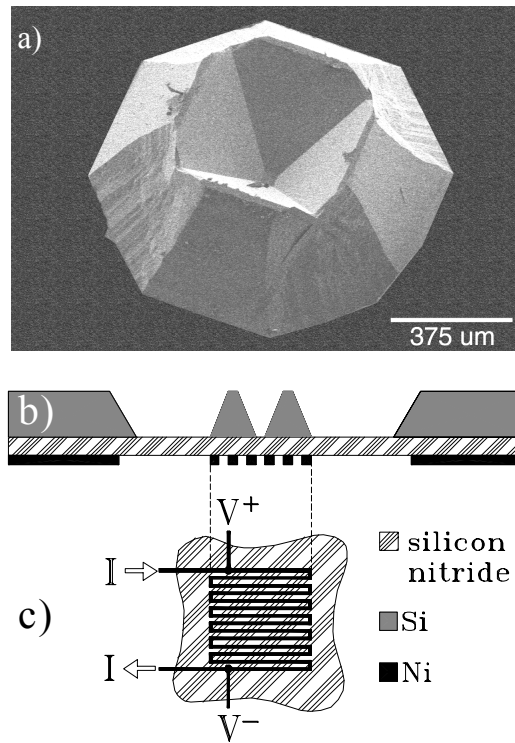


Figure 1: An electron micrograph of the silicon box (a), a cut-away schematic of the calorimeter (b), and a top view of the heater (c). Relative dimensions in (b) and (c) have been exaggerated for clarity.

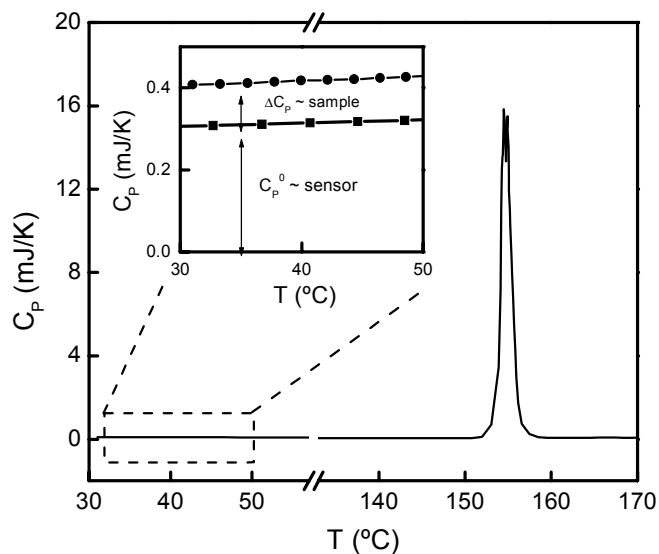


Figure 2: Melting of a 52 nL particle of indium at 150 K/s (average of six scans). The inset graph shows the baseline heat capacity of just the calorimeter (■) and the calorimeter plus the sample (●). The midpoint of the peak is at 155 °C, with a FWHM of 1.3 K. Measured  $H_m$  is 27.2 J/g. Bulk values for  $T_m$  and  $H_m$  of indium are 156.6 °C and 28.6 J/g, respectively. Sensitivity in this experiment was  $\pm 7 \mu\text{W}$ .

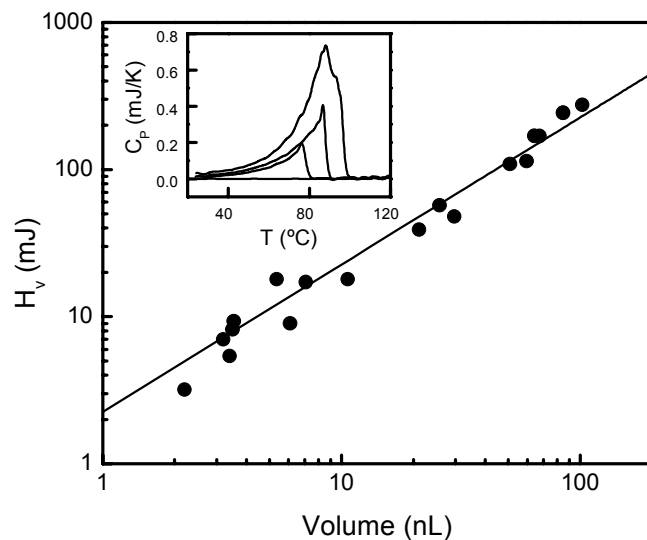


Figure 3: Nineteen water droplets and the heat it took to vaporize each one. The initial volume of the droplets ranged from 2 to 100 nL. (1 nL=1  $\mu$ g) The inset graph shows the heat capacity of three droplets, 2 nL, 3 nL, 7 nL in size, and of the calorimeter with no sample. The measured  $H_v$  was  $2250 \pm 500$  J/g (solid line), compared with the bulk value of  $H_v$  of 2260 J/g.

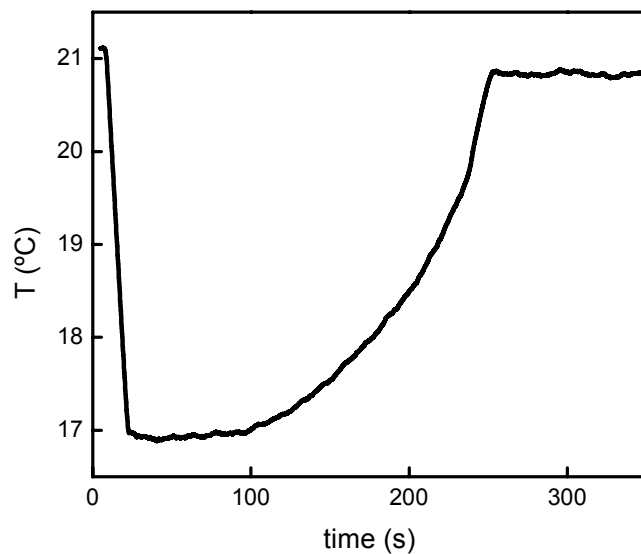


Figure 4: Passive temperature monitoring of water evaporation. At about  $t=10$  s, a small droplet of water was placed on the calorimeter, and the temperature measured throughout its evaporation. The data is smoothed with a 1.4 s moving average. We find  $H_v$  is within 25% of the expected value. Temperature sensitivity in this experiment is  $\pm 13$  mK.

## Appendix B: Protein Research

Excerpt from NSF Proposal, “Nanoliter Biocalorimetry on a Chip for Ultrafast Combinatorial Analysis of Proteins” by L. H. Allen (2002).

### PROJECT SUMMARY

The goal of this proposal is to develop a new protein calorimetry technology (MEMS) and begin measurements of protein folding. The unique aspects of this project include (1) the ultra-small (*nanoliters*) sample volumes, which are 1000× smaller than conventional calorimetric DSC systems and (2) an *ultrafast* scan rate which will be 1000× faster than DSC. The increased scan rate is more than just a way to provide a quick turn-around of results. The high rates will allow my group to capture the *intermediate* steps of protein folding that occur on the time scale of milliseconds – a capability not available with conventional DSC due to the thermal lag between sample and holder. The small sample size and compatibility with conventional IC systems will allow the technology to be extended to an array of calorimeters on a chip. This technology could be used as a basis for combinatorial studies. The extremely small sample sizes are also much needed for characterization of new proteins, which are usually synthesized in limited quantities.

This project will have a broad impact in boosting the *infrastructure in instrumentation* for the country, specifically in the area of biochemical calorimetry. The dissemination of our research results by the PI and his group’s graduate and undergraduate students will extend well beyond the usual materials conferences (e.g. AVS, MRS) to the core thermal analysis societies – NATAS, CalCon and IUPAC Chemical Thermodynamics. These groups serve the underlying thermal characterization needs of the country for *all* areas of science and technology. The research will hopefully become a case-study as part of the “*Frontiers of Calorimetry*” short-

course, which I instructed this last year for NATAS and hope to continue in the future. These societies involve a wide range of scientists (e.g. chemists, biologists) who are all extremely focussed on thermal measurements – *calorimetry*. MEMS calorimetry ideas are especially interesting to this audience, specifically in the area of high-speed, ultrathin/small sample size.

This research is based on my group’s success in developing MEMS nanocalorimeter technology for thin films (e.g. magic numbers nanostructures, *PRL* **85**, 3560 (2000)]. Our prototype calorimeter will serve as starting point for the necessary integrated effort that combines invention at the level of both technique and device.

I will incorporate our results into the showcase for ongoing research at UIUC during the annual “High School Visit Day for Materials.” Our results will serve as an example of the multidisciplinary nature of material science: MEMS (electronic materials), proteins (chemistry and biology), and folding/crystallization dynamics (thermodynamics).

This project provides a broad educational experience for our students, both graduate and undergraduate, for hands-on processing of the devices at UIUC and Cornell Univ. The project will also include electronics design and construction to operate the devices, and material analysis of proteins, which is unusual and exciting for a materials science group. S. Sligar, (UIUC Chemistry, College of Medicine) who is an expert in characterizing protein folding, will be our senior protein consultant on the project.

This proposal combines and addresses both the *Biosystems at the Nanoscale* and the *Nanoscale Structures, Novel Phenomena, and Quantum Control* research and education areas.

## Appendix C: FEA Programs

Following is the text of the MATLAB programs used to perform the two-dimensional finite element analyses.

### C.1 *sensor2D\_FEA.m*

```
function [Cp, res_heat, cur_heat, To, Qmelt] = sensor2D_FEA(memb, heat, prob, samp,
cI, dt, max_time, To, Qmelt, options)
% function [Cp, res_heat, cur_heat, Tout, Qmelt] = sensor2D_FEA(memb, heat,
%     prob, samp, cI, dt, max_time, To, Qmelt)
%
% Two dimensional FEA analysis of a sensor, implicit method.  Exp 131.
% INPUTS:
%   memb_file: filename for characteristics of the membrane layer of the sensor
%   heat_file: filename for characteristics of the heater layer of the sensor
%   prob_file: filename for characteristics of the voltage probe layer of the sensor
%   samp_file: filename for characteristics of the sample layer of the sensor
%   - Alternately, any of memb, heat, prob, or samp can be a 11-member cell
%   array with the same data.  Order: cCp, ck, cRCT, Hm, Tm, thicknxx,
%   maxx, maxy, dx, dy, filename.  Here, polynomial coefficients should be sent
%   as arrays.
%
%   cI: coefficients for current, polyval(cI, time) in A
%   dt: time interval used to calculate solution (s)
%   max_time: time after which to end the analysis (s)
%   To: sparse array with initial starting temperatures (K).  Should be the
%       same size as the arrays in the memb, etc., files
%   Qmelt: input array of melting matrix, (J).  If not present, or if empty,
%         creates a sparse matrix and uses that internally.
%   options: string of options, delimiter unimportant
%           'silent' means no output as program runs
%           'spy' means show each layer in a figure
%
% OUTPUTS:
%   Cp: numx x numy matrix of heat capacities at t = max_time in J/cm^3
%   H: numx x numy matrix of 1/sum(k*thickness) at t = max_time in W/cmK
%   pow_heat: numx x numy matrix of power dissipated in sensor at t =
%             max_time.  (Note: this should be 0 except where the heater is
%             non-zero.)
%   Tout: numx x numy sparse matrix of temperatures at each node at t =
%         max_time in K.  (There's not really any point in making this a sparse
%         matrix, since it has no non-zero elements.)
%
% version 1.0 EAO 21 Feb 2003
% version 2.0 EAO 26 Feb 2003
% 1. Changed several for loops to use vector notation, so they're much
% faster.
% version 3.0 EAO 27 Feb 2003
% 1. Added routine to deal with melting of sample
% 2. Changed a few lines to speed things up.  Avoid nested 'for' loops
% wherever possible!
% version 4.0 EAO 19 Mar 2003
% 1. Removed H and pow from outputs, and added resistance and current
% 2. Added input "options"
```

```

% version 5.0 EAO 4 Apr 2003
% 1. Added non-constant I
% 2. Added option for cell array inputs to memb, etc.
% version 6.0 (in progress)
% 1. Only solve over half the sensor.
% 2. Return Cp and To as full matrices.

% To do:
% 1. Loop over only half the matrix to make the solution faster, since the
% sensor is symmetric.

% Do some error checking on the inputs
if (dt < 0)
    error('ERROR: Time stepsize can not be negative!');
elseif (max_time < 0)
    error('ERROR: Stop time can not be negative!');
elseif (rem(max_time, dt) ~= 0)
    warning('SENSOR2D_FEA:FractionTimeStep', sprintf(['dt is not evenly divisible into
max_time. '...
'Actual max_time will be %g.\n'], fix(max_time/dt)*dt));
end
if (nargin <= 9)
    options = '';
end
if(isempty(regexpi(options, 'silent')))
    silent = 0;
else
    silent = 1;
end

% Read in the given files and make sure all the parameters are compatible
% with each other. (i.e. all matrices have the same size, dx == dy, etc.)
if (silent ~= 1)
    fprintf(1, 'Loading parameter files ... ');
end
[cCpmemb ckmemb tmp tmp tmp thick_memb maxx maxy dx dy memb_mat] =
read_sensor_file(memb);
[cCpheat ckheat cRCTheat tmp tmp tmp thick_heat maxx1 maxy1 dx1 dy1 heat_mat] =
read_sensor_file(heat);
if ( (maxx1 ~= maxx) | (maxy1 ~= maxy) | (dx1 ~= dx) | (dy1 ~= dy) | (size(heat_mat)
~= size(To)) )
    error('ERROR: Files are incompatible! Heater data not compatible. ');
end
[cCpprob ckprob tmp tmp tmp thick_prob maxx1 maxy1 dx1 dy1 prob_mat] =
read_sensor_file(prob);
if ( (maxx1 ~= maxx) | (maxy1 ~= maxy) | (dx1 ~= dx) | (dy1 ~= dy) | (size(prob_mat)
~= size(To)) )
    error('ERROR: Files are incompatible! Probe data not compatible. ');
end
[cCpsamp cksamp tmp Hm Tm thick_samp maxx1 maxy1 dx1 dy1 samp_mat] =
read_sensor_file(samp);
if ( (maxx1 ~= maxx) | (maxy1 ~= maxy) | (dx1 ~= dx) | (dy1 ~= dy) | (size(samp_mat)
~= size(To)) )
    error('ERROR: Files are incompatible! Sample data not compatible. ');
end
if (silent ~= 1)
    fprintf(1, 'Loaded.\n');
end
clear tmp maxx1 maxy1 dx1 dy1;

% Some useful constants

```



```

% vol_X is the volume of a (dx * dy * thick) unit of layer x
vol_memb = dx * dy * thick_memb;
vol_heat = dx * dy * thick_heat;
vol_prob = dx * dy * thick_prob;
vol_samp = dx * dy * thick_samp;
numx = round(maxx / dx);
numy = round(maxy / dy);

% Since we're solving half the matrix only, assume there are an even number
% of nodes.
if (rem(numx,2) > 2*eps) % Use EPS to avoid roundoff error
    error('ERROR: Need an even number of nodes in the x direction.');
```

```

end
numx2 = round(numx/2); % This is the number of the last column on the left half of
the sensor

ThRes = sparse(numy*(numx2+1), numy*(numx2+1));
ThRes_size = numy*(numx2+1);
right = sparse(numy*(numx2+1), 1);
Tamb = 300; % Assume ambient (edges) are 300 K
Qo = Hm * dx * dy * thick_samp; % Heat (J) to melt one node of sample

% Let's make some assumptions about the analysis being done.
if ( (numx <= 2) || (numy <= 2) )
    error('Oh come on, we need more nodes than that!');
```

```

end

% Allocate these for future use
res_heat = sparse(numy, numx);
cur_heat = sparse(numy, numx);
pow_heat = sparse(numy, numx);
if (margin == 8) | (prod(size(Qmelt)) == 0)
    Qmelt = sparse(numy, numx);
end

% Need inline functions for use with SPFUN, so we can operate only over the
% non-zero members of a sparse matrix
recip = inline('1./x');
```

```

% Create some sets of indices we'll need later. Don't need to do this
% every time. Indices are column-ordered.
% cn will be the center nodes, i.e. nodes not on an edge
% We can't use linear indexing for the center nodes, because the ThRes
% matrix becomes too large and the maximum linear index size MATLAB can
% handle is 2^32-1 (65535). So for ThRes, we'll have to use (i,j)
% indexing.
cn = [];
for ii = 2:numx2
    cn = [cn (ii-1)*numy+2:(ii)*numy-1];
end

% te will be the top nodes
te = 1:numy:numx2*numy;
% be will be the bottom nodes
be = numy:numy:numx2*numy;

% Begin looping, once per time slice. Since the loop calculates the
% temperatures at t=to+dt, stop if t=max_time.
time = 0;
```

```

iter = 1;
max_iter = round(max_time/dt);
if (silent ~= 1)
    fprintf(1, 'Beginning main calculation: %i time slices needed.\n',
round(max_time/dt));
end
while (iter <= max_iter)
    % Print a '*' each iteration, so we know the process is running. At 50
    % chars wide, print a linefeed so it wraps.
    if (silent ~= 1)
        if (time > 0)
            if (rem(time/dt, 50) < 1)
                fprintf(1, ' %i\n', fix(time/dt));
            end
        end
        fprintf(1, '*');
    end

    % Construct a net Cp matrix, where Cp(i,j) is the sum of the Cp's of the
    % four layers. Cp is in J/K after this.
    Cp = (polyval(cCpmemb, To) * vol_memb .* memb_mat) + (polyval(cCpheat, To) *
vol_heat .* heat_mat) + ...
        (polyval(cCpprob, To) * vol_prob .* prob_mat) + (polyval(cCpsamp, To) *
vol_samp .* samp_mat);

    % H will be 1/sum(k*thick). It is a material property. The thermal
    % conductivities add in parallel. Multiply H by dx/dy to get thermal
    % resistance matrix. However, dx/dy will depend on the direction of heat
    % flow, so it's not a material property. H is basically NET thermal
    % conductivity for that node
    H = polyval(ckmemb, To)*thick_memb .* memb_mat + polyval(ckheat, To)*thick_heat .*
heat_mat + ...
        polyval(ckprob, To)*thick_prob .* prob_mat + polyval(cksamp, To)*thick_samp .*
samp_mat;
    H = 1 ./ H;

    % Calculate the resistance of each heater segment, current through it and,
    % the power in each segment. Loops are to avoid calculating 1/0 for the
    % empty matrix cells.
    ii = find(heat_mat);
    [i j] = find(heat_mat);
    res_heat(ii) = polyval(cRCTheat, To(ii)) * dx/dy;
    netres = 1 ./ sum(sfun( recip, res_heat));
    Itot = polyval(cI, time);
    cur_heat(ii) = Itot * netres(floor(ii/numy)+1)' ./ res_heat(ii);
    pow_heat = (cur_heat.^2) .* res_heat;

    % Now start constructing a matrix of thermal resistances
    % ThRes(i,j) will be the thermal resistance between nodes i and j. Note
    % that this changes the numbering scheme of the matrix, and no longer
    % spacially represents the physical makeup of the sensor.
    % ThRes(i,j) = ThRes(j,i) so we don't need to calculate for every i,j
    % combination.
    %
    % Start with nodes not on the edges, so they all have four neighbors
    % Note: Don't reference ThRes inside for/for loops. That's REALLY
    % slow.

    % Note: This syntax works really well, but doesn't work if ThRes gets
    % above 65535x65535 or so.
    % ThRes(sub2ind(size(ThRes), cn, cn+1)) = 0.5 .* dy/dx .* (H(cn) + H(cn+1));

```

```

% ThRes(sub2ind(size(ThRes), cn, cn+numy)) = 0.5 .* dx/dy .* (H(cn) +
H(cn+numy));
down_diag = sparse(ThRes_size,1);
right_diag = down_diag;
down_diag(cn+1) = 0.5 .* dy/dx .* (H(cn) + H(cn+1));
right_diag(cn+numy) = 0.5 .* dx/dy .* (H(cn) + H(cn+numy));

% Now take care of the left edge, except for the bottom-left corner
down_diag((1:numy-1)+1) = 0.5 * dy/dx * (H(1:numy-1) + H(2:numy));
%% ThRes(sub2ind(size(ThRes), 1:numy-1, 2:numy)) = 0.5 * dy/dx * (H(1:numy-1) +
H(2:numy));
right_diag((1:numy)+numy) = 0.5 * dx/dy * (H(1:numy) + H(numy+1:2*numy));
%% ThRes(sub2ind(size(ThRes), 1:numy, (1:numy)+numy)) = 0.5 * dx/dy * (H(1:numy) +
H((1:numy)+numy));

% Top edge, use indices te from above
down_diag(te+1) = 0.5 * dy/dx * (H(te) + H(te+1));
right_diag(te+numy) = 0.5 * dx/dy * (H(te) + H(te+numy));

% Bottom edge, use indices be from above
right_diag(be+numy) = 0.5 * dx/dy * (H(be) + H(be+numy));

% Right edge (halfway mark)
down_diag((numx2-1)*numy+2:numx2*numy) = 0.5 * dy/dx * ...
(H((numx2-1)*numy+1:numx2*numy-1) + H((numx2-1)*numy+2:numx2*numy));

ThRes = spdiags([down_diag right_diag], [1 numy], ThRes_size, ThRes_size);

% Use symmetry to complete the matrix. (Although, I'm not sure we need
% more than the upper half of the matrix.)
[ii jj v] = find(ThRes);
ThRes = ThRes + sparse(jj, ii, v, numy*(numx2+1), numy*(numx2+1));

% Now we need to construct the matrix that will be used for the linear
% algebra. The details of this matrix are too complicated to go into here.
% In short, we will solve A*x=b where A incorporates ThRes, x is the future
% temperature, and B incorporates the internal heat and current
% temperature. We can re-use ThRes to avoid additional storage, but we
% need to add to the diagonal, and we need the reciprocal of each element.
%
% The edge nodes are boundary conditions and need to be handled separately,
% so start with non-edge nodes.
% The solutions require the reciprocal of the thermal resistances.
ThRes = spfun( recip, ThRes);
cent_diag = -1 * sum(ThRes,2);

% Now adjust for the boundary conditions.
% Left edge
cent_diag(1:numy) = cent_diag(1:numy) - (2 * dx/dy * (1 ./ H(1:numy)'));
% Top edge
cent_diag(te) = cent_diag(te) - (2 * dy/dx * (1./H(te)'));
% Bottom edge
cent_diag(be) = cent_diag(be) - (2 * dy/dx * (1./H(be)'));
% No adjustments needed for the right edge

% Now incorporate Cp/dt.
%
% We also need to create the right hand side of the equation, which will
% incorporate the internal heat generation and the current temperature.
% The pow_heat matrix needs to be converted to a (numx*numy,1) vector.
% Let's do that here to prevent needing another loop later.
%
```

```

cent_diag(1:numx2*numy) = cent_diag(1:numx2*numy) - Cp(1:numx2*numy)' / dt;

% Now store cent_diag in the zeroth diagonal of ThRes
ThRes = spdiags(cent_diag, 0, ThRes);

% Here's the right hand side of the equation. All the transposing and
% such is because M(i) runs down column 1, then column 2, etc. rather
% than row 1, row 2, etc.
right(1:numy*numx2) = (-1) * pow_heat(1:numy*numx2) - ((Cp(1:numy*numx2) .*
To(1:numy*numx2))/dt);

% Now take into account the edges, need a Tamb factor in there.
% Again, no correction needed for the right (halfway) edge.
right(1:numy) = right(1:numy)' - 2 * Tamb * (dx/dy) ./ H(1:numy);
right(te) = right(te)' - 2 * Tamb * (dy/dx) ./ H(te);
right(be) = right(be)' - 2 * Tamb * (dy/dx) ./ H(be);

% Adjust ThRes, right, and Qmelt to take into account the melting of
% the sample.
% There are four possibilities:
% 1. The sample is not hot enough to melt (To < Tm)
% 2. The sample is melting, but not finished melting during this dt
% 3. The sample will finish melting this dt, and continue heating a bit
% 4. The sample is hotter than Tm, but fully melted already (Qmelt >= Qm)

% Find indices ii and jj where #1 is not the case and #4 is not the
% case. Make sure only to look where there is sample
ii = find( (Qmelt < Qo) & ((To + ((pow_heat*dt) ./ Cp)) > Tm) & samp_mat);
kk = find(ii <= numx2*numy);
ii = ii(kk);

% If melting_index contains the node numbers of nodes where case #2 or
% #3 is TRUE.
melting_index = [];
for m = 1:length(ii)
    jj = ii(m);
    if ((Qmelt(jj) + pow_heat(jj)*dt) < Qo)
        % Case #2
        kk = find(ThRes(jj, :));
        ThRes(jj, kk) = 0;
        ThRes(jj, jj) = 1;
        right(jj) = Tm;
        Qmelt(jj) = Qmelt(jj) + pow_heat(jj)*dt;
    else
        % Case #3
        right(jj) = right(jj) + (Qo - Qmelt(jj))/dt;
        Qmelt(jj) = Qo;
    end
end
end

% Since we're assuming the sensor is symmetric, with a point of
% inversion around the center, the right half of the sensor (x>numx2)
% is the same as the left half (x<=numx2) with the y's reversed. We
% need T(:, numx2+1) to determine T(:, numx2), but they're the same,
% just in reverse order.
% Note: this breaks the symmetry of the ThRes matrix.
for ii = numx2*numy+1:(numx2+1)*numy
    jj = find(ThRes(ii, :));
    ThRes(ii, jj) = 0;
    ThRes(ii, ii) = 1;
    ThRes(ii, numx2*numy-(ii-(numx2*numy+1))) = -1;
end
end

```

```

right(numx2*numy+1:(numx2+1)*numy) = 0;
right((numx2+1)*numy+1:end) = [];

% Now let's solve for the solution.
Tfut = ThRes\right;

% This solves for the left half of the sensor, plus one row. The right
% half of the sensor is mirrored about the numx2 column, but flipped in
% the y-direction, so create the rest of the temperature matrix.
To(1:numx2*numy) = Tfut(1:numx2*numy);
To(numx*numy:-1:numx2*numy+1) = Tfut(1:numx2*numy);

% Clear ThRes and increment the timer
ThRes(:, :) = 0;
time = time + dt;
iter = iter + 1;
end % Stop looping once per time slice
if (silent ~= 1)
    fprintf(1, '\n');
end

% Since we're going to return current and resistance, they must be
% recalculated with Tfut.
% Commented out for debugging 8 Apr
Cp = (polyval(cCpmemb, To) * vol_memb .* memb_mat) + (polyval(cCpheat, To) * vol_heat
.* heat_mat) + ...
    (polyval(cCpprob, To) * vol_prob .* prob_mat) + (polyval(cCpsamp, To) * vol_samp
.* samp_mat);
ii = find(heat_mat);
[i j] = find(heat_mat);
res_heat(ii) = polyval(cRCTheat, To(ii)) * dx/dy;
netres = 1 ./ sum(spfun(recip, res_heat));
cur_heat(ii) = Itot * netres(floor(ii/numy)+1)' ./ res_heat(ii);

% Return these as full matrices, since they have no zeros
Cp = full(Cp);
To = full(To);

% Output figures for the user to make sure stuff is in the right place
if (~(isempty(regexpi(options, 'spy'))))
    figure(1); clf; hold on;
    spy(heat_mat, '.');
    spy(samp_mat, 'ks');
    spy(prob_mat, 'ro');
    legend('Heater', 'Sample', 'Probes');
end

return; % End sensor2D_FEA

%-----
%SUBFUNCTIONS CALLED ONLY BY THIS PROGRAM
%-----

function [cCp, ck, cRCT, Hm, Tm, thick, maxx, maxy, dx, dy, sparsemat] =
read_sensor_file(filename)
% Added possibility that 'filename' is a cell array rather than a string.
% April 2003. EAO

```

```

if iscell(filename)
    cCp = filename{1};
    ck = filename{2};
    cRCT = filename{3};
    Hm = filename{4};
    Tm = filename{5};
    thick = filename{6};
    maxx = filename{7};
    maxy = filename{8};
    dx = filename{9};
    dy = filename{10};
    % If {11} is a char string, assume it's a filename. If not, assume
    % it's sparsemat itself.
    if (ischar(filename{11}))
        try
            tempmat = dlmread(filename{11});
        catch
            error(['ERROR: Unable to open file ' line '. Nonexistant?']);
        end
        sparsemat = spconvert(tempmat);
    else
        sparsemat = filename{11};
    end;
    return;
end

if ~(ischar(filename))
    error('sensor2D_FEA:badinput', 'ERROR: input to read_sensor_file must be either a
string or a cell array.');
```

```

end

fid = fopen(filename);
if (fid == -1)
    error(['ERROR: Unable to open file ' filename ' for reading.']);
end

% Get cCp coefficients
i=1;
while (i<=5)
    line_in = fgetl(fid);
    if (line_in == -1)
        fclose(fid);
        error(['ERROR: File format error while reading file ' filename]);
    elseif (line_in(1) ~= '%')
        cCp(i) = sscanf(line_in, '%g');
        i = i+1;
    end
end

% Get ck coefficients
i=1;
while (i<=5)
    line_in = fgetl(fid);
    if (line_in == -1)
        fclose(fid);
        error(['ERROR: File format error while reading file ' filename]);
    elseif (line_in(1) ~= '%')
        ck(i) = sscanf(line_in, '%g');
        i = i+1;
    end
end
end

```

```

% Get cRCT coefficients
i=1;
while (i<=5)
    line_in = fgetl(fid);
    if (line_in == -1)
        fclose(fid);
        error(['ERROR: File format error while reading file ' filename]);
    elseif (line_in(1) ~= '%')
        cRCT(i) = sscanf(line_in, '%g');
        i = i+1;
    end
end
end

while (1)
    line_in = fgetl(fid);
    if (line_in == -1)
        fclose(fid);
        error(['ERROR: File format error while reading file ' filename]);
    elseif (line_in(1) ~= '%')
        break;
    end
end
Hm = sscanf(line_in, '%g');

while (1)
    line_in = fgetl(fid);
    if (line_in == -1)
        fclose(fid);
        error(['ERROR: File format error while reading file ' filename]);
    elseif (line_in(1) ~= '%')
        break;
    end
end
Tm = sscanf(line_in, '%g');

while (1)
    line_in = fgetl(fid);
    if (line_in == -1)
        fclose(fid);
        error(['ERROR: File format error while reading file ' filename]);
    elseif (line_in(1) ~= '%')
        break;
    end
end
thick = sscanf(line_in, '%g');

while (1)
    line_in = fgetl(fid);
    if (line_in == -1)
        fclose(fid);
        error(['ERROR: File format error while reading file ' filename]);
    elseif (line_in(1) ~= '%')
        break;
    end
end
maxx = sscanf(line_in, '%g');

while (1)
    line_in = fgetl(fid);
    if (line_in == -1)
        fclose(fid);
        error(['ERROR: File format error while reading file ' filename]);
    elseif (line_in(1) ~= '%')

```

```

        break;
    end
end
maxy = sscanf(line_in, '%g');

while (1)
    line_in = fgetl(fid);
    if (line_in == -1)
        fclose(fid);
        error(['ERROR: File format error while reading file ' filename]);
    elseif (line_in(1) ~= '%')
        break;
    end
end
dx = sscanf(line_in, '%g');

while (1)
    line_in = fgetl(fid);
    if (line_in == -1)
        fclose(fid);
        error(['ERROR: File format error while reading file ' filename]);
    elseif (line_in(1) ~= '%')
        break;
    end
end
dy = sscanf(line_in, '%E');

while (1)
    line_in = fgetl(fid);
    if (line_in == -1)
        fclose(fid);
        error(['ERROR: File format error while reading file ' filename]);
    elseif (line_in(1) ~= '%')
        break;
    end
end
try
    tempmat = dlmread(line_in);
catch
    error(['ERROR: Unable to open file ' line_in '. Nonexistent?']);
end
sparsemat = spconvert(tempmat);
fclose(fid);
return;

```

## C.2 *sensor2D\_res.m*

```

function res_mat = sensor2D_res(res_mat, dx, dy, Lprb, Rprb)
% function net_resistance = sensor2D_res(res_mat, dx, dy, Lprb, Rprb)
%
% Calculates the net resistance of a sensor between the voltage probes.
% Intended to be used with the output from sensor2D_FEA.
%
% INPUTS
% res_mat: sparse matrix output of resistance from sensor2D_FEA
% dx, dy: delta x and y spacing of the FEA mesh, in um
% Lprb, Rprb: locations of the voltage probes from the left egde, in um.
% Lprb = 900 and Rprb = 6600 for standard sensor.
%
% OUTPUTS
% net_resistance: Resistance in ohm of the sensor (scalar). This should be the

```



```

% value measured by a voltmeter or in an experiment.
%
% EAO v1.0 28 Feb 2003

% Find the number of x and y points
[numx numy] = size(res_mat);

% Assume matrix represents a sensor 7500 x 2000 um in size
maxx = 7500;
maxy = 2000;

% Now construct a matrix of locations for the center of each node
x = ((1:numx)-1)*dx) + (dx/2);
y = ((1:numy)-1)*dy) + (dy/2);

% Find the entries in the res_mat matrix that are between the two voltage
% probes.
ii = find( (x > Lprb-(dx/2)) & (x < Rprb+(dx/2)) );
res_mat = res_mat(:, ii);

% In case a voltage probe location falls in the middle of a node, scale the
% resistances of those nodes to be a fraction of the total. Only affects
% the nodes at either extreme of the res_mat matrix.
res_mat(:,1) = res_mat(:,1) * ( (x(ii(1)) + (dx/2) - Lprb)/dx );
res_mat(:,end) = res_mat(:,end) * ( Rprb - (x(ii(end)) - (dx/2)))/dx;

% Need inline functions for use with SPFUN, so we can operate only over the
% non-zero members of a sparse matrix
recip = inline('1./x');

% Add each column of nodes in parallel. 1/Rnet = 1/R1 + 1/R2 + ...
% use spfun because res_mat is a sparse matrix and to avoid 1/0 errors.
res_mat = spfun(recip, res_mat);
res_mat = sum(res_mat);
res_mat = spfun(recip, res_mat);

% Now add each column of nodes in series
res_mat = sum(res_mat);

% res_mat should now be a 1x1 sparse matrix, but we want to return a
% scalar
res_mat = res_mat(1,1);

```

### ***C.3 sensor2D\_simCp.m***

```

function [matrix_out, R, To, Qmelt, sim_T, sim_pow] = sensor2D_simCp(memb, heat, prob,
samp, cI, dt, max_time, To, Qmelt, dx, dy, Lprb, Rprb, cTCR)
% function [matrix_out, R, To, Qmelt, sim_T, sim_pow] =
%     sensor2D_simCp(memb, heat, prob, samp, cI, dt, max_time, To, Qmelt, dx, dy,
Lprb, Rprb, cTCR)
%
% Calculates simulated Cp for a sensor, using 2D FEA analysis. Calls
% sensor2D_FEA.m and sensor2D_res.m.
%
% INPUTS:
% memb, heat, prob, samp: filenames or cell arrays with membrane, heater,
% probe, sample layer data. See sensor2D_FEA.m for details.
% cI: current polynomial coefficients, I = polyval(cI, time)
% dt: time spacing of FEA mesh (s)
% max_time: total time of simulation (s)
% To: sparse matrix of starting temperature (K)

```

```

% Qmelt: sparse matrix of heat used to melt each node (J). Qmelt = Hm*vol if
% that node has fully melted. Qmelt = 0 if that node is fully solid. This
% should probably be an empty matrix for a Cp run.
% dx: x-spacing of FEA mesh (um, NOT m)
% dy: y-spacing of FEA mesh (um, NOT m)
% Lprb: distance from left edge of sensor to left voltage probe (um)
% Rprb: distance from left edge of sensor to right voltage probe (um)
% cTCR: heater TCR coefficients, needed to convert simulated R to T.
%
% OUTPUTS:
% matrix_out: matrix similar to output of HCAP program. Four columns:
% [time, resistance, temperature, simulated Cp]
% R: sparse matrix of resistance of the heater
% To: sparse matrix of temperature in the sensor, at the end of the
% simulation
% Qmelt: sparse matrix of heat used to melt each node, at the end of the
% simulation. Qmelt = 0 if no melting occurred.
% sim_T: same as matrix_out(:,3) used for debugging
% sim_pow: dissipated power (I^2*R), used for debugging
%
% v1.0 EAO 1 Apr 2003

% Need this line to prevent the page from filling up and stopping the
% calculation
more off;

% Sensor dimensions
len = 5700E-4;
width = 500E-4;

% Some counters
time = 0;
ii = 1;
max_iter = round(max_time/dt);

% Calculate the sensor resistance at each time step. This is inefficient,
% as it winds up loading the sensor data files every loop, but it's going
% to take a long time anyway. Sending the parameters as cell arrays speeds
% this up considerably.
fprintf(1, 'Need %i loops.\n', round(max_time/dt));
while (ii <= max_iter)
    fprintf(1, '*');
    if (rem(ii,50) < 1)
        fprintf(1, ' %i\n', ii);
    end

    cur = polyval(cI, time);

    % Solve for this time step, To and Qmelt should be the outputs from the
    % previous iteration
    [Cp R Cur To Qmelt] = sensor2D_FEA(memb, heat, prob, samp, cur, dt, dt, To, Qmelt,
'silent');

    % Find th average (simulated) resistance
    sim_R(ii) = sensor2D_res(R, dx, dy, Lprb, Rprb);

    % increment the counters
    t(ii) = time;
    time = time + dt;
    ii = ii + 1;
end

% Convert the simulated resistance to temperature, and calculated the power

```

```

% dissipated
sim_T = polyval(cTCR, sim_R);
sim_I = polyval(cI, t);
sim_pow = sim_I.^2 .* sim_R;

% Fairly simplistic way to find dT/dt
jj = length(sim_T);
if (jj > 2)
    ii = 2:jj-1;
    dTdt(ii) = (sim_T(ii+1) - sim_T(ii-1)) / (2*dt);
end
dTdt(1) = (sim_T(2) - sim_T(1)) / dt;
dTdt(jj) = (sim_T(jj) - sim_T(jj-1)) / dt;

% Now calculate Cp = P/rate
sim_Cp = sim_pow ./ dTdt;

% This will be a matrix of similar form to the output of HCAP program.
matrix_out = [t; sim_R; sim_T; sim_Cp]';

% Turn more back on, since we turned it off at the beginning.
more on;

```

## **Vita**

Eric Ashley Olson was born in Austin, Texas on July 31, 1973. He graduated from Rice University in 1995 with a degree in Materials Science and Engineering. For several years he worked as a materials engineer for Syscom Development Inc., then McDonnell Douglas, which later became The Boeing Company, before beginning graduate study in Champaign, Illinois.